Numerical modelling and evaluation of the temperature distribution in an earthmover tyre: Establishing a safe operating envelope

by

Jeannette Marais

Thesis presented in partial fulfilment of the requirements for the degree of Master of Engineering (Mechanical) in the Faculty of Engineering at Stellenbosch University

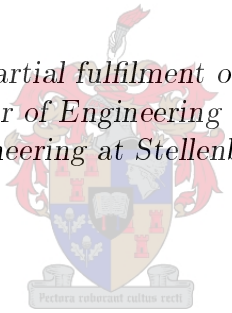

Supervisor: Prof. G. Venter

March 2017

Declaration

By submitting this thesis electronically, I declare that the entirety of the work contained therein is my own, original work, that I am the sole author thereof (save to the extent explicitly otherwise stated), that reproduction and publication thereof by Stellenbosch University will not infringe any third party rights and that I have not previously in its entirety or in part submitted it for obtaining any qualification.

Signature: .....
J. Marais

Date: March 2017

Abstract

The explosion of haul truck tyres due to internal heat generation during operation can lead to loss of life and severe damage to the vehicle and the surroundings. This thesis describes the development of a finite element model for the numerical modelling of a 23.5R25 earthmover tyre using MSC.Marc/Mentat. The numerical model is subjected to different combinations of inflation pressures, loads and rolling velocities to obtain a working knowledge of the heat generation in the tyre cross-section as a function of these conditions. This function is used to give an indication to the maximum temperature in the tyre's cross-section during steady-state heat transfer conditions. As a result, this function can be used to ensure that maximum temperature in the tyre cross-section remains within a safe operating envelope to prevent the explosion of these tyres.

The static tyre deformation obtained from the numerical analysis was compared to experimental data provided by the manufacturer to evaluate the accuracy of the proposed numerical model. From the results obtained it was concluded that the numerical tyre results were consistent with the experimental data within a maximum percentage difference of 3.9 %, 2.5 %, 3.4 % and 9.7 % for the vertical tyre deflection, the overall tyre width, the tyre's contact width and the tyre's contact length, respectively. Thus, it was concluded that the numerical model represented the deformation of the actual tyre to an acceptable extent.

The thermal results could not be experimentally verified and therefore its accuracy could not be determined explicitly. However, from the theoretical description of the method used to simulate the heat generation rate in numerical models, it was evident that the heat generation rate will ultimately be a function of the tyre's deformation and its rolling velocity. Thus, the assumption was made that the accuracy of the static tyre behaviour could be used to provide some measure of verification of the thermal results. Furthermore, thermal results were consistent with the expected temperatures observed in industry when the tyre is subjected to similar conditions. Thus, the thermal results were used to establish an equation that predicted the expected maximum temperature in the tyre's cross-section as a function of the tyre's vertical deflection, its velocity and the ambient temperature of the surroundings. This equation could in turn be used to maintain allowable temperature conditions in the tyre during operation. Furthermore, it was concluded that the rolling velocity of the tyre will have the most significant effect on the heat generation in the tyre and therefore should be managed accordingly.

Opsomming

Die ontploffing van myntrok-bande as gevolg van die interne hitte wat in die deursnit van die band gegenereer word kan lei tot die verlies van lewe en ernstige skade aan die voertuig en die omgewing. Hierdie tesis beskryf die ontwikkeling van 'n eindige element model van 'n 23.5R25 grondverskuiwingsband met behulp van MSC.Marc/-Mentat. Die numeriese model word onderwerp aan verskillende kombinasies van inflasiedrukke, laste en snelhede om die hitte-generasie in die deursnit van die band te evalueer as 'n funksie van hierdie toestande. Hierdie funksie word dan gebruik om 'n aanduiding van die maksimum temperatuur in die band se deursnit tydens ewewigstoestand te voorspel. Gevolglik kan hierdie funksie gebruik word om te verseker dat die maksimum temperatuur in die deursnit van die band binne 'n veilige werkstoestand bly om die ontploffing van hierdie bande te voorkom.

Die statiese band se vervorming is met eksperimentele data soos verskaf deur die vervaardiger vergelyk om die akkuraatheid van die voorgestelde numeriese model te bepaal. Op grond van hierdie resultate was dit duidelik dat die numeriese resultate in ooreenstemming met die gemete data is met 'n maksimum persentasie verskil van 3.9 %, 2.5 %, 3.4 % en 9.7 % vir die vertikale band defleksie, die algehele bandwydte, die kontak breedte van die band en die kontak lengte van die band, onderskeidelik. Dus is die gevolgtrekking gemaak dat die vervorming van die numeriese model die werklike vervorming van die band tot 'n aanvaarbare mate voorstel.

Die termiese resultate kon nie met eksperimentele resultate vergelyk word om die akkuraatheid daarvan te bepaal nie. Vanuit die teoretiese beskrywing van die metode wat gebruik is om die hitte-generasie in numeriese modelle te bepaal, was dit duidelik dat die hitte-generasie in die band 'n funksie van die band se vervorming en snelheid is. Dus is die aanname gemaak dat die akkuraatheid van die statiese analise gebruik kan word om 'n mate van verifikasie van die termiese resultate te verskaf. Verder was dit ook duidelik die termiese resultate in ooreenstemming was met die verwagte temperature in industrie indien die bande onderwerp is aan soortgelyke omstandighede. Dus is die termiese resultate gebruik om 'n vergelyking te ontwikkel wat die verwagte maksimum temperatuur in die deursnit van die band voorspel as 'n funksie van die band se vertikale defleksie, snelheid en die omgewingstemperatuur. Hierdie vergelyking kon dan op sy beurt gebruik word om toelaatbare temperatuur kondisies in the band tydens werking te handhaaf. Vanuit hierdie beskrywing is dit duidelik dat die band se snelheid die mees beduidende invloed op die hitte-generasie in die band sal hê en daarom moet dit ooreenstemmend beheer word.

Acknowledgements

I would like to express my sincere gratitude to the following people and organisations:

- Prof. Gerhard Venter for his guidance and support.
- My family and friends for their love and support.
- Anglo American for their financial support.
- Rhasatsha high performance computer (HPC) at Stellenbosch University for the computational resources: http://www.sun.ac.za/hpc.

Dedications

Hierdie tesis word opgedra aan my Hemelse Vader. Net Hy alleen kan inspireer, lei en dra. Aan Hom al my eer.

Contents

List of Figures

List of Tables

Chapter 1

Introduction

Earthmover tyres are typically used for haul trucks in the mining industry. These trucks are designed to operate in severe environmental conditions while transporting extreme loads. In order to meet these requirements, earthmover tyres consist of large amounts of rubber. When rubber is subjected to cyclic deformation, such as the rolling of a tyre, the rubber tends to absorb more energy than it can dissipate. The lost energy is known as hysteresis loss and is stored in the rubber as heat. The heat stored in the rubber can cause an increase in the internal tyre temperature. An increase in the internal tyre temperature will cause an increase in its internal pressure.

At elevated temperatures rubber starts to degrade. This degradation process is known as either pyrolysis or thermo-oxidation. Pyrolysis can occur in the absence of oxygen, while thermo-oxidation can only occur in the presence of oxygen (Benoît *et al.*, 2009). The gases produced during these reactions contribute to the pressure build-up inside the tyre. If a sufficient concentration of flammable gas, a temperature and pressure reading equal to or greater than the auto-ignition temperature and pressure of the flammable gas, and an oxygen concentration above 5.5 % are present in the tyre, the tyre can explode violently (Benoît *et al.*, 2009). The shock waves and debris propagating from this explosion can lead to fatal injuries and severe damage to the surroundings and the vehicle itself.

Thus, the explosion of earthmover tyres due to internal heat generation is a major concern in the mining industry. A working knowledge of the heat generation in the tyre cross-section is required to manage and eliminate this risk. The structural analysis of pneumatic tyres by finite element analysis is a cost-effective alternative to field tests that can be used to gain insight into the heat generation in a rolling tyre. By studying the heat generation in the tyre cross-section as a function of different operating conditions, such as the inflation pressure, load and rolling velocity of the tyre, the internal tyre temperature can be predicted and used to establish a safe operating envelope.

1.1 Project background and motivation

This project is the third part of a three part investigation for Anglo American PLC (Anglo). This investigation was initiated after the explosion of earthmover tyres at some of their mines claimed the lives of employees. Anglo approached Stellenbosch University to develop a numerical model of an earthmover tyre that can be used to predict the temperature in the tyre cross-section.

The first part of the investigation was completed by Maritz (2015) at Stellenbosch University. This project included the numerical modelling of a passenger vehicle tyre and an evaluation of the temperature distribution in the tyre cross-section as a function of different inflation pressures, loads applied to the tyre and rolling velocities. This evaluation was based on a comparison of the numerical results and experimental results obtained from tests done on a tyre test bench donated by Anglo to Stellenbosch University. If the numerical and experimental results were consistent, the model could be scaled to represent an earthmover tyre and it could be assumed that the analysis procedure used to calculate the temperature distribution in the tyre cross-section is viable.

Unfortunately, shortcomings, such as a lack of deformation in the tyre sidewall, insufficient heat generation and a misrepresentation of the temperature distribution in the tyre cross-section, were evident. Maritz (2015) stated that these shortcomings were mainly due to two factors: first, the rubber was modelled with material properties obtained from literature and not established experimentally from tests done on the actual tyre. Second, the tyre was modelled with only one type of rubber, when in reality, tyres consist of various rubber compounds with different compositions and material properties. Considering the highly non-linear stress-strain behaviour of rubber, the actual material properties and different properties of each rubber compound in a tyre, would significantly affect the response of the numerical model. Hypothetically, Maritz (2015) concluded that the actual response of the numerical model will be more consistent with the experimental results, if the stated factors were corrected.

As a result, a second project was assigned to Van Blommestein (2016) to validate this hypothesis. This project included a study on the numerical response of the same tyre using material properties from tests done on the actual tyre and modelling the different rubber compounds in the tyre structure. From this project, it was concluded that the numerical models showed significant improvements compared to the model developed by Maritz (2015). With regard to the consistency of the numerical and experimental results, the numerical models accurately captured the static tyre deflection as well as the thermal response of the tyre. Based on these findings, it was concluded that the analysis procedure suggested by Maritz (2015) and Van Blommestein (2016) can be used to predict both the static tyre behaviour and thermal response. However, the thermal response of the numerical model in the tyre shoulder where the maximum tyre temperature would typically occur, was not verified experientially and consequently the measure of accuracy at this specific point could not be determined.

The project considered in this study, is the third part of the investigation. The methodology used to develop a numerical model of an earthmover tyre and simulate its temperature distribution in the tyre cross-section, is based on the previous work done by Maritz (2015) and Van Blommestein (2016). The numerical results obtained in this project, will ultimately be used to establish a safe operating envelope for the tyre to conclude the investigation.

1.2 Project objectives

The project objectives are as follow

1. Develop a numerical model of an earthmover tyre that can be used to determine the temperature distribution in the tyre cross-section. The methodology used to develop the model will be based on the previous work done by Maritz (2015) and Van Blommestein (2016).

2. Simulate the temperature distribution in the tyre cross-section at different inflation pressures, loads and rolling velocities. The value of these conditions should be consistent with the actual conditions these tyres are exposed to in industry.

3. Establish the material properties of an earthmover tyre from experimental tests done on the actual tyre.

4. Validate the numerical results obtained for each simulation. The results must be considered to be accurate and viable in order to establish a safe operating envelope for the tyre.

5. Use the validated results to establish a safe operating envelope that could be used to prevent the tyre from reaching critical temperatures during operation.

1.3 Project outline

The following activities were completed in order to reach the project objectives stated in the previous section:

- A literature study on the tyre structure and its materials, the calculation of heat generation in a rolling tyre, and the numerical analysis procedure used to model temperature distribution in the tyre cross-section.

- Obtaining the tyre and rim specifications to numerically model the actual tyre geometry.

- Establishing the material properties of an earthmover tyre by performing experimental tests on an actual earthmover tyre.

- Determining the values of the different inflation pressures, loads applied to the tyre and rolling velocities of the tyre in industry.

- Stating the boundary conditions and features used for each numerical model in the analysis.
- Validation of the numerical results.
- Interpretation of the numerical results to establish a safe operating envelope.
- Project conclusion and recommendations.

These activities were documented accordingly: Chapter 2 includes the literature study on the tyre structure and its materials, and the procedure used to calculate and model the temperature distribution in the tyre. The numerical modelling of the tyre geometry and its material properties are discussed in Chapter 3. A description of the boundary conditions and features used for each numerical model in the analysis is given in Chapter 4. Chapter 5 includes both the numerical and experimental results obtained. Chapter 6 includes the interpretation and evaluation of these results to establish a safe operating envelope. The project conclusion and recommendations for further investigation are discussed in Chapter 7.

Chapter 2

Literature study

This chapter reviews the literature on the tyre structure, the materials used in tyre manufacturing, the calculation of heat generation in a finite element representation of a rolling tyre, and the numerical analysis procedure used to model temperature distribution in the tyre cross-section.

2.1 Tyre structure: Components and terminology

Tyres are composite products that consist of various rubber compounds and steel, textile or synthetic reinforcements. Different rubber compounds are strategically placed in the tyre to give it the desired characteristics. Structural reinforcements are embedded in the rubber to enhance the strength of the tyre and give it dimensional stability. The different rubber compounds and structural components used in a radial ply tyre are shown in Figure 2.1.

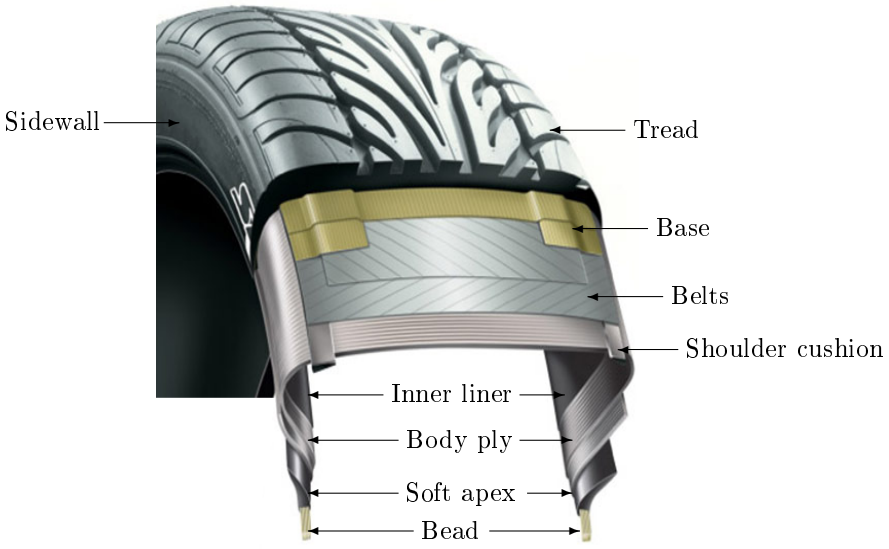

Figure 2.1: Radial tyre cutaway (adapted from Cartwright (2016))

The structural components include the bead, belts and body ply. The bead consists of bundles of high tensile steel wire which seats and seals the tyre on the rim. Belts are placed between the tread and body ply to protect the body ply by distributing road shocks. The body ply refers to the internal cord layer of the tyre that sustains load and absorbs shock. The body ply has directionality which determines how the tyre responds to lateral forces and tread contact with the road surface.

Earthmover tyres are typically manufactured in three basic configurations, namely: bias, bias belted, and radial ply tyres. The main difference of these configurations are based on the direction of its body plies. The body plies of bias and bias belted ply tyres consist of cords that run at alternate opposite angles across the centreline of the tyre, as seen in Figure 2.2(a). Bias belted ply tyres are the same as bias ply tyres with the addition of belts circling the tyre beneath the tread. Radial ply tyres have cords running radially from the outer bead to the inner bead, as seen in Figure 2.2(b). The expected tread and road surface contact interaction of bias and radial ply tyres are shown in Figures 2.3(a) and (b), respectively.

The different rubber compounds include the inner liner, soft apex, sidewall, shoulder, base and tread. The inner liner is a sheet of low permeable rubber laminated to the inside of the first casing ply of a tubeless tyre to ensure retention of air when the tyre is inflated. The sidewall is manufactured from a rubber compound that can flex without cracking and is located between the shoulder and bead. The base is a thin layer of rubber placed under the extruded tread to cover the ends of the cut belts and improve adhesion between the tread and belt plies. The apex provides a cushion between the rigid bead, the flexible inner liner and the body ply assembly. Shoulder inserts are placed on the body ply to help maintain a smooth belt contour and insulate the body ply from the belt edges (Gent and Walter, 2006). The tread is designed to resist wear and provide traction between the tyre and road.

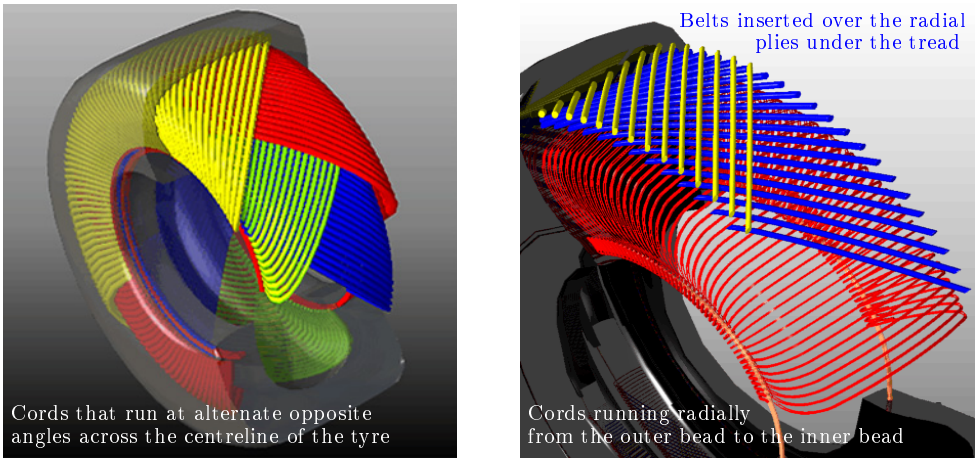

(a) (b)

Figure 2.2: The orientation and location of the cords used in (a) bias ply and (b) radial ply tyres (adapted from Michelin (2016))

Figure 2.3: Tread and road surface contact interaction during loading and cornering for (a) bias ply and (b) radial ply tyres (adapted from Hankook (2015))

2.2 Typical materials used in tyre manufacturing

This section gives an overview of the different materials used in tyre manufacturing. The structural components are discussed first, followed by the different rubber compounds used in manufacturing. The properties of each of these materials has a unique contribution to the overall performance of the tyre. The purpose of this section is to highlight the properties that must be taken into account to understand its material behaviour and contribution to the overall performance of the tyre.

The most common tyre reinforcement materials include rayon, aramid, and steel (Gent and Walter, 2006). The body ply and belts in earthmover tyres, only consist of carbon steel cords. Steel cords are preferred over textiles or other synthetic materials for these tyres, due to its enhanced strength, improved thermal conductivity, quicker handling response and longer tread life (Gent and Walter, 2006). The strength of the cords is primarily based on its configuration and carbon content.

The configuration of the steel cords used in tyre manufacturing are described according to a specific geometrical arrangement of the different components in its construction. The typical components found in these cords include filaments, strands and a wrap wire. These components are illustrated in Figure 2.4. The filament is a single fine metallic wire, and the strand is the combination of two or more filaments (Gent and Walter, 2006). The cord is referred to as the final product, which consist of the steel filaments that have been twisted and wound into multiple-strand bundles in a specific geometrical arrangement. The wrap is a single filament wrapped around a cord package to maintain compactness (Gent and Walter, 2006). This geometrical arrangement influences the cord behaviour and its strength. These cords therefore do not possess a specific Young's modulus, but an apparent Young's modulus that must be established from experimental tests (Bridon, 2016).

Pneumatic tyres usually contain a variety of rubber compounds, each designed to contribute some particular factor to the overall performance. Before rubber is processed, its natural composition consists of a highly-viscous liquid that can show elasticity when the long molecules are intertwined and entangled. During rubber processing these long molecules are joined together via sulphur or other equivalent accelerators to form chemical bonds known as crosslinks. This process is known as

vulcanisation and it is used to transform the viscous liquid to an elastic solid (Gent, 2012). The crosslinks help to form a permanent molecular network (Gent and Walter, 2006). The crosslinks and entanglements in a rubber polymer network are illustrated in Figure 2.5. This unique molecular structure is the basis of rubber elasticity and explains the internal viscous forces that exits between molecular chains.

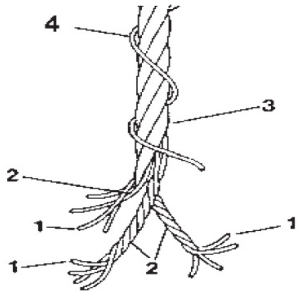

Cord components: (1) filaments, (2) strands, (3) cord and (4) spiral wrap

Figure 2.4: Components in the steel cords used for tyre manufacturing (adapted from Gent and Walter (2006))

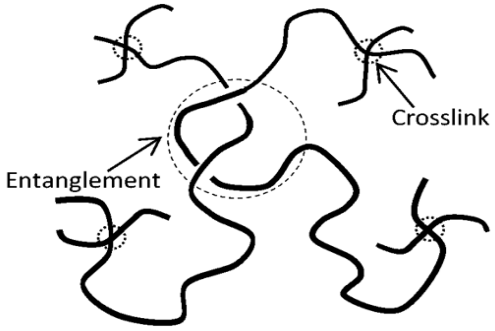

Figure 2.5: Crosslinks and entanglements in a rubber polymer network (Polymer Properties Database, 2015)

At elevated temperatures the molecular chains of the rubber will start to break down, causing charring and embrittlement (Gent, 2012). This degradation reaction leads to a loss of mechanical properties. Its effects are irreversible and cumulative following several heating events (Benoît *et al.*, 2009). This degradation process is known as either pyrolysis or thermo-oxidation. Pyrolysis can occur in the absence of oxygen, while thermo-oxidation can only occur in the presence of oxygen (Benoît *et al.*, 2009). Thus, pyrolysis or thermo-oxidation not only increases the pressure build-up in tyres, as mentioned in Chapter 1, but it also has irreversible effects on the mechanical properties of the tyre, which makes it even more difficult to predict its behaviour. As a result, the internal heat generation in earthmover tyres must be managed to the extent that it would prevent it from reaching critical temperatures that will cause the embrittlement of rubber.

The most common rubber polymers used in tyre manufacturing include natural rubber, styrene-butadiene rubber, polybutadiene rubber, butyl rubber, and halogenated butyl rubber. Natural rubber, styrene-butadiene rubber and polybutadiene rubber are generally used for the sidewall and tread, while butyl rubber or halogenated butyl rubber are used for the inner liner (McGarry (2007) and Clark (1981)). Other ingredients are added to the rubber polymer or blend of polymers to alter its chemical composition and give it the desired mechanical properties. These ingredients include: fillers, such as highly-developed carbon blacks, softeners, chemical protective agents, and sulphur or small amounts of zinc oxide (Gent and Walter, 2006).

By weight, carbon black is the most important additive to rubber compounds (McGarry, 2007). Carbon black enhances the modulus, hardness and thermal conductivity of the rubber compound. However, carbon black also increases the mechanical

energy losses, hysteresis loss and viscoelastic response to forces of the rubber compound (Clark, 1981). This unique influence on the mechanical properties of the rubber compound can be used to distinguish between the different rubber compounds used in the tyre and its expected behaviour.

2.3 Heat generation in a rolling tyre

Rubber can be defined as a hyper-viscoelastic material due to its unique molecular structure, as described in Section 2.2. If the viscous component is neglected, the hyperelastic behaviour of rubber can be represented by a hyperelastic material model, assuming that rubber is an incompressible and isotropic material, and its stress-strain behaviour is independent of strain rate. Hyperelastic material models include a description of elasticity in terms of a stored energy function, also known as the elastic strain energy density. This elastic strain energy density, along with the hysteresis in rubber, can be used to determine the heat generation in a rolling tyre (Tang *et al.* (2014), Smith *et al.* (2012) and Lin and Hwang (2004)). This section gives a description of the relation between the use of hyperelastic material models and the hysteresis in rubber to calculate the heat generation in a finite element representation of a rolling tyre.

2.3.1 Hyperelasticity

The relation between the use of hyperelastic material models and the elastic strain energy density in hyperelastic materials during deformation is discussed in this section. This relation is based on a review of the general elastic theory of hyperelastic material models given by Clark (1981).

Hyperelastic material models are based on the principle of perfect elasticity. Perfect elasticity implies immediate and complete recovery upon deformation. In thermodynamics, this behaviour can be described as a reversible process,

$$dE = TdS + dW \tag{2.1}$$

where dE is the change in internal energy of the system ($\mathrm{J/m^3}$), T is the absolute temperature of the system (K), dS is the change in entropy ($\mathrm{J/K\ m^3}$), and dW is the change in work done on the system per unit volume ($\mathrm{J/m^3}$). From this thermodynamic relation, it has been found that over a considerable temperature range, the stress is closely proportional to absolute temperature. This finding gives way to the conclusion that the material's elasticity lies principally within the entropy term. For rubber elongations above 10 %, and below large deformations causing crystallisation, the entropy will decrease on exention as the molecular chains straighten, and increase on retraction.

The description of rubber elasticity in terms of entropy allows for a relation between stress and internal energy based on molecular or atomic spacings. If it is assumed that the vector components of length of each chain changes is the same

ratio as the corresponding dimensions of the rubber specimen, the change in entropy can be determined from the changes in deformation of a network,

$$dS = -\frac{1}{2}Nk({\lambda_1}^2 + {\lambda_2}^2 + {\lambda_3}^2 - 3) \tag{2.2}$$

where N is the number of network chains per unit volume, k is the Boltzmann's constant (1.38064852 (10^{-23}) m^2 kg/ s^2 K), and λ_i are the principal stretch ratios in the three mutually perpendicular axes of strain for a pure homogeneous strain. The stretch ratio, λ, is defined as the ratio between the deformed length and the unreformed length,

$$\lambda = \frac{l}{L} \tag{2.3}$$

where l is the deformed length (m), and L is the unreformed length (m). If the deformation is not accompanied by a change in internal energy, $dE = 0$, which is evident for a reversible process, the work of deformation can be expressed in terms of entropy:

$$dW = -TdS \tag{2.4}$$

Assuming that volume changes can be neglected, the change in entropy of the system can be calculated from the principle stretch ratios given in Equation 2.2. For incompressibility the following relation holds:

$$\lambda_1\lambda_2\lambda_3 = 1 \tag{2.5}$$

This description is known as the general elasticity theory for large deformations of incompressible, isotropic elastic materials. This theory provides a description of material elasticity in terms of a stored energy function. The most widely used formulation of this description is the Mooney-Rivlin approach (Gent, 2012). In this approach, strain-energy representation of the material behaviour is based on a polynomial fit of its measured stress-strain behaviour. The calculation of the polynomial coefficients are based on the general elasticity theory and the stored energy function is expressed as a symmetric function of the three principal extension ratios λ_1, λ_2 and λ_3. These extension ratios are given in terms of the following strain invariants:

$$I_1 = \lambda_1^2 + \lambda_2^2 + \lambda_3^2 \tag{2.6}$$

$$I_2 = \lambda_1^2\lambda_2^2 + \lambda_2^2\lambda_3^2 + \lambda_1^2\lambda_3^2 \tag{2.7}$$

$$I_3 = \lambda_1\lambda_2\lambda_3 \tag{2.8}$$

Assuming incompressibility, $I_3 = 1$, and λ_3 is eliminated from Equations 2.6 and 2.7.

As a result, the stored energy is expressed in terms of two independent variables I_1 and I_2:

$$W = \sum_{i=0}^{\infty} \sum_{j=0}^{\infty} C_{ij}(I_1 - 3)^i (I_2 - 3)^j \tag{2.9}$$

Equation 2.9 is known as the most general form of the Mooney-Rivlin stored energy function. $(I_1 - 3)$ and $(I_2 - 3)$ are used to ensure that the stored energy will be zero for zero strain. Retention of the first two terms , $i = 1$, $j = 0$ and $i = 0$, $j = 1$ gives,

$$W = U = C_{10}(I_1 - 3) + C_{01}(I_2 - 3) \tag{2.10}$$

where U is the elastic strain energy density ($\mathrm{J/m^3}$), and C_{10} and C_{01} are the Mooney-Rivlin material coefficients (Pa). Equation 2.10 is known as the two-term Mooney-Rivlin strain energy density function. More terms can be introduced from Equation 2.9 to account for the upward curvature in the stress-strain curves at high elongation. However, the inclusion of these terms to fit the data, may result in unstable energy functions yielding non-physical results and should be used with caution (Gent, 2012).

From the derivations given in this section, it can be concluded that the stress-strain curve of a hyperelastic material, such as rubber, can be represented by a polynomial fit of the stress-strain data using a Mooney-Rivlin material model. This model includes the calculation of the elastic strain energy density in the rubber as a function of deformation. The use of the elastic strain energy density in the rubber which can be used for the calculation of heat generation in a rolling tyre, is discussed in Section 2.3.3.

2.3.2 Rubber viscosity

Rubber exhibits viscous behaviour due to the internal viscosity between molecular chains present, as described in Section 2.2. When rubber is subjected to cyclic deformation, such as the rolling of a tyre, the internal viscous forces cause a lag in the material recovery. This component is indicative of the cyclic energy loss, since rubbers tend to absorb more heat than they can dissipate during this process. The lost energy is known as hysteresis loss and is stored in the rubber as heat (Clark, 1981). Thus it can be assumed that the hysteresis loss in a rolling tyre is entirely responsible for the internal heat generation in this system ((Tang *et al.*, 2014) and (Lin and Hwang, 2004)). This hysteresis loss is a function of the hysteresis coefficient of a specific material ((Tang *et al.*, 2014) and (Lin and Hwang, 2004)). This section describes an approach that can be used to determine the hysteresis coefficient in rubber, which in turn, can be used to determine the lost energy stored in the rubber as heat.

Dynamic mechanical analysis (DMA) is a technique used to study and characterise materials such as the viscoelastic behaviour of rubber. DMA measures the viscoelastic properties of materials using dynamic oscillatory tests. During these tests a

sinusoidal stress is applied to the material and a sinusoidal strain is measured. The viscous component in the material will cause a lag of strain behind stress. This lag can be measured as a phase difference, δ. This phase difference is indicative of mechanical energy loss in each cycle and is known as hysteresis loss. For purely elastic materials, the phase difference will be 0° and 90° for purely viscous materials, as shown in Figure 2.6(a). For viscoelastic materials, the phase difference will be between 0° and 90°, as shown in Figure 2.6(b).

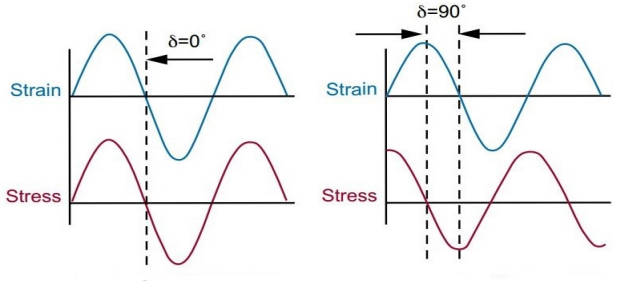

100 % Elastic behaviour 100 % Viscous behaviour

(a)

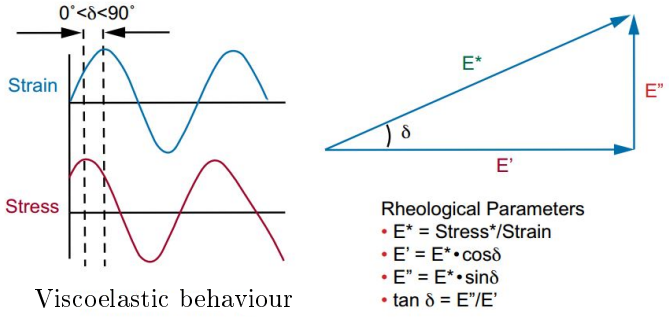

Viscoelastic behaviour

(b)

Figure 2.6: The phase lag for (a) purely elastic and viscous materials; (b) Viscoelastic materials and an illustration of the relation between the dynamic, storage and loss modulus (adapted from TA Instruments (2014))

The dynamic modulus, E^*, storage modulus, E', and loss modulus, E'', are typical parameters obtained from DMA. The dynamic modulus of a sample is indicative of the total energy in the system, the storage modulus is indicative of the sample's stiffness, and the loss modulus is indicative of the sample's ability to dissipate mechanical energy through molecular motion. The relation between the dynamic, storage and loss modulus is given by Equation 2.11 (Lin and Hwang, 2004), and illustrated in Figure 2.6(b).

$$E^* = \sqrt{(E')^2 + (E'')^2} \tag{2.11}$$

The hysteresis coefficient, H, of a material can be defined as the loss modulus di-

vided by the dynamic modulus, as seen in Equation 2.12 (Lin and Hwang, 2004). As a result of this definition the assumption can be made that the hysteresis coefficient of a material can also be defined as the lost energy divided by the total energy in a cyclic system (Lin and Hwang, 2004),

$$H = \frac{E''}{E^*} = \frac{Loss\ part}{Total\ part} \tag{2.12}$$

where the *Loss part* refers to the lost energy, and the *Total part* refers to the total energy in the system. Thus, for a cyclic system represented by a rolling tyre, it can be assumed that the total energy in the system can be represented by the total elastic strain energy density in the rubber, and the lost energy is due to hysteresis in rubber. Using the hysteresis coefficient of a specific rubber compound obtained from DMA and the total elastic strain energy density obtained form the hyperelastic material model, the lost energy can be calculated using Equation 2.12. The exact calculation of the lost energy and heat generation in a finite element representation of a rolling tyre, is given in Section 2.3.3.

2.3.3 Finite element representation

In this section the relation between the total elastic strain energy density, lost energy due to hysteresis, and the calculation of the heat generation in a numerical model of a rolling tyre is discussed. Assuming that the lost strain energy density in a rolling tyre completely contributes to internal heat generation in the tyre, the lost strain energy density can be calculated by rewriting Equation 2.12 as,

$$U_{LSED} = HU_{TSED} \tag{2.13}$$

where U_{TSED} is the total strain energy density ($\mathrm{J/m^3}$), and U_{LSED} is the lost strain energy density in the system ($\mathrm{J/m^3}$). Considering a numerical model that consists of a finite number of elements, the total strain energy density of a element node for each increment during one revolution of the tyre can be calculated as,

$$U_{tsed} = \sum_{i=1}^{n} \Delta U_i \tag{2.14}$$

where U_{tsed} is the total strain energy density of an element node ($\mathrm{J/m^3}$), n is the number of times the elastic strain energy increases from increment to increment, and ΔU_i is the increase in elastic strain energy density for the corresponding increment ($\mathrm{J/m^3}$). The total strain energy density of the element, U_{TSED}, can be calculated by averaging the nodal values over the element. Using the total strain energy density of the element and the hysteresis coefficient of the relevant rubber compound obtained from DMA, the lost strain energy density for each element can be calculated from Equation 2.13.

The heat generation rate in each element can be calculated as,

$$\dot{q}_g = U_{LSED} f \tag{2.15}$$

where $\dot{q}_g$ is the heat generation rate in each element (W/m^3), and f is the rolling frequency of the tyre (Hz). The rolling frequency of the tyre can be defined as the velocity divided by the circumference of the rolling tyre,

$$f = \frac{V_c}{L_r} = \frac{V_c}{2\pi R_r} \tag{2.16}$$

where V_c is the velocity (m/s), L_r the circumferential length (m) of the rolling tyre calculated from the rolling radius R_r of the tyre (m). From Equation 2.16, it can be concluded that the heat generation rate will be proportional to the rolling velocity of the tyre.

By using the approach described in this section, it can be concluded that: the total elastic strain energy density of each element in a numerical model of a rolling tyre can be obtained from its deformation which is described by its hyperelastic material model; the hysteresis coefficient of a specific rubber compound can be obtained from DMA and; the lost strain energy density of each element can be calculated using Equation 2.13. Assuming the lost strain energy density completely contributes to heat generation in a rolling tyre, the heat generation rate of each element can be calculated using Equation 2.15. The heat generation rate can be used in a thermal model of the tyre cross-section to represent the temperature distribution during steady-state rolling. The implementation of the heat generation rate to represent the temperature distribution in tyre cross-section in the numerical analysis procedure, is discussed in Section 2.4.2.

2.4 Numerical modelling considerations

This section describes the aspects that must be considered when developing a numerical model of a tyre and the analysis procedure that will be used to simulate the temperature distribution in the cross-section of a rolling tyre. This description is based on the findings of Maritz (2015) and similar studies completed by other authors in literature.

2.4.1 Modelling of the tyre structure

Different commercial software packages are available to numerically model the geometry and components in a tyre. Various techniques are integrated into these packages to simplify the tyre geometry and save computational time (Gent, 2012). MSC.Marc/Mentat has been used by Maritz (2015), Kováč and Krmela (2012) and Ghoreishy (2008) for the numerical modelling of passenger vehicle structures and to simulate its behaviour. MSC.Marc/Mentat 2014.0.0 was identified as the latest version of this specific software package and was therefore selected to numerically model the tyre structure and simulate its behaviour. This software package will be

referred to as Marc/Mentat throughout this document. This section describes the different techniques integrated into this software package to numerically model the tyre structure and its components.

Tyres consist of different rubber compounds with specific properties that must be modelled individually to accurately represent the numerical response of the tyre Maritz (2015). Other studies which includes the numerical modelling of the different rubber compounds in the tyre were completed by Kováč and Krmela (2012), Ghosh (2011), Ghoreishy (2006), and Korunović *et al.* (2007). Figure 2.7 indicates the expected regions of the different rubber compounds modelled in radial ply truck and bus tyres. The numerical model developed in this project will include the different rubber compounds established from tests done on the tyre under consideration.

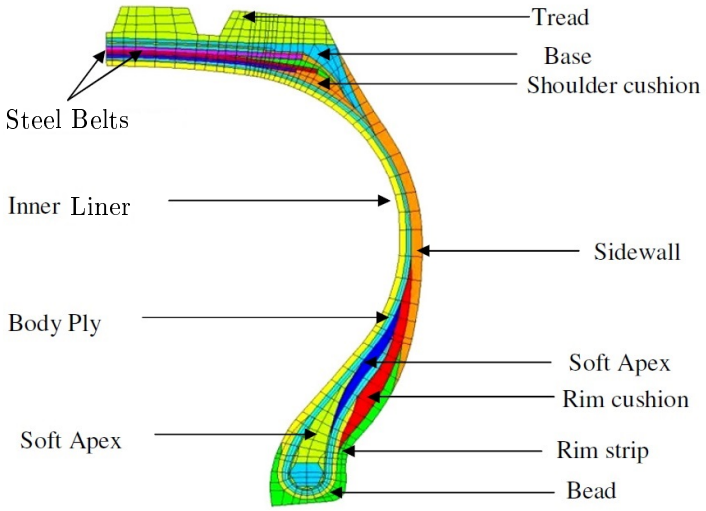

Figure 2.7: Numerical representation of the rubber compounds and structural components modelled in radial ply truck and bus tyres (adapted from Ghosh (2011))

Maritz (2015) recommended that the material behaviour of each compound must be established from experimental tests done on the actual tyre. Hyperelastic material models are typically used to represent the non-linear elastic behaviour of rubbers. Various hyperelastic material models are supported in Marc/Mentat, including the Mooney-Rivlin material model. When using hyperelastic material models, the appropriate experimental loading sequences and realistic strain levels are required to capture the material behaviour (Miller, 2002). The basic states of strain should therefore be represented in the material data. The basic states of strain of rubbers include simple tension and compression (Miller, 2002). Pure shear can be neglected, since rubbers are assumed to be isotropic materials. Marc/Mentat supports uniaxial test data to fit hyperelastic models. Thus, both uniaxial tensile and compression test data will be considered to numerically model the stress-strain behaviour of the rubber compounds identified in the tyre under consideration.

Structural reinforcement, such as the body ply and belts, are typically modelled with `Rebar` elements in Marc/Mentat. These elements can be placed inside the rubber elements using the `Insert` option. The `Insert` option ties the degrees of freedom of the nodes in the inserted element list to the corresponding degrees of freedom of the nodes in the host body elements based on their isoparametric location in the elements (MSC, 2014*b*). The material properties of the `Rebar` elements are defined according to its Young's modulus, Poisson's ratio and density. The size and orientation of the element is defined by the `Rebar` area, number of `Rebar` layers, number of `Rebars` per unit length and the `Rebar` orientation with respect to the selected reference axis. This method has been used by both Maritz (2015) and Kováč and Krmela (2012), and will be used in this project as well.

The precise modelling of the bead is not as important as the correct modelling of its strength Maritz (2015). The bead seats the tyre on the rim during the numerical inflation and rolling analysis procedure. Maritz (2015) modelled the bead as a solid ring with isotropic material properties using only one element. However, more elements can be used to fit the mesh accordingly, as seen in Cho *et al.* (2013). A similar method will be used to model the bead in this project. Another aspect to consider is the modelling of the tread pattern. Maritz (2015) modelled only the circumferential grooves in the tread area, and not the actual tread pattern of the tyre. It can be assumed that the exact modelling of the tread pattern can be neglected if it does not significantly contribute to the purpose of the study. Studies that usually include the actual tread pattern are typically done when the influence of the tread pattern on the rolling resistance of the tyre are investigated, as seen in Cho *et al.* (2013). Other authors that also modelled a rolling tyre using only the circumferential grooves, include Ghoreishy (2006) and Tang *et al.* (2014). Based on these findings the numerical model developed in this project will include only the circumferential grooves of the tyre.

First order quadrilateral and hexahedral elements will be used to model the 2-D and 3-D geometry of the tyre, respectively. These elements are considered sufficient to represent the large strains associated with rubber deformation. Furthermore, first order elements were preferred, since it uses less computational resources than second order elements, which is crucial considering the computational requirements for modelling the rolling of a tyre. Other authors that used similar elements include Kováč and Krmela (2012), Ghoreishy (2006), and Korunović *et al.* (2007).

Since rubber experiences large strains and deformations under loads, it must be modelled with an element which is formulated to handle its incompressibility (Gent, 2012). This is generally accomplished by using `Full & Herrmann Formulation` elements in Marc/Mentat. These elements are formulated with displacement and pressure as variables (MSC, 2013). This formulation not only enables these elements to accommodate the incompressibility of rubber, but makes it compatible with the elements specified for the non-elastic components, such as the bead. Thus, the rubber and the bead will be modelled with these elements.

2.4.2 Numerical analysis procedure

The numerical modelling of the temperature distribution in the cross-section of a rolling tyre can be achieved by using either a coupled structural and thermal analysis, or an uncoupled analysis (Maritz, 2015).

In a coupled analysis, a structural and thermal analysis is done simultaneously. The tyre is rolled until steady-state is reached and the heat generation in the tyre is extracted. This procedure is extremely computationally expensive, since simulating a rolling tyre is a computationally expensive process in itself, and the tyre must be rolled for a large number of revolutions to reach steady-state. In an uncoupled analysis, the structural and thermal analysis are separated. A structural model is solved first, in which the tyre is inflated and a load is applied to the tyre. The loaded tyre is rolled for at least two revolutions and the elastic strain energy density for one revolution is extracted. The elastic strain energy density is used to calculate the heat generation rate in the tyre according to the method given in Section 2.3.3. The heat generation rate, along with other heat transfer boundary conditions, are implemented into a thermal model to represent the temperature distribution in the tyre cross-section.

It can be assumed that the tyre model only has to be rolled for two revolutions to calculate its steady-state heat generation in an uncoupled analysis, since the heat generation in the tyre is ultimately a function of the rubber deformation, which will be the same for each revolution. This assumption is based on the use of a hyperelastic material model to represent the rubber behaviour. The derivation of hyperelastic material models is based on the principle of perfect elasticity, which implies complete recovery upon deformation. Thus, the deformation in each revolution will be the same, and consecutively the heat generation in each revolution for this analysis. It can therefore be concluded that an uncoupled analysis requires more steps, but less computational resources than a coupled analysis, since the tyre does not need to reach steady-state to calculate its heat generation, and is therefore preferred. This procedure has been used by Maritz (2015), Lin and Hwang (2004), and Tang *et al.* (2014), and will be used in this project as well.

2.4.3 Effect of different operating conditions

The temperature distribution in the tyre cross-section is a function of several factors, of which the inflation pressure of the tyre, the load applied to the tyre, and the rolling velocity of the tyre will be considered in this project. These factors have been identified by Maritz (2015) and Lin and Hwang (2004) as some of the factors that have the most significant contribution to the heat generation in a tyre and can be controlled externally. By adjusting these parameters the heat generation in the tyre can be altered to eventually prevent the tyre from reaching critical temperatures. This project will therefore include a parametric study of the temperature distribution in the tyre cross-section as a function of these operating conditions to establish a safe operating envelope. The values of the different inflation pressures, applied loads

and rolling velocities the numerical model will be subjected to will be established from the operating conditions the tyre under consideration are typically exposed to in industry.

2.5 Conclusion

This chapter provides a general overview of the factors that must be considered to develop the numerical model of an earthmover tyre, as well as the procedure used to simulate the temperature distribution in the tyre cross-section. The Mooney-Rivlin hyperelastic material model is derived from first principles to confirm the numerical modelling of rubber based on a polynomial fit of its stress-strain behaviour during deformation. This derivation includes a description of rubber elasticity in terms of a stored energy function, which is also known as the elastic strain energy density in the rubber during deformation. The elastic strain energy density, along with the hysteresis coefficient, can be used to calculate the lost energy stored in the tyre as heat during rolling. The lost energy can be used to calculate the heat generation rate in the tyre, and can be implemented into a thermal model to represent the temperature distribution in the tyre cross-section during steady-state rolling.

MSC.Marc/Mentat 2014.0.0 (Marc/Mentat) was identified as latest version of the commercial software packages that will be used to numerically model the tyre structure and simulate its behaviour. An uncoupled analysis can be used to simulate the temperature distribution in the cross-section of a tyre at steady-state rolling. A parametric study of the temperature distribution in the rolling tyre will be done at different inflation pressures, applied loads and rolling velocities to establish a safe operating envelope. The value of these parameters will be similar to the operating conditions used in industry.

Chapter 3

Numerical modelling: Tyre structure and material properties

This chapter describes the results of the experimental tests done on a 23.5R25 earthmover tyre to numerically model its geometry and material properties. Earthmover tyres are extremely expensive and therefore Anglo donated a segment of a used tyre to Stellenbosch University for the purpose of this project. A side view and cross-sectional view of the donated tyre segment is shown in Figures 3.1(a) and (b), respectively. Figure 3.1(c) shows the remaining tread pattern of the tyre.

It should be noted that the analysis in this project considers the heat generation in a new tyre, although the tyre geometry was originally obtained from measurements done on the donated tyre segment, which only had one third of its tread remaining. The geometry developed for the numerical model was therefore adjusted to be consistent with that of a new tyre. The numerical modelling of the tyre geometry will be discussed in the following section. The material properties of the components identified in the tyre will be discussed thereafter.

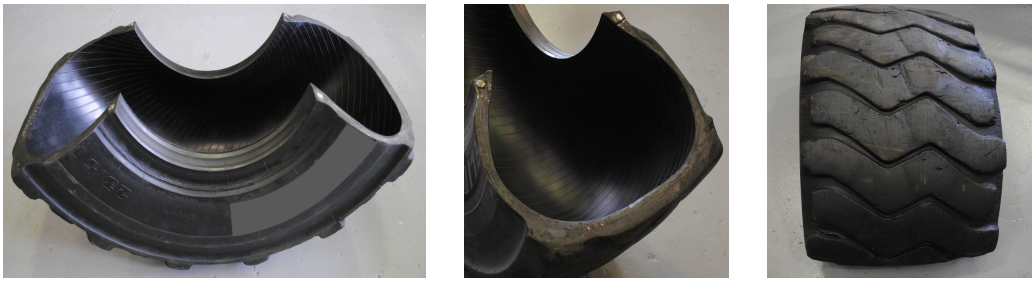

(a) (b) (c)

Figure 3.1: (a) Side view of the earthmover tyre segment donated to Stellenbosch University by Anglo; (b) Cross-sectional view and (c) remaining tread pattern of the donated tyre segment

3.1 Tyre geometry and specifications

This section describes the numerical modelling of the tyre geometry, the adjustments made to the measured geometry, and the numerical modelling of the rim profile.

The cross-section of the donated tyre was measured with a touch probe computer numerical control (CNC) digitising machine to model the tyre profile. The measured points were imported into Autodesk Inventor Professional 2016 (Inventor) to convert the points to continuous splines. This geometry was imported into MSC.Apex Eagle and adjusted to be consistent with that of a new tyre.

Since the tyre segment had only one third of its tread remaining, the tread depth and tyre height had to be adjusted. These adjustments were made according to the tread depth and thus the tyre height of a new tyre provided by the manufacturer's specifications. A summary of these specifications are given in Appendix A. The adjusted geometry was imported into MSC.SimXpert 2013.1 and meshed. The meshed model was imported into Marc/Mentat for pre- and post-processing. Figure 3.2 illustrates the resulting 2-D tyre geometry developed for the numerical model. This illustration includes the circumferential grooves of the tread of a new tyre, which cannot be seen in Figure 3.1(c) since it has been worn off.

The rim profile was created in Inventor and imported into Marc/Mentat. The rim size and dimensions were obtained from the tyre manufacturer's specifications. Figure 3.2 includes an illustration of the rim profile. The rim dimensions used for the numerical model are summarised in Appendix A.

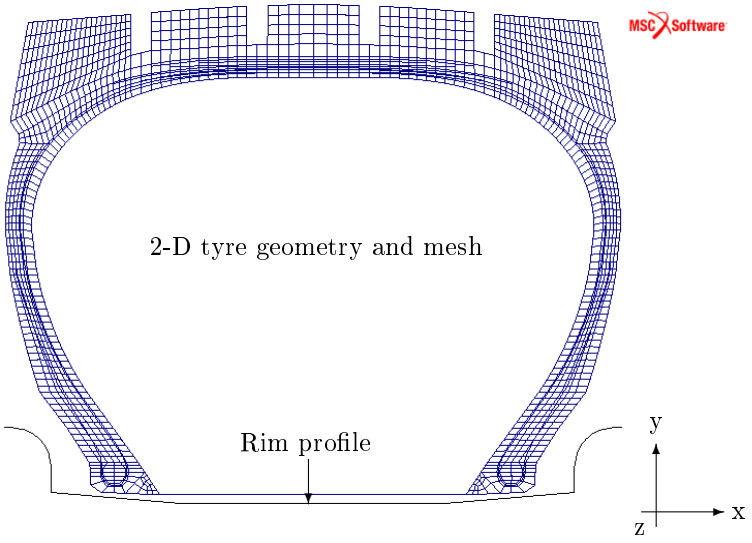

Figure 3.2: 2-D numerical tyre geometry, rim profile and mesh

3.2 Tyre components

The structural components and rubber compounds of the earthmover tyre were identified from the visual inspection of the donated tyre segment. According to the manufacturer's specifications, the tyre under investigation had a radial ply construction and therefore the different components identified in the tyre were labelled according to the description of the tyre structure given in Section 2.1.

The structural components were identified from tread and sidewall cut-outs of the provided tyre segment. These components include a radial steel body ply, five steel belt plies, and a bead bundle which consists of seventy-two individual wires. Figure 3.3 shows the structural components identified in the tyre.

In tyre manufacturing, the different rubber compounds are applied separately and sequentially to the tyre. The outline of these compounds can be identified in the tyre cross-section if its surface is evened and buffed. Thus, the surfaces of the tread and sidewall cut-outs were buffed using a grinder and P100 Aluminium Oxide sanding disks to identify the outline of the different rubber compounds in the tyre. These compounds included the inner liner, inner filler, soft apex, sidewall, shoulder, base and tread. Figure 3.3 shows the different rubber compounds identified in the tyre.

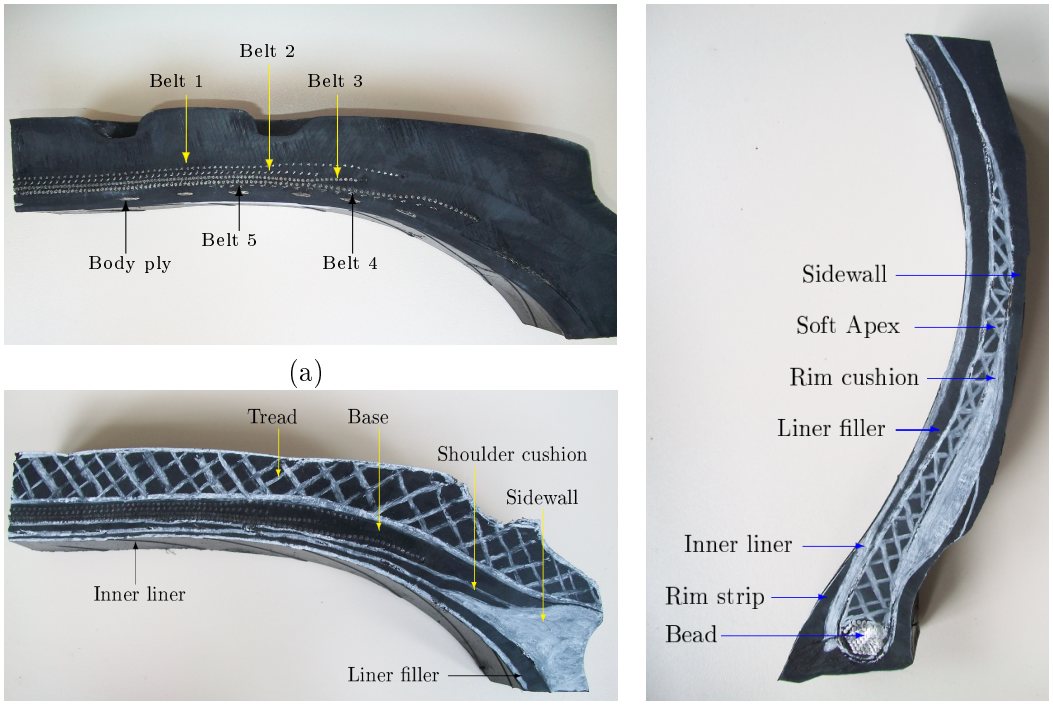

Figure 3.3: (a) Body ply and steel belt reinforcement identified in a tread cut-out of the tyre; (b) The different rubber compounds identified in a tread cut-out of the tyre; (c) The different rubber compounds and bead bundle identified in a sidewall cut-out of the tyre

3.3 Numerical modelling of the structural components

The belts and body plies were modelled using `Rebar` elements in Marc/Mentat. `Rebar` elements are defined according to its area, number of `Rebar` layers, number of `Rebar` elements per unit length and `Rebar` angle with respect to the selected reference axis. The material properties of these elements are defined according to its Young's modulus, Poisson's ratio, and density. Although the bead was modelled with solid elements and not `Rebar` elements, its Poisson's ratio, density and Young's modulus must be defined for the numerical model. This section describes the results of the tests done to obtain the value of each of these parameters.

3.3.1 Belt orientation and spacing

From Figure 3.3 it can be seen that the belts and body ply in the tyre consist of a number of steel cords. The definition of `Rebar` elements used to model the belts and body ply are based on the properties of these cords. This section describes the tests done to obtain the cord area, the number of cord layers in the belt or ply, the number of cords per unit length and the cord angle with respect to the selected reference axis.

The orientation and spacing of the steel cords used for each belt and the body ply were established from visual inspection. Pieces of the tyre were cut from the donated segment and burnt in an open-flame set-up to separate the steel components from the rubber until the orientation of each ply could be seen and the cords could be separated from it. The cord orientations were obtained by measuring its angle with a protractor. The measured cord angles with respect to the positive z-axis are shown in Figure 3.4.

The overall diameter the different cords were measured using a 0.01 resolution digital vernier to calculate the area of the cords. The cords used in belts 1, 2, 3, 4, and the body ply had an overall diameter of 0.0015 m, the cords used in belt 5 had an overall diameter of 0.0010 m. The resulting modelling parameters are given in Table 3.1.

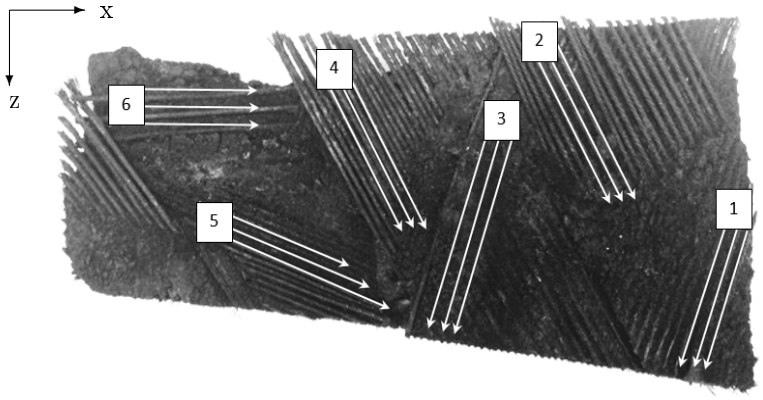

Figure 3.4: Cord angle with respect to the positive z-axis of: (1) belt 1 (-45°), (2) belt 2 (30°), (3) belt 3 (-38°), (4) belt 4 (30°), (5) belt 5 (70°) and (6) the body ply (90°) shown on a burnt piece of the actual tyre

Table 3.1: Modelling parameters used for the `Rebar` elements

	Layers	Rebar area (10^{-6} m^2)	Rebars per unit length (#/m)	Rebar angle
Belt 1	1	1.7670	150	-45°
Belt 2	1	1.7670	150	30°
Belt 3	1	1.7670	222	-38°
Belt 4	1	1.7670	222	30°
Belt 5	1	0.7854	500	70°
Body Ply	1	1.7670	200	90°

In order to verify the results obtained from visual inspection, similar pieces of tyre were cut from the donated segment and sent for computed tomography (CT) scans. A CT-scan is an X-ray procedure that generates cross-sectional views and three-dimensional images of a structure with the aid of a computer. The scan was used to evaluate the cord spacing and angle of each belt and the body ply within its original configuration as it is embedded in the tyre rubber. The results were consistent with the measured results. The results of the CT-scan are given in Appendix B.

3.3.2 Material properties

This section describes the results of the procedures used to establish the Young's modulus, Poisson's ratio, and density of the bead wire and the cords used in the belts and body ply. These procedures include visual inspection of the cord arrangement and uniaxial tensile tests performed on each component.

As mentioned in Section 2.2 the cords used in tyre manufacturing typically consist of multiple steel filaments with a specific geometrical arrangement (Gent and Walter, 2006). The cords of the tyre under investigation were selected from the donated tyre segment to inspect its arrangements. The cord arrangements were defined according to the convention shown in Figure 3.5. The cords used in belts 1 and 2 had a multi-strand arrangement consisting of three strands with six filaments each (3 x 6). The cords used in belts 3 and 4, and the body ply had a single strand arrangement consisting of twenty-seven filaments (1 x 27). The cords used in belt 5 had a single strand arrangement consisting of twelve filaments (1 x 12).

The cord arrangement influences its overall stress-strain behaviour and therefore its Young's modulus was established from experimental tests (Bridon, 2016). In order to obtain the strength of the bead wire, its Young's modulus was also determined experimentally. Thus, three sets of uniaxial tensile tests were completed for each component. The average of the test sets were used to fit a linear curve of the test data. The equipment, methodology, tensile tests data, and influence of different cord arrangements on the experimental data are discussed in Appendix C.

From the results obtained in Appendix C, it was concluded that the cords with similar arrangements yielded similar results. Since the cords used for belts 1 and 5,

and the body ply each represents a different arrangement, only the stress-strain curves of these cords are included in this section. The stress-strain curve of the bead wire is included in this section as well. The stress-strain curves of the cords used in belts 1, 5 and the body ply are given in Figures 3.6, 3.7 and 3.8, respectively. The stress-strain curves for the bead wire is given in Figure 3.9. These curves include the average of the tensile test data sets and a linear approximation of the average data used to obtain the slope of the curve.

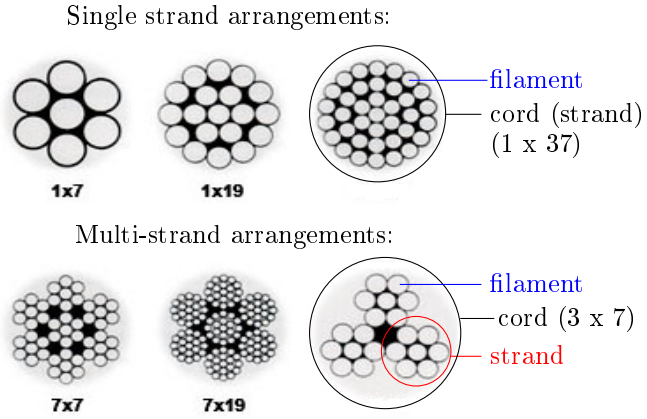

Figure 3.5: Examples of different cord arrangements, classified according to its number of filaments and strands (adapted from Lam Hong (2014))

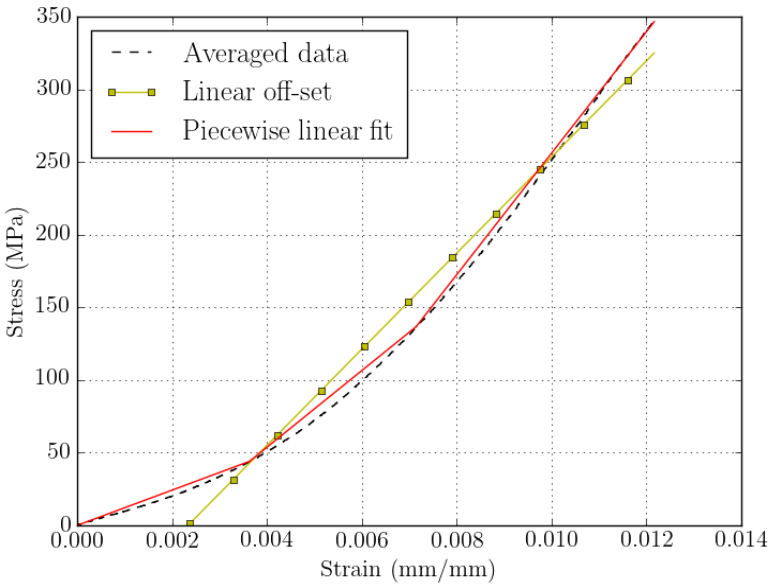

Figure 3.6: Stress-strain curve for the cords used in belt 1: the average of the three uniaxial tensile test sets, a piecewise linear fit of the average data and a linear curve fit of the average data at a 0.0024 (mm/mm) strain offset

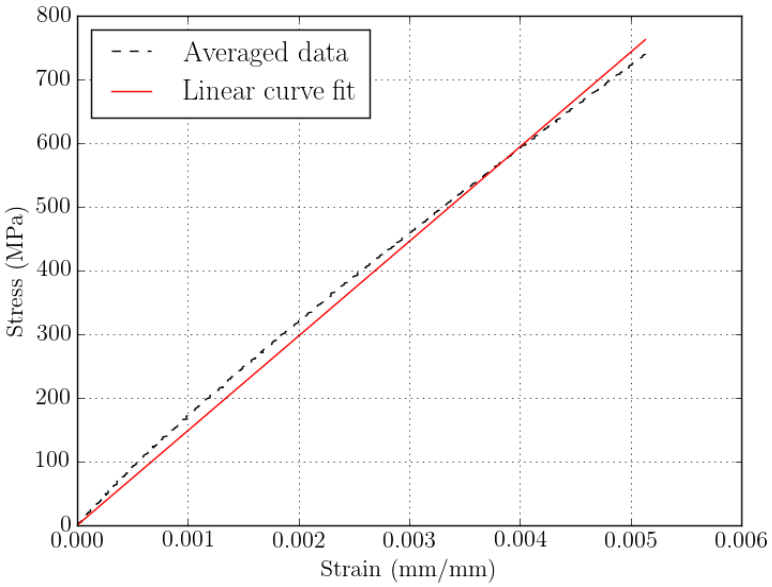

Figure 3.7: Stress-strain curve for the cords used in belt 5: the average of the three uniaxial tensile test sets and a linear curve fit of the average data

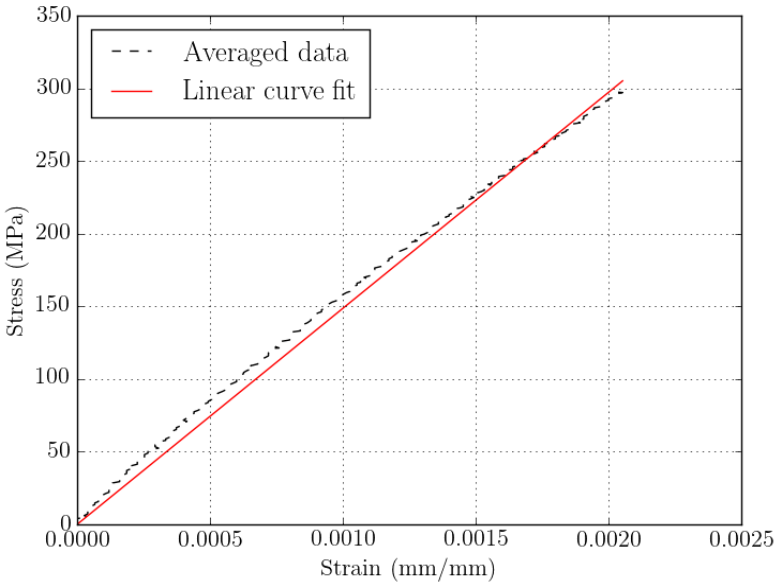

Figure 3.8: Stress-strain curve for the cords used in the body ply: the average of the three uniaxial tensile test sets and a linear curve fit of the average data

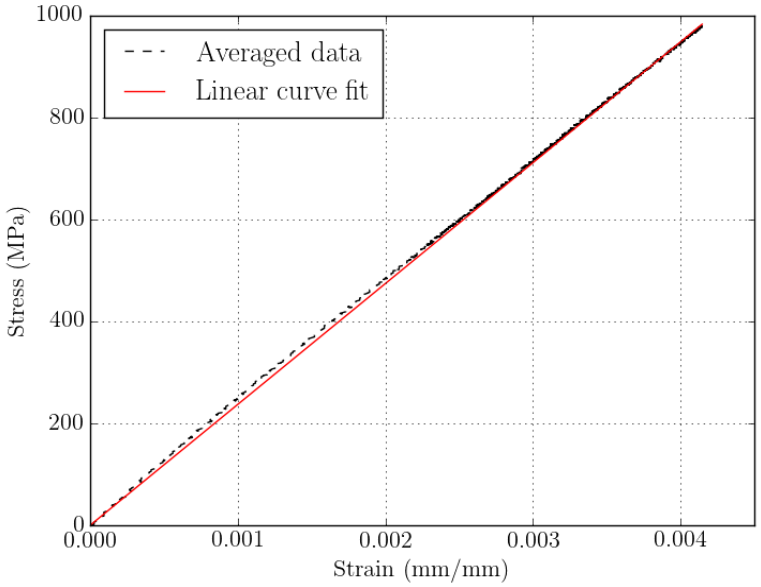

Figure 3.9: Stress-strain curve for the wires used in the bead: the average of the three uniaxial tensile test sets and a linear curve fit of the average data

It should be noted that the stress-strain curve of the average tensile test data shown in Figure 3.6 is somewhat non-linear. This non-linear behaviour is expected, due to the cord arrangement, which is discussed in further detail in Appendix C. Ideally, this non-linear curve can be represented by a piecewise linear fit, as seen in Figure 3.6. However, the modelling of this fit for a linear-elastic material in Marc/Mentat, tends to unnecessarily overcomplicate the numerical model. Alternatively, a linear curve fit of the test data at a strain offset of 0.0024 (mm/mm) was used to evaluate its influence on the numerical results. This approximation yielded a variation in the strain and deformation results of less than 2 %. This variation was considered tolerable for the purpose of this project, and the linear approximation was therefore used instead. This linear approximation is included in Figure 3.6.

The Young's modulus of the cords and bead wire were calculated from the slope of its respective linear curve fits shown in Figures 3.6 to 3.9. The resulting Young's modulus of each component is given in Table 3.2.

The materials used for the cords used in tyre manufacturing, range from AISI 302, 303, 304 and 316 stainless steel (Bell, 2010), or AISI 1005 to 1090 carbon steel, depending on its carbon content (Gent and Walter, 2006). Although these materials have different tensile strengths, their Poisson's ratio, density and Young's modulus are quite similar, ranging from 0.27 to 0.3, 7 850 to 8 000 kg/m^3, and 190 to 210 GPa, respectively. Thus, a Poisson's ratio of 0.3 and density of 7 850 kg/m^3 were selected for the structural components. A Young's modulus of 210 GPa was used as an estimate to compare the calculated Young's modulus. The resulting properties of each component are given in Table 3.2.

From Table 3.2 it can be seen that the Young's modulus of the cords used for belt 1 and 2 is the lowest of all the components, and it is much lower than 210 GPa. This low modulus is expected due to the cord arrangement. The cords used in belts 1 and 2 had a multi-strand arrangement which requires a high level of twist (Gent and Walter, 2006). An increase in the level of twist allows the cords to have a larger degree of flexibility during bending (Anzor, 2016). This property allows the cords to absorb and distribute most of the road shock to protect the body ply and the belts underneath.

The main purpose of belts 3 and 4 and the body ply is to provide strength and dimensional stability to the tyre (Gent and Walter, 2006). Thus, the cords used in these belts must have a higher Young's modulus than that used in belts 1 and 2 to provide the necessary stiffness and strength to the tyre and therefore the higher Young's modulus obtained for cords used in belts 3 and 4 and the body ply is as expected. Furthermore, the higher Young's modulus is achieved by altering the cord arrangement. The cords used in belts 3 and 4 and the body ply had a single strand arrangement. A single strand arrangement requires a lower level of twist than a multi-strand arrangement and consequently decreases its flexibility, but increases its stiffness.

The high Young's modulus of the bead wire given in Table 3.2 is expected, since high tensile carbon steel wires are typically used to properly seat and seal the tyre on the rim (Gent and Walter, 2006).

Based on these findings, it can be concluded that the results obtained in this section are viable and can be used to numerically model the structural components in the tyre.

Table 3.2: Young's modulus, Poisson's ratio and density of the cords in the belts and body ply, and the bead wire

	Young's modulus (GPa)	Poisson's ratio	Density (kg/m^3)
Belt 1 & 2	32.34	0.3	7870
Belt 3 & 4	148.59	0.3	7870
Belt 5	148.51	0.3	7870
Body ply	148.59	0.3	7870
Bead	237.14	0.3	7870

3.4 Rubber compounds: Material properties and stress-strain behaviour

This section describes the results of the procedures used to identify the rubber compounds considered for the numerical model and its corresponding material properties and the numerical modelling of its stress-strain behaviour. These properties include the Shore A scale durometer hardness of the rubber compounds, the stress-strain behaviour of the rubber compounds in tension and compression, the density of the rubber compounds and the hysteresis coefficient of the rubber compounds considered for the numerical model.

3.4.1 Hardness

The hardness of the rubber compounds used in tyre manufacturing can be related to the amount of carbon black added to the compound during processing. Carbon black is a filler used to enhance the strength of rubbers during processing, which consequently increases its hardness as well. The Shore A scale durometer hardness of the rubber compounds identified in the tyre under investigation was measured to establish a relation between of the different compounds used in the tyre. The results are given in Table 3.3. The equipment, methodology and results of the hardness measurements are discussed in Appendix D.

Table 3.3: Classification of the different rubber compounds identified in the tyre segment according to its measured Shore A scale durometer hardness

Group	Rubber compound	Durometer hardness Shore A
1	Rim strip	73.6
	Tread	72.1
2	Base	64.2
	Liner filler	62.1
	Sidewall	60.2
	Rim cushion	59.4
	Soft apex	58.1
	Shoulder cushion	56.8
3	Inner liner	54.1

To avoid the numerical modelling of nine different rubber compounds, the rubber compounds with similar hardness values were grouped accordingly. A specific rubber compound was selected from the group to represent the entire group. These compounds were selected based on either its representation of volume in the tyre and thus its contribution to heat generation in the tyre, or by its unique hardness value. Thus, the inner liner, sidewall and tread rubber compounds were selected from each group to represent the rubber compounds in the group. The material properties of these compounds were established for the numerical model.

3.4.2 Hyperelastic material model

As mentioned in Chapter 2 the stress-strain behaviour of rubber can be represented numerically using hyperelastic material models. Various hyperelastic material models are supported in Marc/Mentat, of which the Mooney-Rivlin material model will be used for this project. This material model was selected due to its simplicity, since the model is based on a polynomial fit of the test data of the rubber deformation during loading, independent of any molecular theory (Clark, 1981). The numerical modelling inner liner, sidewall and tread rubber test data used to represent its material behaviour will be discussed in this section.

From Section 2.4.1 in can be concluded that the Mooney-Rivlin material model of rubber compounds can be obtained by fitting uniaxial tensile and compression data in Marc/Mentat. Thus, three sets of tensile tests were completed for the inner liner rubber. Three sets of tensile and compression tests were completed for the sidewall and tread rubber compounds. Only tensile tests were performed on the inner liner rubber since it was too thin for compression tests, however, it was modelled separately due to its unique hardness value given in Table 3.3. The average value of the data sets were used to numerically model its corresponding stress-strain curves. The equipment, methodology, and uniaxial test results are discussed in Appendix C.

When fitting test data to numerically model the behaviour of rubber using a Mooney-Rivlin material model, the number of terms included in the polynomial given in Equation 2.9 in Section 2.3.1 must be considered beforehand. Generally, a two-term Mooney-Rivlin material model is preferred over a three-term model, since a simpler model tends to be more stable over a wider range of strain and is less computationally expensive (MSC, 2013). However, when including both tension and compression test data three-term models are recommended (MSC, 2013). Since no rubber physics are embedded in the equations, the inclusion of higher terms to obtain a better fit should be used with caution. Using higher order terms to obtain a better fit, may result in unstable energy functions yielding non-physical results (Gent, 2012).

In order to evaluate the physicality of the results, other modes of strain should be included when fitting the data. Marc/Mentat automatically plots the other modes of strain based on the selected material model, although the data of these modes were not included. One of these modes include the biaxial response of the rubber. From the observations of natural rubber it is recommended that the tensile biaxial response of the rubber compound should be about 1.5 to 2.5 times its uniaxial tensile response (MSC, 2010). This estimate was also used to evaluate the response of the selected material model.

The uniaxial test data of the rubber compounds were fitted using both two-term and three-term Mooney-Rivlin material models. The two-term model showed good agreement with uniaxial test data, and its biaxial response was within the estimated range. The three-term model showed a slightly better fit than the two-term model, but it's biaxial response greatly exceeded the estimated range, and therefore the two-term model was used instead.

The average tensile stress-strain data and two-term Mooney-Rivlin fit of the inner liner rubber are shown in Figure 3.10. The average tensile and compression stress-strain data of the sidewall, tread and rim strip rubber are shown in Figures 3.11, 3.12 and 3.13, respectively. The average tensile and compression stress-strain data of tread and rim strip rubber are both based on the test data of the tread rubber, but at different strain ranges, since the rim strip typically experiences larger strains than the tread. The two-term Mooney-Rivlin model of the tensile and compression data of the respective rubber compounds are included in Figures 3.11, 3.12 and 3.13.

An extrapolated fit of the two-term Mooney-Rivlin material models using only tensile test data for the respective rubber compounds are shown in Figures 3.10, 3.12 and 3.13. This fit was included to compare the use of including both tensile and compression test data to model the material behaviour, rather than using only tensile test data. From the results obtained it can be concluded that using both tensile and compression data gives a better fit of the actual material response, rather than using only tensile test data and was therefore used instead.

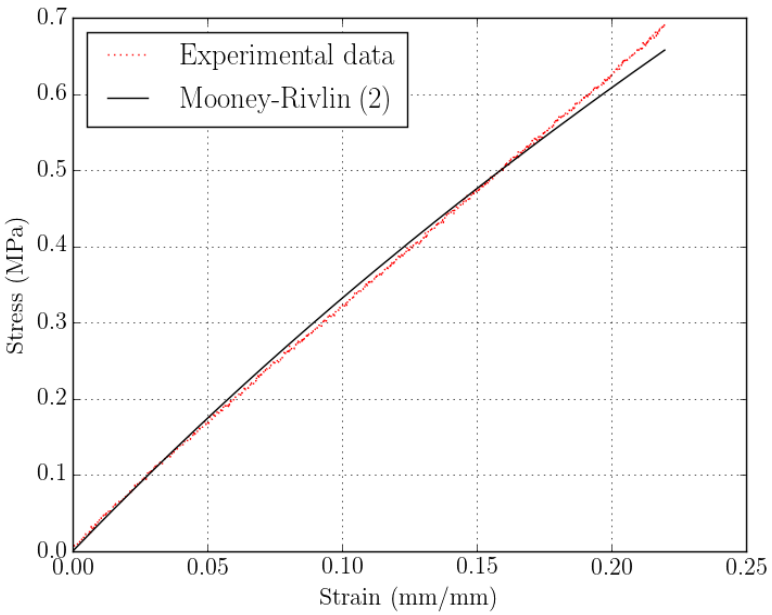

Figure 3.10: Inner liner rubber: the average tensile stress-strain test data and a two-term Mooney-Rivlin fit of the test data

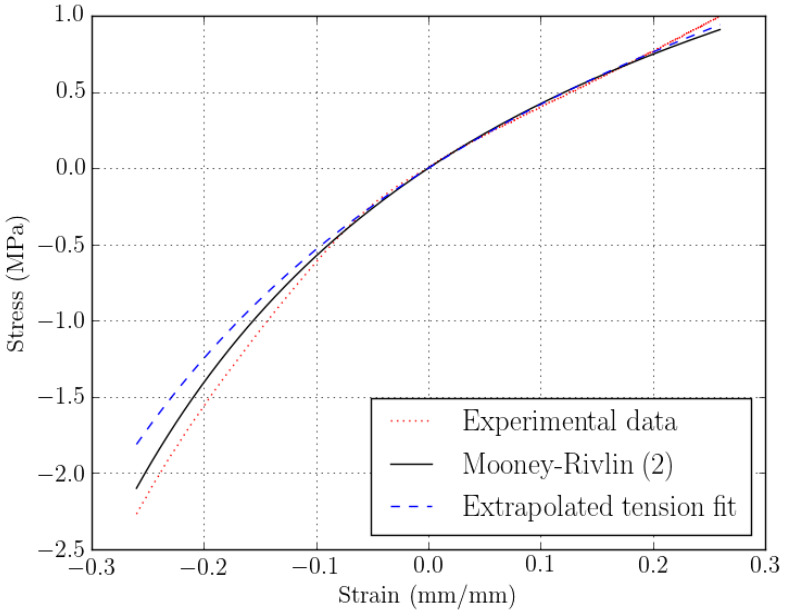

Figure 3.11: Sidewall rubber: the average tensile and compression stress-strain test data, a two-term Mooney-Rivlin fit of the test data and an extrapolated fit of the two-term Mooney-Rivlin material model using only the tensile test data

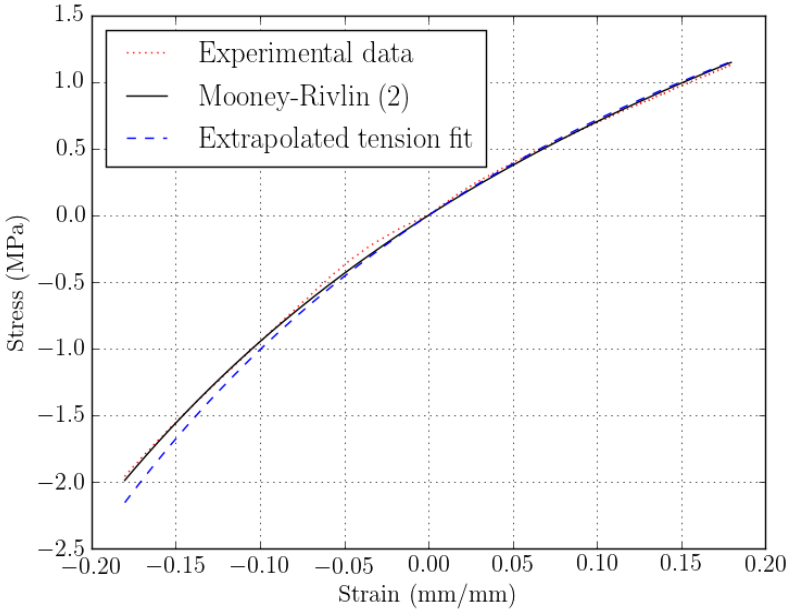

Figure 3.12: Tread rubber: the average tensile and compression stress-strain test data, a two-term Mooney-Rivlin fit of the test data and an extrapolated fit of the two-term Mooney-Rivlin material model using only the tensile test data

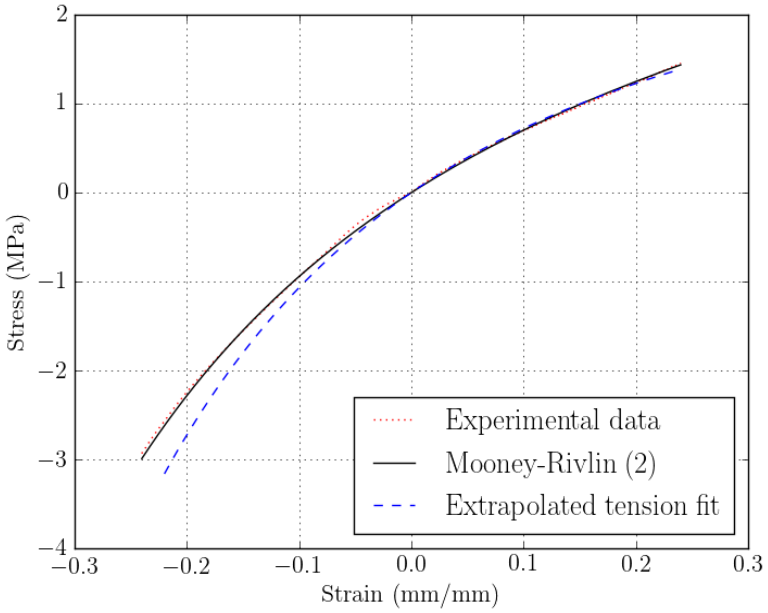

Figure 3.13: Rim strip rubber: the average tensile and compression stress-strain test data, a two-term Mooney-Rivlin fit of the test data and an extrapolated fit of the two-term Mooney-Rivlin material model using only the tensile test data

The two-term Mooney-Rivlin material coefficients calculated in Marc/Mentat for the rubber compounds are given in Table 3.4. The derivation of hyperelastic material models includes the assumption of incompressibility. Incompressibility implies a Poisson's ratio of 0.5, and therefore this value was assigned to each of the rubber compounds in Table 3.4. It should be noted that only positive coefficients were used to fit the data. Positive coefficients guarantee stability in all modes for all strain and were therefore preferred MSC (2010).

Table 3.4: C_{10}, C_{01} and Poisson's ratio of the inner liner, sidewall, tread and rim strip rubber compounds

	C_{10} (MPa)	C_{01} (MPa)	Poisson's ratio
Inner liner	0.5424	0.0706	0.5
Sidewall	0.3735	0.4387	0.5
Rim strip	0.7103	0.6295	0.5
Tread	0.6925	0.6516	0.5

3.4.3 Density

The density of the rubber compounds was established from volume and mass measurements of sidewall and tread samples cut from the tyre segment. The equipment, methodology and results are discussed in Appendix E. The average density established from the test results was 1 040.8 kg/m^3. This value was considered viable and was therefore used in the numerical model.

3.4.4 Hysteresis coefficient

The hysteresis coefficient of the inner liner, sidewall and tread rubber compounds was determined from dynamic mechanical analysis (DMA) done on samples of each compound. The equipment, test procedures and results are discussed in Appendix F. The average hysteresis coefficient established from DMA of the different rubber compounds are given in Table 3.5. These values were considered viable and were used to calculate the heat generation in the tyre as described in Section 2.3.

Table 3.5: Average hysteresis coefficient

	Hysteresis coefficient
Inner liner	0.2132
Sidewall	0.1557
Tread	0.1864

3.5 Conclusion

In conclusion, the tyre geometry and material properties given in this chapter were considered sufficient for numerical modelling of the earthmover tyre under investigation. A summary of the material properties used for the numerical model are given in Table 3.6.

Table 3.6: Material properties used for the numerical model

	Young's Modulus (GPa)	C_{10} (MPa)	C_{01} (MPa)	Poisson's ratio	Density (kg/m^3)
Belt 1 & 2	32.3	-	-	0.3	7870
Belt 3 & 4	148.6	-	-	0.3	7870
Belt 5	148.5	-	-	0.3	7870
Body Ply	148.6	-	-	0.3	7870
Bead	237.1	-	-	0.3	7870
Inner liner	-	0.5424	0.0706	0.5	1040
Sidewall	-	0.3735	0.4387	0.5	1040
Rim Strip	-	0.7103	0.6295	0.5	1040
Tread	-	0.6925	0.6516	0.5	1040

Chapter 4

Numerical modelling: Non-linear considerations and analysis procedure

This chapter describes the criteria and boundary conditions used to develop the models required for the uncoupled analysis procedure described in Section 2.4.2. In short, this analysis includes a structural dynamic rolling analysis and a steady-state thermal analysis to simulate the temperature distribution in the tyre cross-section. The selected criteria and the description of the models are based on the recommendations and features supported in Marc/Mentat. A brief description of the solving method and the criteria used to define each loadcase condition are included in this chapter as well.

4.1 Non-linear considerations

Besides the non-linear material behaviour of the rubber compounds in the tyre, the models developed in this analysis included geometric and contact non-linearities. This section describes the non-linear solving method and the non-linear boundary conditions included in this analysis. The numerical modelling of the non-linear material behaviour of the rubber compounds will not be repeated in this section since it was discussed in Chapter 3.

4.1.1 Non-linear solution criteria

An iterative `Full Newton-Raphson` solving method was used to solve the non-linear analysis. In a non-linear solution procedure, the results of the non-linear analysis is dependent on the convergence criteria defined in the model. An `Adaptive Multi-Criteria` loadcase stepping procedure was used to solve each loadcase in this analysis. This stepping procedure requires user specified criteria to solve the loadcase. This criteria included the specification of the convergence tolerance, initial and maximum fraction of loadcase time and the desired number of cycles per increment.

A relative residual tolerance was used to monitor the extent to which the iterative procedure has reached equilibrium state during convergence. This convergence criterion includes the specification of a convergence tolerance. The convergence tolerance is defined as the threshold value below which convergence is deemed to have occurred. If this tolerance is too slack, a false state of equilibrium will be given. If the tolerance is too tight, the simulation may include unnecessary iterations (MSC, 2013). Therefore, the convergence criteria of each loadcase depends on the extent non-linearity of the relevant boundary conditions.

The `Total Loadcase Time`, the `Initial Fraction of Loadcase Time`, the `Minimum Fraction of Loadcase Time` and the `Maximum fraction of loadcase time` were specified in an adaptive loadcase procedure as the load increment parameters. In this procedure, the `Total Loadcase Time` refers to the duration of the relevant loadcase. The `Initial Fraction of Loadcase Time` refers to the initial fraction of the total load applied that will be used to solve each increment during the relevant loadcase. The `Minimum Fraction of Loadcase Time` refers to the minimum fraction of the total load that may be applied to solve the desired increment of the relevant loadcase. The `Maximum Fraction of Loadcase Time` refers to the maximum fraction of the total load that may be applied to solve the desired increment of the relevant loadcase.

If the simulation has not reached convergence at the load fraction indicated by the `Minimum Fraction of Loadcase Time`, the analysis will stop. If the load fraction specified by the `Maximum Fraction of Loadcase Time` is too large, the time step associated with the specified load at that increment may be too large. Thus, the model may converge, but the increment may be too large and neglect some intermediate increments that was required to sufficiently capture the tyre behaviour. The effect of this parameter becomes increasingly relevant as the non-linearity of the simulation increases, such as a simulation which includes the rolling of a tyre. The value of the these parameters can only be established from observations of the model convergence during simulations.

The loadcase criteria include the `Desired # Recycles/Increment` and the `Maximum # Recycles`. The `Desired # Recycles/Increment` refers to the number of iterations the solving algorithm must use to reach convergence. If convergence is reached before the desired amount of iterations is reached, the time step of the next increment will increase. If the desired and the actual amount of increments required to reach convergence is the same, the time step will remain the same for the next increment. If the desired amount of increments are exceeded before convergence is reached, the time step of the next increment will be decreased. The `Maximum # Recycles` refers to the maximum number of recycles the algorithm is allowed before the increment can be restarted at a reduced load level (MSC, 2013).

4.1.2 Geometric non-linearity

Large deflections or strains typically occur in models including rubber components, due to its hyperelastic material behaviour. Models that undergo large deflection or strains are defined as geometrically non-linear. An `Updated Lagrange` framework

with a `Large Strain` structural analysis formulation was specified in Marc/Mentat to accommodate these large strains. This framework is formulated in terms of true stress and logarithmic strain. All the integrals are evaluated with respect to the last completed iteration of the current increment, mapping the elements to the current configuration and not to the undistorted mesh. The deformation of the elements is taken into account by means of the left Cauchy-Green deformation tensor (MSC, 2013).

4.1.3 Non-linear contact

Tangential stresses exist between the tyre and road surface during rolling, due to friction. If these stresses reach critical values, the bodies will slip and move relative to each other. As long as these stresses remain below this critical value, the bodies will stick. The relation between the critical frictional stress, τ_{cr} (Pa), and contact pressure, P (Pa), is given as,

$$\tau_{cr} = \mu P \tag{4.1}$$

where μ is the friction coefficient. This friction model is known as Coulomb friction. This frictional stress is defined as a step function. This step function is given in terms of a tangential relative incremental displacement, δu_t, for a given normal stress, σ_t (MSC, 2014*b*). The discontinuity in this step function can be approximated by a `Coulomb Bilinear` friction model in Marc/Mentat for a displacement control contact condition. This model ensures that the tangential stresses remain within the friction force tolerance during the analysis. A friction force tolerance of 0.05 and an automatic slip threshold were automatically specified in Marc/Mentat. The `Bilinear Coulomb` model is shown in Figure 4.1.

A `Node To Segment` method was used to specify the boundaries of the contact bodies. This method uses an automated solution procedure which is based on an algorithm that automatically detects the nodes entering contact and generates the appropriate constraints to ensure that no penetration occurs.

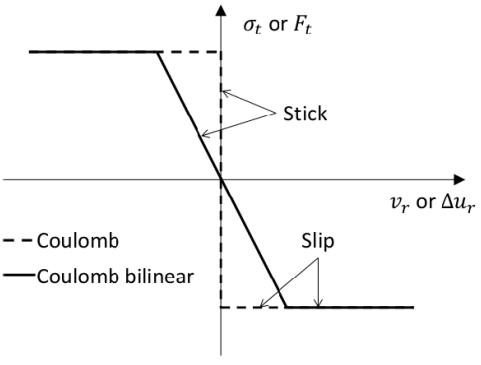

Figure 4.1: `Coulomb` and `Coulomb Bilinear` friction models (MSC, 2014*b*)

4.2 Numerical analysis procedure

This section describes the models developed for the dynamic rolling analysis and the thermal analysis. The rolling analysis was executed as three separate analyses. Initially, a 2-D axisymmetric model of the tyre cross-section was developed and inflated. The 2-D model was then expanded into segments revolving around the x-axis as indicated on Figure 4.2 to create a 3-D model of the tyre. The inflation results were also used as an initial condition for the 3-D model. The 3-D tyre was loaded and rolled to obtain its elastic strain energy density for one revolution. The elastic strain energy density was used to calculate the heat generation rate in the tyre according to the method described in Section 2.3.3. The heat generation rate of each element was implemented into the 2-D axisymmetric model of the tyre and a thermal/structural analysis was completed to simulate the temperature distribution in the tyre.

The models developed for the dynamic rolling analysis were modelled as implicit non-linear structural finite element models, while models developed for the steady-state thermal analysis were modelled as implicit non-linear thermal/structural finite element models. The material properties obtained in Chapter 3 were used for the numerical modelling of the tyre components. The 2-D axisymmetric model of the tyre and its structural components and rubber compounds are shown in Figure 4.2.

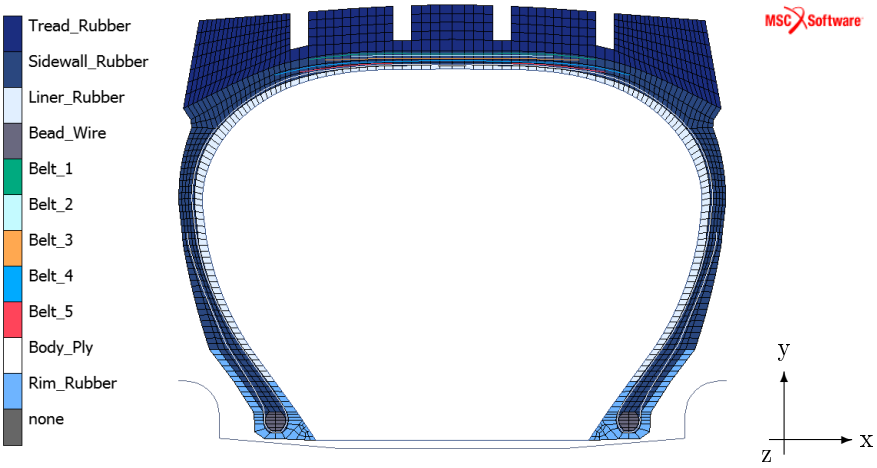

Figure 4.2: 2-D axisymmetric tyre model, including the location of the structural components and the regions modelled for the inner liner, sidewall, rim strip and tread rubber compounds

4.2.1 Inflation analysis

The first step in the rolling analysis procedure was the inflation of the 2-D axisymmetric tyre model. The rubber components and the bead were meshed using `Full & Herrmann Formulation` linear quadrilateral elements, while the body ply and steel belts were meshed by two node `Membrane Rebar` elements. The 2-D axisymmetric model consisted of 1 845 elements and 2 065 nodes.

The model was inflated by applying a `Cavity Pressure Load` to a `Cavity` function specified in the model. The pressure load and cavity are shown in Figure 4.3. A `Cavity Surface Element` was placed between the inside end points of the tyre to close the cavity. The `Cavity Pressure Load` was increased as a linear function of time to inflate the tyre. As the pressure increases the volume of the cavity will increase until the specified pressure is reached. After the tyre is inflated, the mass of gas inside the cavity will remain constant.

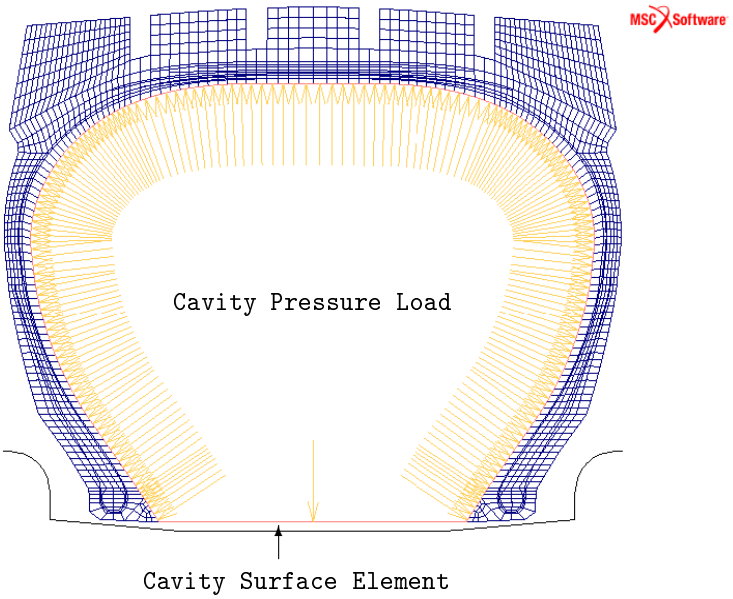

Figure 4.3: Boundary conditions for the inflation analysis

The `Cavity` function must be specified with a reference pressure, temperature and density of the gas used to inflate the tyre at the reference pressure and temperature conditions. These parameters are used to calculate the specific gas constant and the mass of the gas. The `Cavity` function was specified with a reference pressure of 100 kPa and temperature of 298.15 K. In industry, earthmover tyres are preferably inflated with nitrogen and not air. Nitrogen is preferred over air since it can absorb more heat than air at a constant pressure. Thus, if an earthmover tyre would be subjected to similar conditions, the internal temperature of gas in the tyre will be less for a tyre inflated with nitrogen than a tyre inflated with air. This property therefore delays the increase in the internal tyre temperature and pressure, which can lead to the explosion of these tyres and therefore increases the life cycle of the tyre, compared to a the same tyre inflated with air. In order to simulate the tyre model at similar conditions as in industry, the `Cavity` function was specified with the density of nitrogen at the corresponding pressure and temperature, which is 1.13006 kg/m^3. The cavity job parameters are given in Table 4.1.

The meshed tyre and the geometric rim profile were selected as contact bodies. The deformable tyre contact body was specified as a `3-D` C^0`-Continuity Analytical`

`Boundary` and the rigid rim as an `Analytical Boundary`. A deformable-to-rigid (Meshed-to-Geometric) touching contact table was specified for the contact interaction. A touching contact was used, since the tyre must be inflated before it makes contact with the rim profile. No friction was modelled between the tyre and rim, since the rim was only used as a geometrical boundary to inflate the tyre and keep it in position.

The parameters used for the inflation loadcase are summarised in Table 4.2. A relative residual force tolerance of 0.1 was used for the inflation loadcase. This convergence tolerance was considered sufficient for the purpose of this study, since the inflation loadcase is only slightly non-linear. Similar results were obtained if the convergence tolerance was tightened to 0.001, confirming the convergence of the numerical results.

The results of the inflated 2-D axisymmetric model were used as an initial condition in the loading and rolling analysis. The model output results included: the deformation gradient, the determinant of the deformation gradient, the elastic left Cauchy-Green deformation, the equivalent Cauchy stress and the total strain.

Table 4.1: Modelling parameters for the `Cavity`

Solution procedure	Iterative
Polytropic process exponent	1
Ambient pressure (Pa)	101 325

Table 4.2: Stepping parameters for the inflation loadcase

Loadcase time (s)	2
Initial fraction of loadcase time	0.1
Minimum fraction of loadcase time	10^{-10}
Maximum fraction of loadcase time	0.5
Desired number of recycles per increment	10
Time step increase factor	1.2
Maximum number of recycles	20

4.2.2 Loading analysis

The second step in the rolling analysis procedure was the loading analysis of the 3-D expanded tyre. A 3-D model was created by expanding the 2-D axisymmetric model using the `Axisymmetric Model To 3-D` feature in Marc/Mentat. The model was expanded into different repetition angles. This expansion was based on similar studies completed by Maritz (2015), Ghoreishy (2006) and Ghoreishy *et al.* (2007). In order to ensure an accurate evaluation of the contact area at the road tyre contact, the selected expansion angles were specified to have a very fine mesh in the vicinity

of this interface. The angle increases away from the contact area to decrease the number of elements in the model. The angles are shown in Table 4.3.

The rubber components and the bead were meshed with `Full & Herrmann Formulation` linear hexagon elements. The body ply and steel belts were meshed with quadrilateral `Membrane Rebar` elements. The 3-D model consisted of 88 560 elements and 99 121 nodes. The 3-D model and road surface are shown in Figure 4.4.

Table 4.3: Repetition angle and number of repetitions for the 3-D model

Repetition angle	Number of repetitions
2.5°	9
5°	2
7.5°	5
10°	2
15°	12
10°	2
7.50°	5
5°	2
2.5°	9

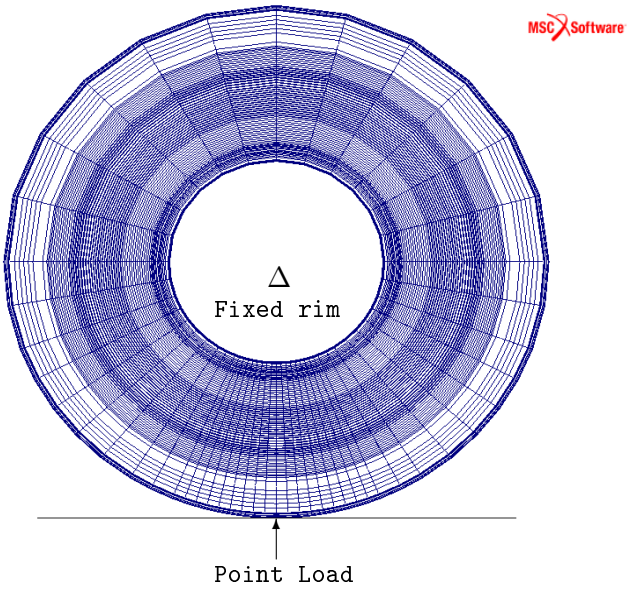

Figure 4.4: Repetition angles and boundary conditions for the loading analysis

The meshed tyre and the geometric road surface were selected as contact bodies. The deformable tyre contact body was specified as a `3-D C0-Continuity Analytical Boundary` and the rigid road surface as an `Analytical Boundary`. A deformable-to-rigid (Meshed-to-Geometric) touching contact table was specified for the meshed

tyre and the geometric road surface contact interaction. A friction coefficient of 0.7 was used to model the friction between the tyre and road. This coefficient is typically used for gravel road contact (Chi and Caldas, 2009).

The model was inflated before the load was applied. The results of the inflated 2-D axisymmetric model were used to provide the initial conditions for the 3-D model. To ensure that the inflation pressure was correct after the expansion, a `Cavity Pressure Load` was applied to the cavity for a short period. This load condition enabled any pressure change that could have occurred during the 2-D to 3-D model expansion to be corrected. Thereafter, the `Cavity Pressure Load` was changed to a `Cavity Mass Load`. A `Cavity Mass Load` was used to close the cavity and ensure that the mass of the gas inside remains constant during loading. After the tyre was inflated to the correct pressure the tyre was loaded.

It should be noted that when a load is applied to the tyre, the volume of the tyre will change, and consequently the pressure will increase. As a result, the temperature will rise as well. This increase in temperature was ignored, since it cannot be modelled in Marc/Mentat and was considered negligible compared to the total volume of the tyre and heat generated in the tyre due to hysteresis.

The load was applied using the `Load Control Rigid Body` option. This option allowed a `Point Load` to be applied to a control node on the road surface that transferred the load to the rigid road surface. The load was applied linearly as a function of time. As the road surface came in contact with the tyre, the tyre deformed. The boundary conditions used for the loading analysis are shown in Figure 4.4.

The loading analysis was divided into an inflation loadcase and a loading loadcase. The parameters used for the inflation loadcase were the same as for the inflation analysis given in Table 4.2, except that the loadcase time was reduced from 2 s to 0.5 s. The parameters defined for the loading loadcase are shown in Table 4.4. A relative residual force convergence tolerance of 0.05 was used for the loading loadcase. The loading loadcase is slightly more non-linear than the inflation analysis and therefore the tolerance was tightened. In order to verify the convergence of the numerical results, a simulation was completed at a convergence tolerance of 0.001. The results were consistent and the convergence of the numerical results were confirmed.

Table 4.4: Stepping parameters for the loading loadcase

Loadcase time (s)	1.5
Initial fraction of loadcase time	0.02
Minimum fraction of loadcase time	10^{-10}
Maximum fraction of loadcase time	0.5
Desired number of recycles per increment	12
Time step increase factor	1.2
Maximum number of recycles	25

The vertical tyre displacement obtained from the loading analysis was used to load the tyre in the rolling analysis using a displacement control condition. This method was used instead of a load control condition, since a load control condition is more computationally expensive than a displacement control condition. The deformation, total strain and contact normal stress results were also obtained from the loading analysis.

4.2.3 Rolling analysis

The last step in the dynamic rolling analysis was the rolling of the tyre. The 3-D tyre model used in the loading analysis, was used for the rolling analysis as well. However, for the rolling analysis, the tyre was rotated 180° around the axial axis. The road surface was extended to a length of 14 m. The rolling model and road surface are shown in Figure 4.5.

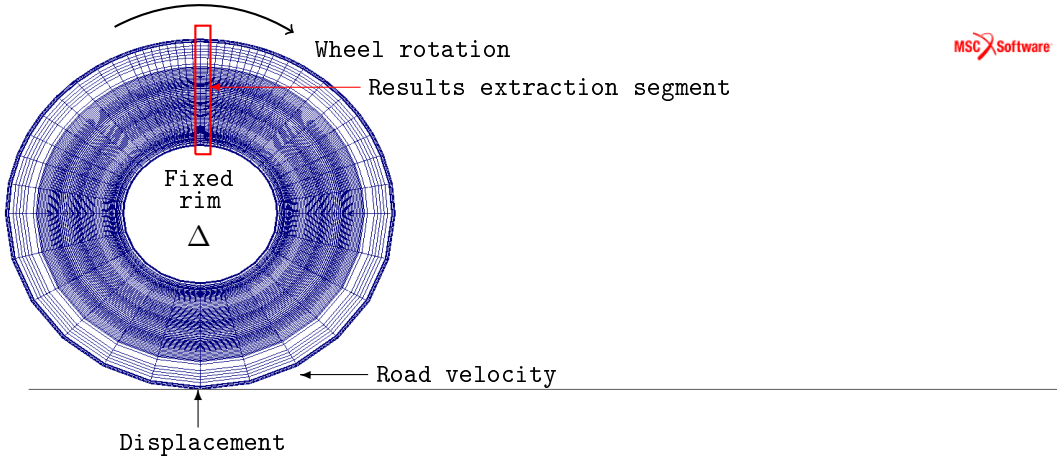

Figure 4.5: Boundary conditions for the rolling analysis

The following parameters of the rolling analysis were the same as for the loading analysis:

- Contact model and body definitions.
- Contact body boundary descriptions and interactions.
- Friction model and coefficients.
- Initial conditions and `Cavity Pressure Load`.
- Switch to a `Cavity Mass Load`.
- `Large Strain` formulation.
- `Adaptive Multi-Criteria` stepping procedure.
- Convergence criteria for the inflation and loading loadcase.

The load in the rolling analysis was enforced as a displacement control condition, using the `Velocity Control Rigid Body` option in Marc/Mentat. The duration and displacement of the road surface was specified to be consistent with the displacement obtained from the loading analysis. The velocity road surface was also specified with the `Velocity Control Rigid Body` option to enforce the rotation of the tyre. In reality the tyre is fixed to the rim and the rim enforces the rolling of the tyre. In this analysis, however, the rotation of the tyre was enforce by the relative velocity of the road surface during the tyre and road contact interaction. The road velocity was specified as 15 km/h until at least two revolutions were completed. The boundary conditions of the rolling analysis are included in Figure 4.5.

The parameters used for the displacement loadcase were the same as in Table 4.4, except for the loadcase time, which was reduced from 1.5 s to 0.5 s. The parameters for the rolling loadcase are summarised in Table 4.5.

Table 4.5: Stepping parameters for the rolling loadcase

Loadcase time (s)	2.36
Initial fraction of loadcase time	0.02
Minimum fraction of loadcase time	10^{-16}
Maximum fraction of loadcase time	0.05
Desired number of recycles/increment	12
Time step increase factor	1.2
Maximum number of recycles	24

A relative residual force convergence tolerance of 0.07 was used for the rolling loadcase. This tolerance was selected based on a combination of factors. These factors included observations made from the time steps used to converge and the corresponding computational resources required when the tyre model was subjected to different tolerances and load conditions. It should be noted that total computational time required for the tyre to complete two revolutions on the HPC at Stellenbosch University ranged from three to four weeks, depending on the operating conditions the model was subjected to during the simulation.

In general a rolling analysis is considered as highly non-linear and it is known that a tolerance of 0.001 ensures convergence for this type of analysis. However, a convergence tolerance of 0.001 would have been even more computationally expensive. According to MSC (2014*a*), a relative force tolerance of 0.05 is sufficient for a steady-state rolling analysis of an automobile tyre.

In order to evaluate the extent of the convergence of the models, some of the models were simulated at a convergence tolerance of 0.007 and its results were compared to the results obtained from the models using a tolerance of 0.07. The influence of the rolling results on the maximum temperature results obtained from the thermal analysis using different tolerances deviated with no more than 1.4 %, ensuring the convergence of the results obtained from the rolling analysis. Thus, it was concluded

that the results obtained from the numerical models simulated at a relative force tolerance of 0.07 were considered sufficient to represent the temperature distribution in the tyre model. It should be noted that a convergence tolerance between 0.001 to 0.007 is still preferable if it is feasible, considering the trade-off in simulation time and computational requirements.

The tyre was rolled for one revolution before the results extraction commenced at the start of the next revolution. The elastic strain energy density in the elements was extracted for one revolution and was used to calculate the heat generation rate in the elements. The segment used to extract the results are also shown in Figure 4.5. The deformation, equivalent Cauchy stress, total strain and contact normal stress results were also obtained during the rolling analysis.

The heat generated due to friction between the tyre and the road surface was ignored in this analysis. This simplification was based on the assumption that heat generation due to friction between the tyre and the road will be negligible compared to that caused by hysteresis effects (Smith *et al.*, 2012).

4.2.4 Steady-state thermal analysis

In this analysis the heat transfer boundary conditions were applied to the 2-D axisymmetric tyre model to evaluate the temperature distribution in the tyre cross-section. The heat transfer in this analysis includes the heat generated in the tyre cross-section, the conduction of the generated heat and the convection of the heat leaving the tyre. The effects of heat transfer by radiation were ignored, since previous studies have shown its effects negligible (Nyaaba *et al.*, 2015). The 2-D axisymmetric tyre model used for the thermal analysis is shown in Figure 4.6.

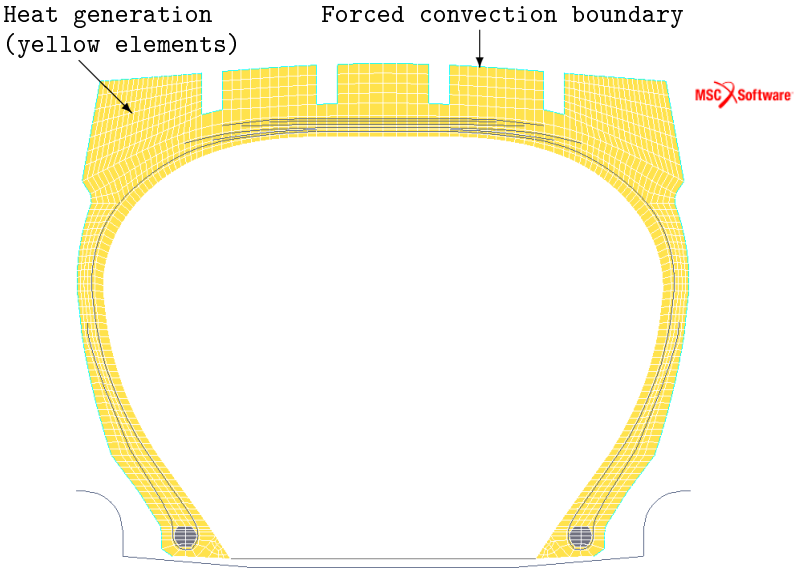

Figure 4.6: 2-D axisymmetric tyre model used for the thermal analysis and the heat transfer boundary conditions

An ambient temperature of 25 °C was defined for this analysis and a uniform initial temperature condition of 25 °C was applied to all of the nodes. The heat generation in the elements was defined as a thermal `Volume Flux` boundary condition. The flux was calculated from the elastic strain energy density obtained for the rolling analysis according to the method described in Section 2.3.3. The heat generated in the tyre was conducted to the exposed tyre surfaces. In order to simulate the conduction heat transfer in the tyre, the thermal conductivity, specific heat and emissivity of the tyre materials were included in this analysis. These properties were obtained from the material properties of the rubber compounds typically used in tyres, as provided by Gent (2012) and Clark (1981). The thermal properties are given in Table 4.6.

Table 4.6: Thermal properties of the materials used in the thermal analysis

	Thermal conductivity (W/m °C)	Specific heat (J/kg °C)	Emissivity
Belts, body ply and bead	49.80	448	0.00
Inner liner, sidewall, rim strip and tread rubber	0.25	1 900	0.94

The convection heat transfer boundary condition was added to the outside edges of the tyre as an `Edge Film`. A constant convective film coefficient as given by Equation 4.2, were defined for all exposed surfaces in the model. This forced convection coefficient has been established from experimental tests done on the outside surface of a passenger vehicle tyre by Assaad *et al.* (2008), but can be used for earthmover tyres as well (Nyaaba *et al.*, 2015). From Equation 4.2 it can be seen that the film coefficient will depend on the rolling velocity of the tyre. The temperature distribution in the tyre was simulated at 15, 30 and 45 km/h. The parameters defined for the convection heat transfer boundary condition are given in Table 4.7. The boundary conditions defined for the thermal analysis are included in Figure 4.6.

$$h_o = 5.9 + 3.7\ V_c \tag{4.2}$$

where h_o is the convection coefficient (W/m^2) on the outside of the tyre and V_c is the rolling velocity of the tyre (m/s). Natural convection occurs on the inside of the tyre, but it was not included in the thermal analysis. This heat transfer condition can be used to obtain the internal tyre temperature, but it can not be modelled, since the internal tyre temperature is dependent on the heat generation in the tyre.

The thermal analysis was divided into an inflation loadcase and a heating loadcase. The parameters used for the inflation loadcase were the same as for the inflation analysis, as seen in Table 4.2, except that the loadcase time was reduced from 2 s to 1 s. The parameters used for the thermal loadcase are given in Table 4.8. A relative residual force convergence tolerance of 0.1 was used for each loadcase. The thermal convergence was achieved using a `max error` in the temperature estimate of `zero`.

The convergence tolerance used in these loadcases were considered sufficient for the purpose of this analysis.

The temperature distribution and the heat flux distribution in the tyre cross-section were obtained in this analysis. These results were used to identify the maximum temperature in the tyre cross-section. The results will be discussed in Chapter 5.

Table 4.7: Forced convection heat transfer parameters

Ambient temperature settings method	Single sink point
Ambient temperature (°C)	25
Evaluation temperature	Ambient
Film coefficient (W/m^2 °C) at 15 km/h	21.32
30 km/h	36.73
45 km/h	52.15

Table 4.8: Stepping parameters for the thermal loadcase

Loadcase time (s)	360 000
Initial fraction of loadcase time	0.01
Minimum fraction of loadcase time	10^{-5}
Maximum fraction of loadcase time	0.5
Desired number of recycles/increment	5
Time step increase factor	1.2
Maximum number of recycles	10

4.3 Conclusion

This chapter provided a description of the numerical models developed for an uncoupled analysis procedure to simulate the temperature distribution in the tyre cross-section. The boundary condition and convergence criteria defined in this chapter was verified to ensure the convergence of the numerical models. Thus, it can be concluded that the results of the proposed numerical models can be used to evaluate its accuracy. The accuracy of the proposed models will be evaluated by comparing the numerical results to experimental data provided by the tyre manufacturer.

Chapter 5

Numerical results: Discussion and evaluation

The results of the numerical models described in Chapter 4 are provided in this chapter. These results are compared to experimental data to evaluate the accuracy of the proposed numerical models. The numerical models were subjected to different combinations of operating conditions to study its influence on the tyre behaviour and the maximum temperature in the tyre during each combination of conditions. The method used to select the relevant parameters of the operating conditions are included in this chapter as well.

5.1 Operating conditions

The numerical tyre models were subjected to different inflation pressures, loads and rolling velocities to evaluate its influence on the temperature distribution in the tyre. These conditions were selected to be consistent with a tyre and articulated dump truck wheel assembly typically used in the mining industry. A summary of the recommended inflation pressures, loads and vehicle velocity specifications is included in Appendix A.

In order to study the tyre behaviour, the operating conditions were selected to simulate the tyre behaviour during under-inflation, over-inflation and when the tyre is inflated to its recommended pressure. Furthermore, each combination of inflation pressures and applied loads were subjected to different velocities. These velocities ranged from 15 km/h, which is a safe operating velocity, 28 km/h which is the recommended travelling distance per hour and 50 km/h which is the maximum rated tyre velocity at the specified load and pressure conditions indicated on the tyre's sidewall markings. The selected inflation pressures, loads and velocities are given in Table 5.1. A separate model was created for each combination specified in Table 5.1. A total of 27 models were completed for the thermal analysis.

It should be noted that the road velocity specified in the rolling analysis is irrelevant to the velocities used to calculate the heat generation rate in the tyre from the elastic strain energy density results. This assumption is based on the theory that the

elastic strain energy density results is a function of the material's deformation during the analysis and it is therefore independent of the velocity specified in the analysis. The velocity of the tyre is only taken into account when the heat generation rate in the elements are theoretically calculated from Equation 2.15 at the desired rolling frequency.

Table 5.1: Operating conditions used for the numerical analysis

Tyre pressure (kPa)	Load (N)	Road velocity (km/h)
200	22 588	15, 30, 45
	48 656	15, 30, 45
	74 703	15, 30, 45
268	22 588	15, 30, 45
	48 656	15, 30, 45
	74 703	15, 30, 45
336	22 588	15, 30, 45
	48 656	15, 30, 45
	74 703	15, 30, 45

5.2 Numerical results

The numerical results of the inflation, loading, rolling and heat transfer loadcases are discussed in this section. These results include the numerical tyre geometry, the vertical tyre deflection and contact area during loading, the elastic strain energy density and the temperature distribution in the tyre cross-section. The numerical results are compared to experimental data provided by the tyre manufacturer to evaluate the accuracy of the proposed numerical models.

Initially, the numerical models were supposed to be validated from experimental tests done on a tyre and Bell B25E articulated dump truck assembly at one of Anglo's mines. Unfortunately, by the time the tests could be executed, Anglo upgraded to larger trucks and it was not feasible to test the tyre's response in this set-up any more. Alternatively, experimental data provided by the manufacturer was used to evaluate the numerical tyre deflection and contact area. The data obtained from the manufacturer did not include the exact same operating conditions as the conditions considered in this project. In order to extend the evaluation of the numerical results, a numerical analysis of the tyre inflated to its rated inflation pressure of 450 kPa and its maximum rated load of 90 742 N, were completed for the inflation and the loading analysis. The corresponding experimental results were included in the provided data sets and therefore the numerical results at this load condition were included in the inflation and the loading analysis results.

From Chapter 2 it is evident that the elastic strain energy density is based on the tyre deformation during the rolling analysis. Since it was not feasible to experimentally measure the elastic strain energy density or temperature distribution in the tyre to validate the numerical results, the accuracy of the tyre deflection and contact patch is essential to provide a sufficient prediction of the tyre behaviour. Thus, the accuracy of the elastic strain energy density and ultimately the temperature distribution in the thermal models were based on the accuracy of the numerical results obtained from structural static analysis.

5.2.1 Tyre geometry

The finite element model of the 2-D tyre cross-section established from the measurement of the actual tyre, as discussed in Section 3.1, was compared to the specifications of a new tyre to verify the resulting tyre profile used for the numerical analysis. The definition of the dimensions used to measure the tyre parameters are shown in Figure 5.1. The measured numerical dimensions were compared to the dimensions specified by the tyre manufacturer. These results are given in Table 5.2.

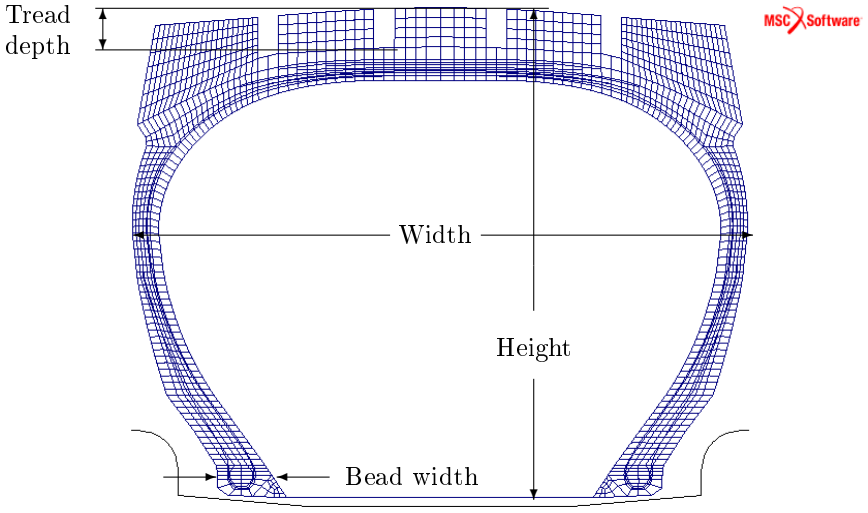

Figure 5.1: Definition of the tyre parameters measured from the 2-D finite element model of the tyre geometry

From the results obtained it was concluded that the measured tyre geometry of the 2-D finite element model of the tyre model sufficiently represents that of a new tyre and therefore it was used for the numerical analysis.

5.2.2 Inflation analysis

The inflated tyre profile was used as an initial condition to inflate the 3-D tyre model. The inflated tyre model was evaluated according to the specified tyre dimensions provided by the manufacturers to ensure consistency between the inflated tyre models

Table 5.2: Recommenced and numerical tyre measurements

	Specified	Measured	% Difference
Height (m)	0.478	0.474	0.8
Width (m)	0.585	0.582	0.5
Radius (m)	0.795	0.794	0.1
Bead width (m)	0.057	0.058	1.8
Tread depth (m)	0.038	0.038	0.0

and the actual tyre. The tyre model was inflated to the recommended tyre pressure of 450 kPa. The resulting numerical and actual tyre measurements are included in Table 5.3. Figure 5.2 illustrates a cross-sectional view of the original and deformed 3-D tyre profile before and after inflation.

From the results obtained it was concluded that the numerical tyre inflation sufficiently represents the inflation of the actual tyre and therefore it was used as an initial condition to inflate the 3-D tyre model. The inflated tyre model was used as a reference point to measure the numerical tyre deflection.

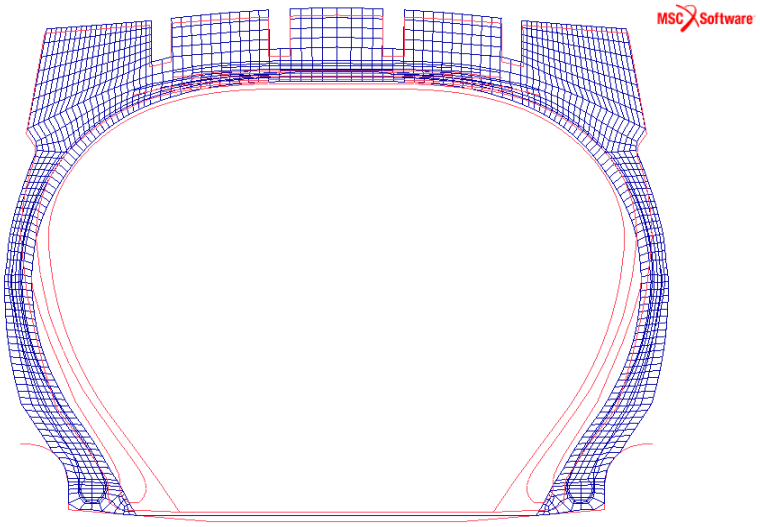

Figure 5.2: Cross-sectional view of the 3-D tyre profile before and after an inflation pressure of 450 kPa was applied to it

Table 5.3: Tyre geometry specifications 3-D tyre model inflated to 450 kPa

	Specified	Numerical	% Difference
Height (m)	0.489	0.485	0.8
Width (m)	0.601	0.603	0.3
Radius (m)	0.806	0.808	0.2

5.2.3 Loading analysis

The numerical tyre displacement and the contact area results are discussed in this section. The accuracy of the tyre deflection and the contact area results are evaluated by comparing the numerical results to the experimental data provided by the tyre manufacturer. The measured tyre deflection and contact area results are defined according to the parameters shown in Figure 5.3 and 5.4.

The experimental and the numerical tyre deflection, the overall width, the contact width and the contact length are included in Tables 5.4 to 5.7, respectively. In order to evaluate the accuracy of the numerical results, a percentage difference of the values are given in these tables as well. It should be noted that the percentage difference of the tyre deflection was based on the difference in the loaded tyre radius using the experimental and the numerical deflections stated in Table 5.4.

From the results obtained it can be seen that the numerical and experimental tyre deflection increases as the inflation pressure decreases or the load increases. The numerical tyre deflection deviates with no more than a maximum percentage difference of 3.9 % from the experimental results.

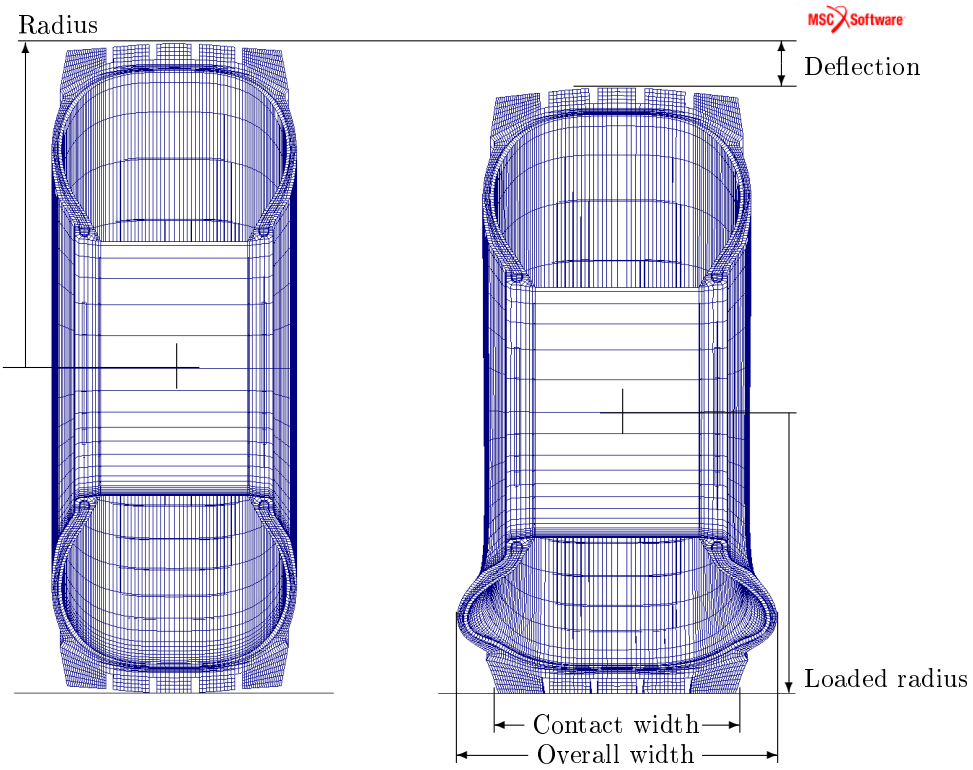

Figure 5.3: Parameter definition for the measured: (a) radius of the unloaded 3-D tyre model and (b) the loaded radius, deflection, contact width and overall width of the loaded 3-D tyre model

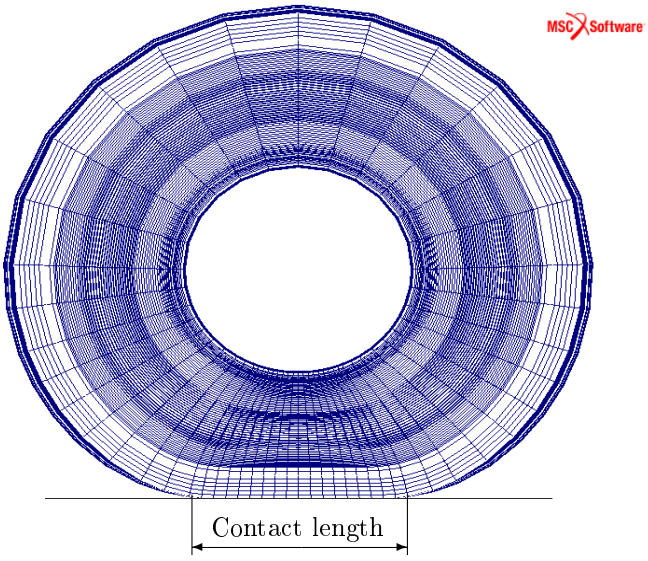

Figure 5.4: Parameter definition for the measured contact length of the 3-D tyre model

The overall tyre width increases as the tyre deflection increases. The numerical overall tyre width deviate with no more than a maximum percentage difference of approximately 2.5 % from the experimental results.

From the experimental results stated in Table 5.6, it is evident that the tread contact distribution has very little variation in the tyre width. Thus, the experimental contact width is essentially constant throughout the entire tyre tread width. However, it can still be concluded that the contact width increases as the inflation decreases or the load increases. This result is expected, since tyres are designed to wear evenly, which implies even tread contact over the entire tread width. With regard to the numerical results it can be seen that the tread contact width does not vary, but makes contact over the entire tread width for each operating condition. Since even tread contact is preferable, this result is sufficient for the purpose of this analysis. The numerical contact width results deviate with no more than a maximum percentage difference of 3.4 % from the experimental results.

The tread contact length, on the other hand, significantly increases as the tyre deflection increases. This behaviour is expected, since the contact width basically remains constant as the tyre deflection increases, and therefore it is expected that the contact length will increase as the tyre deflection increases. The numerical contact length deviated with no more than a maximum percentage difference of 9.7 % from the experimental results. An illustration of the 3-D numerical tyre deflection and contact area at no-load and when the tyre is loaded to 90 742 N are shown in Figure 5.5.

From the results obtained it can be concluded that the numerical tyre results are consistent with the experimental data within a maximum percentage difference of 3.9 %, 2.5 % , 3.4 % and 9.7 % for the vertical tyre deflection, the overall tyre width,

the tyre's contact width and the tyre's contact length, respectively. This percentage difference was considered sufficiently accurate to numerically represent the deformation of the actual tyre.

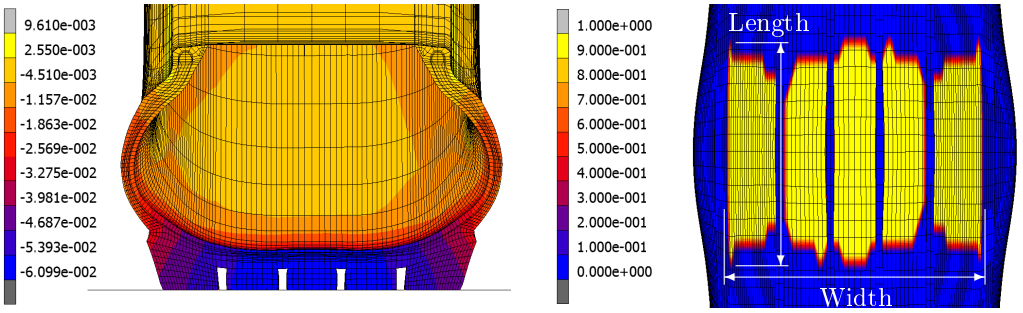

(a) (b)

Figure 5.5: Cross-sectional view of the 3-D tyre model inflated to 450 kPa and loaded to 90 742 N: (a) the tyre deflection and (b) its contact status

Table 5.4: Specified and numerical tyre radius and deflection

Tyre pressure	Force	Radius	Deflection		
(kPa)	(N)	(m)	Specified (m)	Numerical (m)	% Difference
200	22 588	0.800	0.042	0.039	0.4
	48 656		0.086	0.070	2.3
	74 703		0.127	0.100	3.9
268	22 588	0.803	-	0.035	-
	48 656		-	0.061	-
	74 703		-	0.085	-
336	22 588	0.805	-	0.032	-
	48 656		-	0.055	-
	74 703		-	0.075	-
450	48 656	0.808	0.050	0.048	0.5
	74 703		0.073	0.065	1.3
	90 742		0.087	0.075	1.9

Table 5.5: Specified and numerical overall tyre width

Tyre pressure	Force	Overall width		
(kPa)	(N)	Specified (m)	Numerical (m)	% Difference
200	22 588	0.640	0.645	0.8
	48 656	0.670	0.686	2.3
	74 703	0.699	0.717	2.5
268	22 588	0.636	0.636	0.1
	48 656	0.661	0.670	1.3
	74 703	0.685	0.699	2.0
336	22 588	0.633	0.629	0.7
	48 656	0.655	0.657	0.3
	74 703	0.676	0.685	1.4
450	48 656	0.649	0.645	0.6
	74 703	0.666	0.667	0.2
	90 742	0.676	0.678	0.3

Table 5.6: Specified and numerical contact width

Tyre pressure	Force	Contact width		
(kPa)	(N)	Specified (m)	Numerical (m)	% Difference
200	22 588	0.515	0.535	2.8
	48 656	0.527	0.535	0.5
	74 703	0.540	0.535	1.8
268	22 588	0.513	0.535	3.1
	48 656	0.524	0.535	1.2
	74 703	0.534	0.535	0.2
336	22 588	0.512	0.535	3.4
	48 656	0.521	0.535	2.5
	74 703	0.530	0.535	1.0
450	48 656	0.519	0.535	3.0
	74 703	0.526	0.535	1.8
	90 742	0.530	0.535	1.1

Table 5.7: Specified and numerical contact length

Tyre pressure	Force	Contact length (m)		
(kPa)	(N)	Specified (m)	Numerical (m)	% Difference
200	22 588	0.310	0.322	3.8
	48 656	0.433	0.402	7.2
	74 703	0.548	0.540	1.5
268	22 588	0.294	0.273	7.2
	48 656	0.397	0.397	0.1
	74 703	0.493	0.541	9.7
336	22 588	0.283	0.266	5.8
	48 656	0.374	0.391	4.5
	74 703	0.455	0.456	0.1
450	48 656	0.348	0.326	6.3
	74 703	0.416	0.392	5.7
	90 742	0.455	0.459	0.8

With regard to the deformation of the tyre, it should be noted that most of the tyre's deformation occurs in its sidewall due to the radial construction of the tyre. This construction ensures that the tread makes contact across the entire tread width, to ensure even wear during loading. The overall tyre width, the contact width and length is a function of the tyre deflection and each of these parameters will increase as the tyre deflection increases. The tyre deflection will increase as the inflation pressure decreases or the load increases.

The tyre and road contact stress distribution results were obtained from this analysis as well. These results could unfortunately not be experimentally validated, but it is included in Appendix G to be used as an estimate of the expected tyre contact stress that can be used as a comparison in future work.

5.2.4 Rolling analysis

The elastic strain energy density was extracted from the tyre segment shown in Figure 4.5 in the previous chapter for the second revolution of the rolling loadcase. Figure 5.6 illustrates a cross-sectional view of the elastic strain energy density of a 3-D tyre model. From this illustration, it can be seen that the elastic strain energy density is the highest at the sidewall regions. This result is expected since most of the tyre deformation typically occurs in this region to ensure even tread contact.

The heat generation rate was calculated from the elastic strain energy density results according to the method described in Section 2.3.3. In Chapter 2 it was assumed that the tyre model has to be rolled for only two revolutions, and not until steady-state to compute the heat generation in the tyre. This assumption was based on the behaviour of hyperelastic material models.

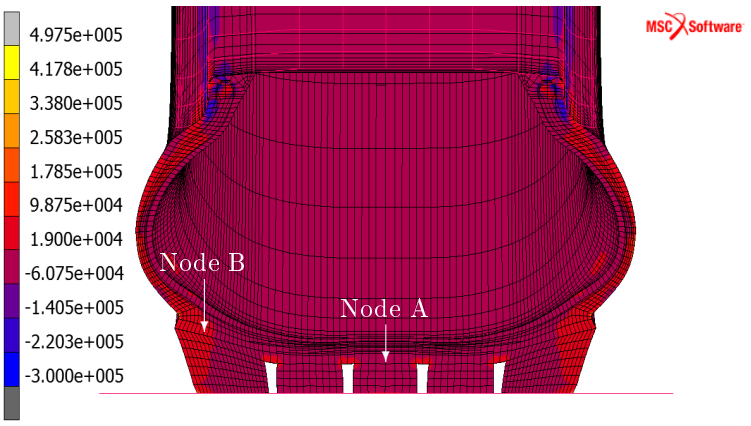

Figure 5.6: Cross-sectional view of the elastic strain energy density for the 3-D tyre model inflated to 268 kPa and loaded to 74 703 N during the second tyre revolution

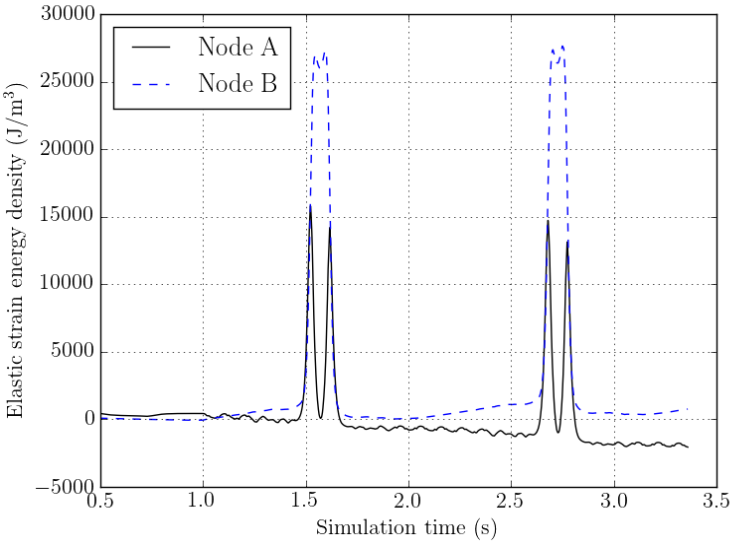

Figure 5.7: History plot of the elastic strain energy density of nodes A and B during the rolling analysis for the 3-D tyre model inflated to 268 kPa and loaded to 74 703 N

The behaviour of hyperelastic material models implies rapid and complete recovery upon deformation. This behaviour implies that the change in the tyre deformation, and evidently the change in elastic strain energy density, will be the same for each revolution. This assumption was verified by Figure 5.7. In Figure 5.7 a history plot of the elastic strain energy density of nodes A and B shown in Figure 5.6 is illustrated. From Figure 5.7 it can be seen that the trends of the change in elastic strain energy density for the selected nodes are the same for each revolution. The specific elastic strain energy density changes, but the change in elastic strain energy density remains the same.

Thus, it was concluded that the theoretical method stated in Section 2.3.3 can be used to calculate the heat generation rate in the tyre using either the first or second revolution of the tyre. The heat generation rate calculated from the elastic strain energy density results was implemented into the thermal model to simulate the temperature distribution in the tyre cross-section. The thermal results are discussed in the following section.

5.2.5 Thermal analysis

The heat generation rate obtained from the elastic strain energy density results were implemented into the 2-D axisymmetric tyre model described in Section 4.2.4. The simulation time of the 2-D thermal models was selected based on the simulated operating time of these model to reach steady-state heat transfer conditions. The resulting simulated operating time was 100 hrs. The maximum temperature in the tyre model at steady-stated heat transfer condition for each combination of the operating conditions were obtained from this analysis. These results are given in Table 5.1. The temperature distribution for each of the thermal models are included in Appendix H.

Table 5.8: Maximum temperature obtained from the thermal analysis of the 2-D axisymmetric tyre models

Tyre pressure	Force	Maximum temperature (°C)		
(kPa)	(N)	15 km/h	30 km/h	45 km/h
200	22 588	33.48	39.88	46.16
	48 656	46.93	63.43	79.25
	74 703	62.86	90.47	116.82
268	22 588	34.20	40.73	46.84
	48 656	45.71	61.66	76.97
	74 703	56.77	80.50	103.15
336	22 588	35.70	43.60	51.06
	48 656	43.56	58.09	72.08
	74 703	54.67	77.29	98.96

From the results obtained it was observed that the exact temperature distribution varied for each model, since each model was subjected to a different combination of operating conditions. However, similar trends were identified from the models subject to under-inflation, the recommended inflation pressure and over-inflation. The models subject to each of these categories are given in Table 5.9.

For the models subjected to under inflation, as seen in Figure 5.8, the maximum temperature occurs at the sidewall. For the tyre models inflated to its recommended pressure, as seen in Figure 5.9, the maximum temperature occurs at the sidewall and in approximately the same region for each model in this category. The maximum

temperature for the models inflated to the recommended pressure occurs closer to the tread region than the under-inflated models.

Table 5.9: Models subjected to under-inflation, over-inflation and the recommended inflation pressure

Under-inflation		Recommended inflation		Over-inflation	
(kPa)	(N)	(kPa)	(N)	(kPa)	(N)
200	48 656	200	22 588	268	22 588
268	74 703	268	48 656	336	22 588
200	74 703	336	74 703	336	48 656

For the models subjected to over inflation, as seen in Figure 5.10, the maximum temperature varies from the sidewall to the middle of the tread. This behaviour is expected, since most of the tyre deformation starts from the first point of contact which is at the middle of the tyre. Thus, the location of the maximum temperature starts at the middle of the tyre, and moves to the sidewall region as the tyre deflection increase.

From the results obtained it was concluded that the location of the maximum temperature is indicative of the point at which the tyre experiences the most deformation during the specific load condition. The location and the value of the maximum temperature will ultimately be a function of the tyre deflection. The tyre deflection is a function of the tyre inflation pressure and load and therefore the tyre inflation pressure and load of the tyre can be used to control the temperature in the tyre.

Furthermore, the temperature increases as the tyre velocity increases. This relation is evident from Equation 2.15, which states that the heat generation rate is directly proportional to the rolling frequency of the tyre. Similar trends were observed by Smith *et al.* (2012), Maritz (2015) and Van Blommestein (2016).

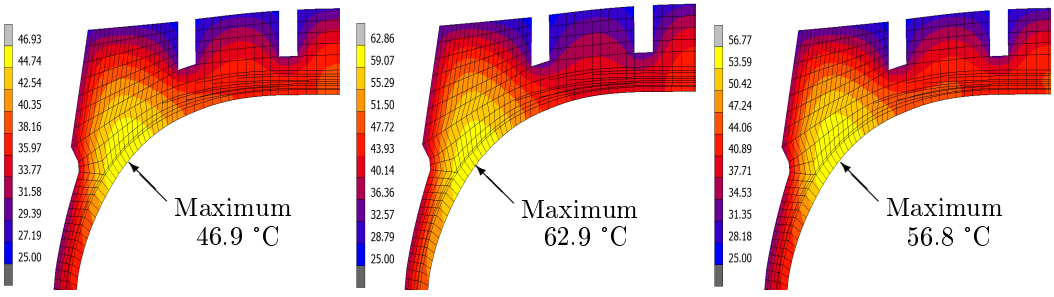

(a) (b) (c)

Figure 5.8: Location of the maximum temperature for the models subjected to under-inflation pressure conditions at 15 km/h: (a) 200 kPa and 48 656 N, (b) 200 kPa and 74 703 N and (c) 268 kPa and 74 703 N

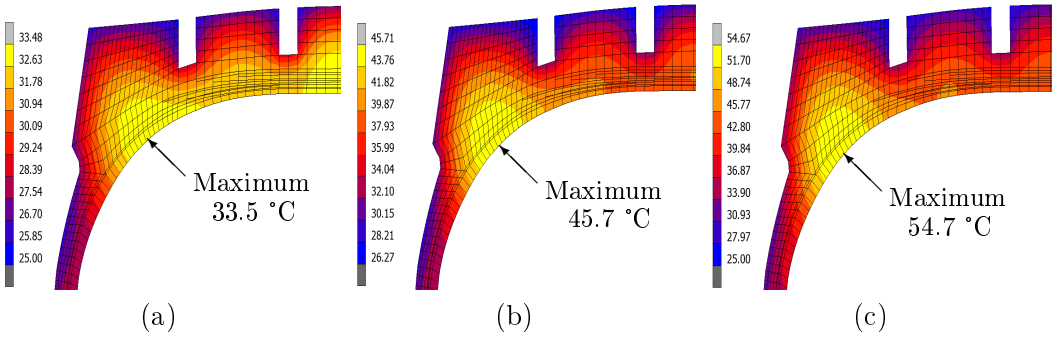

Figure 5.9: Location of the maximum temperature for the models subjected to the recommended inflation pressure conditions at 15 km/h: (a) 200 kPa and 22 588 N, (b) 268 kPa and 48 656 N and (c) 336 kPa and 74 703 N

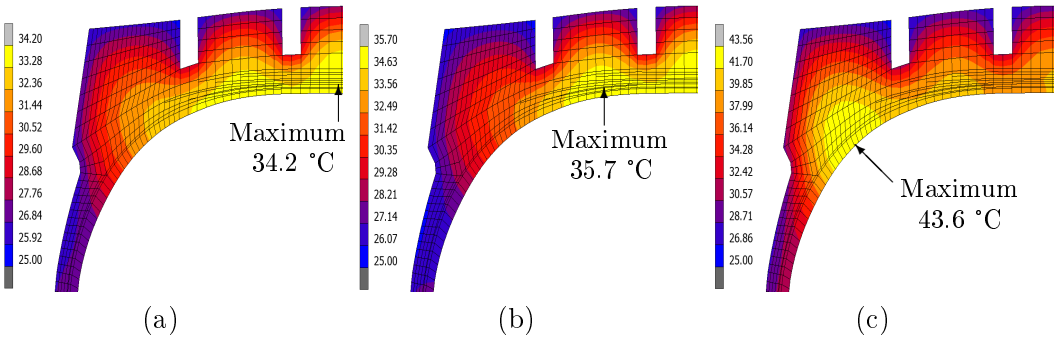

Figure 5.10: Location of the maximum temperature for the models subjected to over-inflation pressure conditions at 15 km/h: (a) 268 kPa and 22 588 N, (b) 336 kPa and 22 588 N and (c) 336 kPa and 48 656 N

As mentioned, the tyre temperatures could not be experimentally verified and the thermal results were compared to similar studies and observations made in industry to give some sort of verification of the maximum temperature readings obtained from the thermal models. Van Blommestein (2016) showed that the numerical temperature readings can be experimentally verified for a passenger vehicle tyre, and the assumption was made that the numerical results obtained from the thermal analysis gives a sufficient representation of the temperature readings in an actual tyre subjected to similar operating conditions.

As mentioned in Chapter 2, the most common rubber polymers used in tyre manufacturing include natural rubber, styrene-butadiene rubber, polybutadiene rubber, butyl rubber, and halogenated butyl rubber (McGarry (2007) and Clark (1981)). In the presence of oxygen it has been found that the highest service temperature styrene-butadiene rubber is 75 °C. For natural rubber and polybutadiene rubber the highest service temperature is 85 °C. For butyl rubber the highest service temperature is 125 °C (Gent, 2012). In industry the recommended internal tyre temperature must be kept below 75 °C during operation to avoid the tyre from reaching excessive

temperatures. At this temperature it has been observed that the degradation of rubber during the chemical reaction known as pyrolysis or thermo-oxidation, as defined in Chapter 1, is likely to occur. Thus, the maximum temperature obtained in the thermal models are consistent with the expected temperatures associated with the degradation of rubber when these tyres are under inflated or the maximum travelling distance per hour is exceeded.

Thus, it was concluded that numerical results were sufficient for the purpose of this project and the thermal results were used to establish a relation between the maximum temperature and the operating conditions.

5.3 Conclusion

This chapter confirms the finite element model developed for a 23.5R25 earthmover tyre. The model was simulated at different combinations of inflation pressures, loads and rolling velocities to evaluate the tyre behaviour during under-inflation, over-inflation and at the recommended tyre inflation pressure. The numerical results were compared to experimental data provided by the tyre manufacturer to evaluate the accuracy of the numerical tyre deflection and contact area. From the results obtained it was concluded that the proposed numerical model sufficiently simulated the actual tyre behaviour. The elastic strain energy density results obtained from the rolling analysis were used to compute the heat generation in the tyre according to the method given in Section 2.3.3. From the results obtained it was concluded that the method is sufficient to compute the heat generation rate in the tyre at steady-state, using either the first or the second tyre revolution, since each revolution yielded the same change in elastic strain energy density.

A thermal analysis of the 2-D axisymmetric tyre model was completed to obtain the temperature distribution in the tyre cross-section at steady-state heat transfer conditions. From the results obtained it was concluded that the location of the maximum temperature in the tyre will occur at the inner radius of the tyre and it will vary from the middle of the tyre to its sidewall region. The location and the value of the maximum tyre temperature will ultimately be a function of the tyre deflection, which can be controlled by adjusting the tyre inflation pressure or the load applied to the tyre. The tyre temperature will increase as the tyre velocity increases. The temperature distribution and maximum tyre temperature were verified by similar studies in literature and observations made in industry.

Based on these verifications, the thermal results were considered sufficient to predict the maximum temperature in the tyre and therefore it was used to describe the maximum temperature in the tyre as a function of its operating conditions. This function will be discussed in Chapter 6.

Chapter 6

Numerical results: Establishing a safe operating envelope

From the results obtained in Chapter 5 it was evident that the tyre temperature increases as its deflection and velocity increases. A scatter plot of the tyre's deflection and the maximum tyre temperature as given in Tables 5.4 and 5.8, are shown in Figure 6.1. Since the recommend internal operating temperature is below 75 °C, the recommended operating envelope is indicated on Figure 6.1 as a dashed box. The tyre deflection and rolling velocities that would result in critical temperature conditions are indicated as the red box in Figure 6.1. It should be noted that the recommended operating envelope has been established at steady-state conditions, which occurred after 28 hrs of the simulated operating time of the 2-D thermal models. A plot of the tyre temperature as a function of the simulation time for nodes A and B of the 2-D thermal tyre models is shown in Figure 6.2.

In order to establish a relation between the maximum tyre temperature and its deflection and velocity a polynomial fit of the data was created for each of the velocity conditions. From the results in Figure 6.1 it was evident that a linear function can be used to describe the maximum tyre temperature as a function of its deflection. The slope of each curve representing the respective velocities increased in a linear manner. The point of intersection of the three curves is at 25 °C and at 0.0132 m deflection off-set. This temperature was equivalent to the ambient temperature specified in the thermal models.

In order to evaluate the influence of the ambient temperature specified for the numerical models, the thermal models were simulated at different ambient temperatures. From these results it was evident that the point of intersection of the three curves will be at the same x-axis off-set of 0.0132 m, but at the corresponding ambient temperate specified for the thermal analysis. The change in temperature will, however, remain the same. This result is expected, since the equations used to calculate convection and conduction heat transfer are linear. These equations are based on the change in temperature, of which the selected ambient temperature is the reference temperature and the heat generation rate is a fixed calculated result.

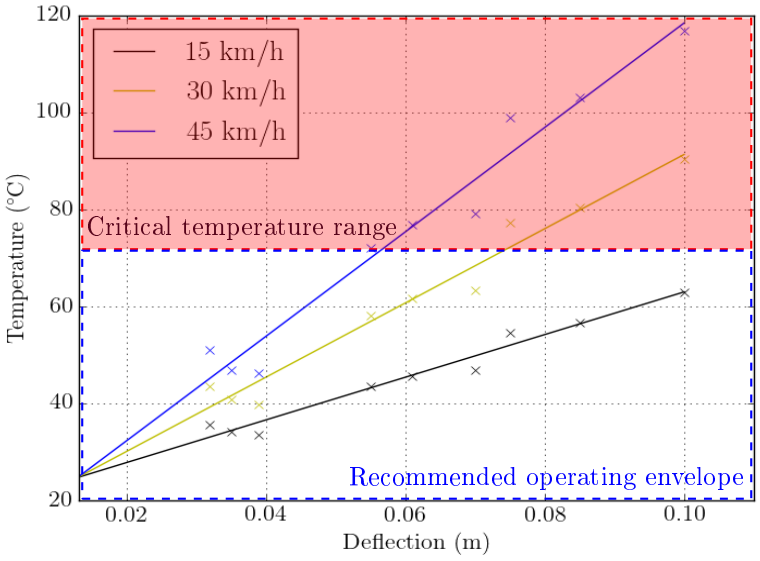

Figure 6.1: Scatter plot and linear curve fit of the maximum temperature in the tyre cross-section as a function of its corresponding numerical deflection at 15, 30 and 45 km/h

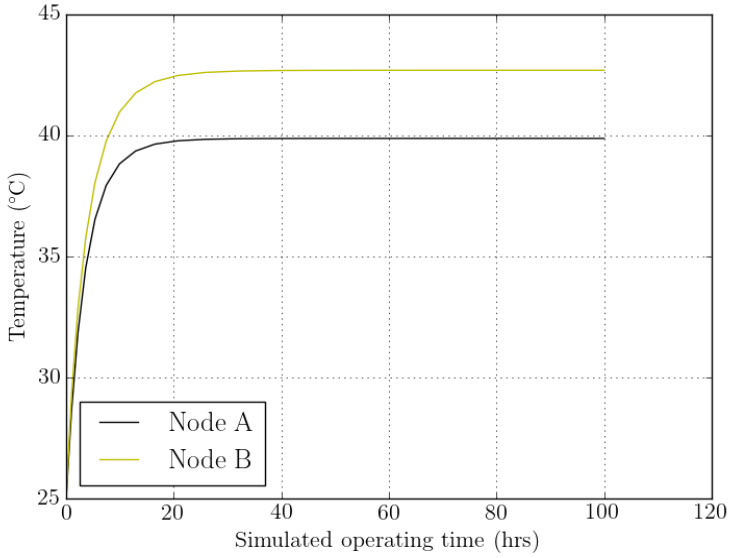

Figure 6.2: History plot of the temperature of nodes A and B as a function of its simulation time for a 2-D axisymmetric model inflated to 268 kPa and loaded to 74 703 N at 15 km/h

From these relations an estimate of the expected maximum tyre temperature as a function of its velocity, its vertical deflection and the ambient temperature specified in the thermal analysis was established. This function is given as,

$$y = (21.25V_t + 123.79)(x - 0.0132) + T_{amb} \tag{6.1}$$

where y is the predicted internal tyre temperature in °C, V_t is the velocity of the tyre in km/h, x is the vertical tyre deflection as defined in Figure 5.3 in m, and T_{amb} is the ambient temperature of its surroundings in °C.

Based on these findings, it was evident that the maximum temperature in the tyre can be controlled by either adjusting the tyre deflection or velocity at the specified ambient conditions. The tyre's deflection can be controlled by adjusting either the inflation pressure or the applied load to maintain a safe operating envelope. At full-payload haul trucks usually carry less load than the maximum load the tyre can actually carry, and therefore it is suggested that these tyres should rather be slightly over-inflated during operation to reduce excessive heat generation. This may result in uneven tread wear, but not to an excessive extent. Furthermore, from the results obtained, it was evident that the tyre velocity will have the most significant influence on the heat generation in the tyre. This result is expected since the method used to calculate the heat generation rate, as stated in Equations 2.15 and 2.16, is directly proportional to the rolling velocity of the tyre.

In order to establish a correlation between the recommended travelling distance per hour and the deflection of the tyre at the specified inflation pressure and load indicated on the sidewall markings, Equation 6.1 was used to predict the maximum temperature in the tyre at these conditions. When the tyre under investigation is inflated to 450 kPa and loaded with 90 742 N a deflection of 0.087 m and recommended travelling distance of 28 km per hour is specified in the user and maintenance guide. The maximum predicted tyre temperature at steady-state operation and at 25 °C ambient temperature conditions, is 78.05 °C. Similarly, for a tyre with a deflection of 0.116 m and maximum recommended travelling distance of 16 km per hour, as specified in the user and maintenance guide, the maximum predicted tyre temperature is 72 °C. In these examples the maximum predicted temperature slightly exceeds or is close to the recommended tyre temperature of 75 °C. Thus, a general correlation can be established between the recommended travelling distance and the vertical tyre deflection stated in the user and maintenance guide for earthmover tyres at its specified inflation pressure and load indicated on the sidewall markings.

Based on these findings, it was concluded that the function in Equation 6.1 provides a realistic estimate of the maximum tyre temperature of the haul tyres based on its recommended travelling distance per hour and its specified deflection at the indicated inflation pressure and load sidewall markings, independent of its size. It should be noted that this prediction is at steady-state conditions and could therefore be considered conservative, but considering the implications of excessive heat generation in these tyre, it is preferable. In order to maintain safe operation the

recommended travelling distance per hour given in the user guide should be reduced by one quarter of its specified speed when the vehicle is operating at full-payload. At no-load, these tyres can be operated at its maximum rated velocity, which is 50 km/h for the tyre under consideration.

It should be noted the function described in Equation 6.1 is based on the numerical results obtained from the thermal analysis and it was not experimentally verified. The experimental validation of the thermal results are recommended to determine the accuracy of this function, although it was concluded that the predicted temperatures are consistent with that which would be expected in industry.

Chapter 7

Conclusion and recommendations

7.1 Project conclusion

The project considered in this study was the third part of an investigation for Anglo to develop a numerical model of an earthmover tyre that can be used to predict the temperature in the tyre cross-section. The methodology used to develop a numerical model of an earthmover tyre and simulate its temperature distribution was based on the work completed by predecessors Maritz (2015) and Van Blommestein (2016) which completed the first and second part of the investigation, respectively.

The aim of this project was to develop a numerical model of an earthmover tyre that can be used to represent the temperature distribution in the tyre cross-section. The purpose of these results was to obtain a relationship between the maximum temperature in the tyre and its operating conditions. These conditions included different inflation pressures, loads and rolling velocities. This relation could in turn be used to predict the maximum temperature in the tyre at steady-state heat transfer conditions to ensure safe operation.

The numerical model was developed from measurements of a segment of a 23.5R25 earthmover tyre donated by Anglo. Samples were cut from this segment to determine the tyre's components and its material properties. These properties were verified and implemented into the numerical model.

An uncoupled analysis procedure was used to numerically simulate the temperature distribution in the tyre during steady-state heat transfer conditions. This analysis procedure included the inflation, loading and rolling of the tyre model and a thermal analysis of the 2-D axisymmetric tyre model. The elastic strain energy density was obtained from the rolling analysis and it was used to calculate the heat generation rate in each element according to the method described in Section 2.3.3. The tyre models were subjected to each of the operating conditions given in Table 5.1.

The accuracy of the proposed models was evaluated by comparing the numerical results to experimental data provided by the tyre manufacturer. From the results obtained it was concluded the numerical tyre results were consistent with the exper-

imental data within a maximum percentage difference of 3.9 %, 2.5 %, 3.4 % and 9.7 % for the vertical tyre deflection, the overall tyre width, the tyre's contact width and the tyre's contact length, respectively. This percentage difference was considered sufficiently accurate to numerically represent the deformation of the actual tyre during static loading. Furthermore, it was concluded that most of the tyre deformation will occur in its sidewall due to the radial construction of the tyre. This construction ensures that the tread makes contact across the entire tread width to ensure even tread wear during loading. The overall tyre width, the contact width and length is a function of the tyre deflection and each of these parameters will increase as the tyre deflection increases. The tyre deflection will increase as the inflation pressure decreases or the load increases.

Since the elastic strain energy density and the thermal results could not be experimentally validated, the assumption was made that the accuracy of the static tyre behaviour could be used to provide some measure of verification of the elastic strain energy density and the thermal results. This assumption was based on the theoretical description of the elastic strain energy density in the rubber during deformation and the method used to calculate the heat generation rate in numerical models during deformation. According to this description, the elastic strain energy density will purely be a function of the rubber deformation during loading. The heat generation rate will be a function of the elastic strain energy density, which is a function of the tyre deformation during loading, and the rolling velocity of the tyre.

From elastic strain energy density results it was concluded that the method used to calculate the heat generation rate in the tyre was sufficient to simulate the temperature distribution in the tyre. This conclusion included that the heat generation in the tyre can be computed from the elastic strain energy density results using either the first or the second tyre revolution. From the results obtained from the thermal analysis, it was concluded that the location of the maximum temperate in the tyre will occur at the inner radius of the tyre and it will vary from the middle of the tyre to its sidewall region. The location and the value of the maximum tyre temperature will ultimately be a function of its deflection and velocity. Since the tyre's deflection is a function of the inflation pressure and load applied to the tyre, the maximum tyre temperature can be controlled by adjusting either the tyre inflation pressure, the load applied to the tyre or its velocity. The thermal results were compared to similar studies in literature and observations made in industry to give some measure of verification, since it could not be experimentally verified.

A linear function of the predicted tyre temperature was derived from the results of the thermal analysis. This function predicted the maximum temperature in the tyre cross-section in terms of its deflection, its velocity and the ambient temperature specified in the thermal analysis at steady-state heat transfer conditions. This function could unfortunately not be experimentally verified, but was considered sufficient to be used as an estimate to predict the maximum temperature in the tyre during operation to prevent the explosion of these tyres. This function is given in Equation 6.1.

Considering different tyres and tyre sizes it was established that the tyre deflection and recommended travelling distance given in the user and maintenance guide for the different tyre sizes at its rated inflation pressure and load given on the sidewall markings had a general correlation. From this correlation, it was evident that the function given in Equation 6.1 can be used to predict an estimate of the expected maximum temperature in the tyre for any earthmover tyre size. However, this may be a gross estimation and therefore this function must be experimentally validated before this conclusion can be drawn.

As a final remark, in order to maintain a safe operating envelope based on the findings of this project, it was evident that the maximum temperature in the tyre can be controlled by either adjusting the tyre deflection or velocity at the specified ambient conditions. The tyre's deflection can be controlled by adjusting either the inflation pressure or the applied load to maintain a safe operating envelope. At full-payload haul trucks usually carry less load than the maximum load the tyre can actually carry and these tyres are slightly over-inflated, and therefore it is not likely that excessive heat generation will occur due to excessive deformation, but rather when the rolling velocity or maximum recommended travelling distance of the tyre is exceeded while transporting a load. Thus, the tyre velocity will have the most significant influence on the heat generation in the tyre and should therefore be managed accordingly. This result is expected since the method used to calculate the heat generation rate, as stated in Equations 2.15 and 2.16, is directly proportional to the rolling velocity of the tyre.

7.2 Recommendations

The experimental validation of the maximum temperature in the tyre must be completed to verify the results obtained. If the numerical and experimental results are consistent, the function derived in Equation 6.1 can be verified and used to predict the maximum temperature in the tyre. If this function can be experimentally verified for any earthmover tyre size, it can be used to manage the heat generation in the tyres while improving the efficiency of the mine.

Appendices

Appendix A

Tyre specifications and load conditions

The specifications and load conditions for a 23.5R25 earthmover tyre, similar to the tyre of which the donated segment was cut from, are summarised in this appendix. These specifications were obtained the user and maintenance guide for earthmover tyres as provided by the manufacturer.

A.1 Tyre specifications

The tyre dimensions and specifications of a 23.5R25 earthmover tyre are given in Table A.2. These parameters were used to adjust the measured tyre geometry established from the used tyre segment to that of a new tyre. The corresponding inflation pressures and loads are given in Table A.2.

Table A.1: A summary of the specifications of a 23.5R25 earthmover tyre

Specification	Value
Standard section width	0.600 m
Standard section height	0.478 m
Tyre diameter inflated to 450 kPa	0.806 m
Rolling radius	0.771 m
Rim diameter	0.635 m
Tread depth	0.038 m
Maximum load index	9250 kg
Maximum speed at load index	50 km/h
Maximum distance per hour	28 km
Ton kilometre per hour (TKPH)	207

Table A.2: Recommended inflation pressures and loads

Pressure (kPa)	200	250	300	350	375	400	450	500
Load (kg)	5650	6380	7100	7800	8175	8550	9250	10350

A.2 Rim specifications

25-19.5/2.5 inch five piece 5° taper bead seat rims are generally recommended for 23.5R25 earthmover tyres. The recommended rim type and its dimensions were used to model the rim profile. The definition of the rim components and its dimensions are given in Figure A.1 and Table A.3, respectively. These dimensions were obtained from Topy (2008) and Canadian Wheel (2012).

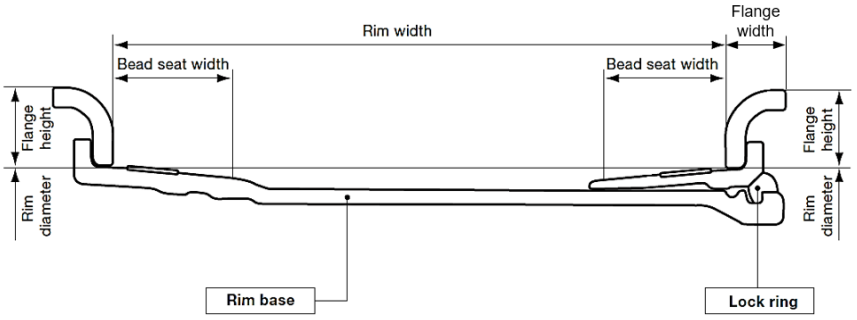

Figure A.1: Definition of the different components in a five piece 5° taper bead seat rim (adapted from Topy (2008))

Table A.3: Dimensions of a 25-19.5/2.5 inch five piece 5° taper bead seat rim

Rim diameter (m)	Rim width (m)	Bead seat width (m)	Flange height (m)	Flange width (m)
0.6350	0.4950	0.1270	0.0635	0.0445

A.3 Operating loads

The earthmover tyre under investigation are typically used for articulated dump trucks such as the Bell B25E machine. The operating loads of this specific truck were used to obtain an estimate to determine the typical loads the tyre would be subjected to in industry. The operating weights of each axle during no-load (unladen) and full payload (laden) are given in Table A.4. Each axle consist of two tyres in total and the different axles are indicated on Figure A.2. The load specifications of the Bell B25E machine were obtained from Bell (2015*a*) and Bell (2015*b*).

Table A.4: Bell B25E articulated dump truck operating weights and ground pressures

Operating weights	Unladen (kg)	Laden (kg)
Front	9 740	12 480
Middle	4 605	15 235
Rear	4 565	15 195
Total	18 910	42 910
Ground pressure	**Laden (no sinkage) (kPa)**	**Laden (15 % sinkage) (kPa)**
Front	244	225
Middle	336	279
Rear	336	279

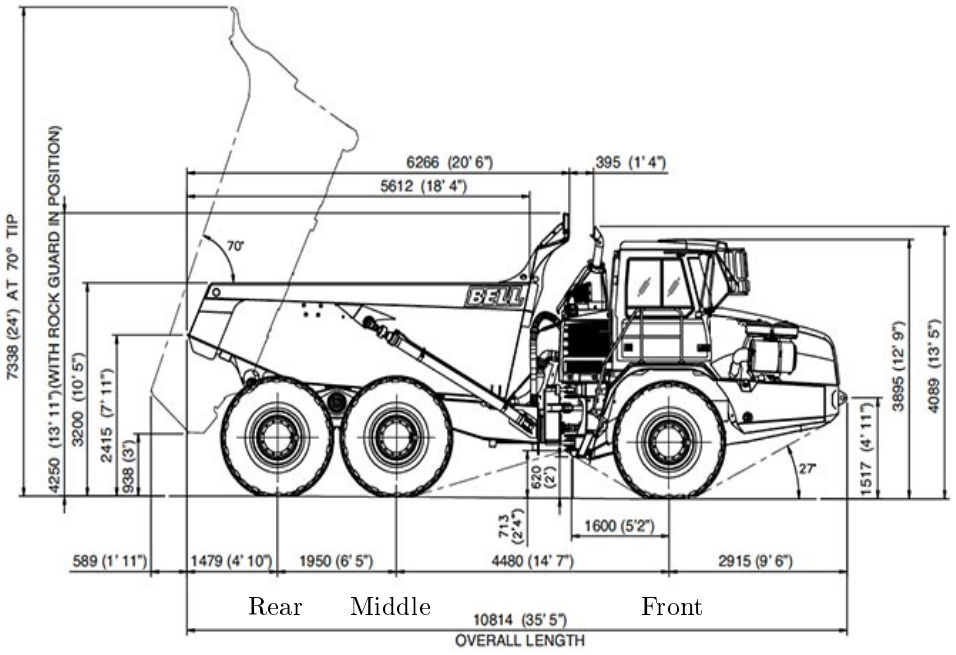

Figure A.2: Front, middle and rear axles shown on a blueprint of a Bell articulated dump truck (adapted from Bell (2016))

Appendix B

Computed tomography scan

An illustration of the computed tomography (CT) scan of the cords used in the belts and body ply are given in this appendix. The CT-scan was completed at the CT scanner facility at Stellenbosch University. A direct tube micro-CT system with a typical voxel dimension of 0.09 mm was used to complete the CT-scan. Figures B.1(a) to (f) illustrates the spacing and the angle of the cords with respect to the positive z-axis.

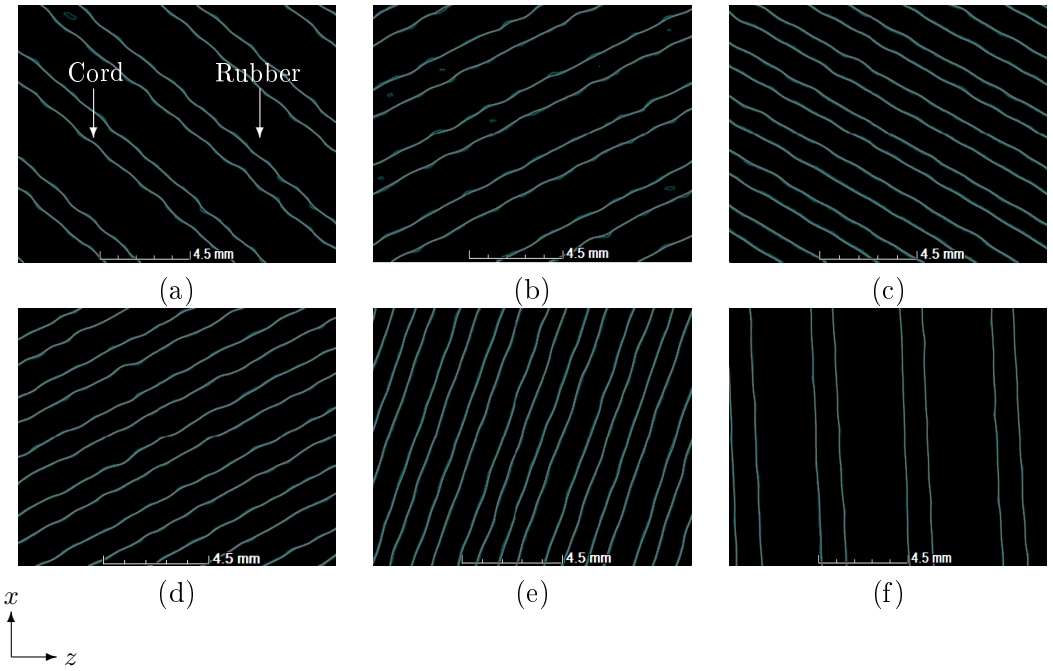

Figure B.1: CT-scan of the cord spacing and angle with respect to the positive z-axis in: (a) belt 1 (-45°), (b) belt 2 (30°), (c) belt 3 (-38°), (d) belt 4 (30°), (e) belt 5 (70°) and (f) body ply (90°)

Appendix C

Tensile and compression tests

This appendix describes the sample preparation, the methodology and the results obtained from uniaxial tensile and compression tests performed on the structural components and rubber compounds identified from the donated tyre segment. First, the uniaxial tensile tests performed on the bead wire and the cords used in the belts and body ply are discussed. Second, the uniaxial tensile tests performed on the inner liner rubber compound and the tensile and compression tests performed on the sidewall and tread rubber compounds are discussed.

C.1 Equipment specifications and calibration

The uniaxial tests were performed on the Material Testing System (MTS) Criterion Model 44, at the Department of Mechanical and Mechatronic Engineering at Stellenbosch University. A 30 kN high-accuracy load cell was used in combination with the MTS test machine set-up. This load cell includes a transducer electronic data sheet that allows the automatic identification and calibration of the MTS system. The MTS set-up is shown in Figure C.1.

C.2 Uniaxial tensile tests

This section describes the uniaxial tensile tests performed on the bead wire, the cords used in the belts and the body ply, the inner liner, the sidewall and the tread rubber compounds. The standard test method for tension testing of metallic materials as given by ASTM E8/E8M-11 (2011) and the standard test method for tension testing of single-filament tyre bead wire made from steel as given by ASTM D4975-04 (2011) were used as guidelines to perform the tensile tests on the structural components. The standard test method for tension testing of vulcanised rubber and thermoplastic elastomers as given by ASTM D412-06a (2013) was used as a guideline to cut, prepare and perform tensile tests on the rubber compounds.

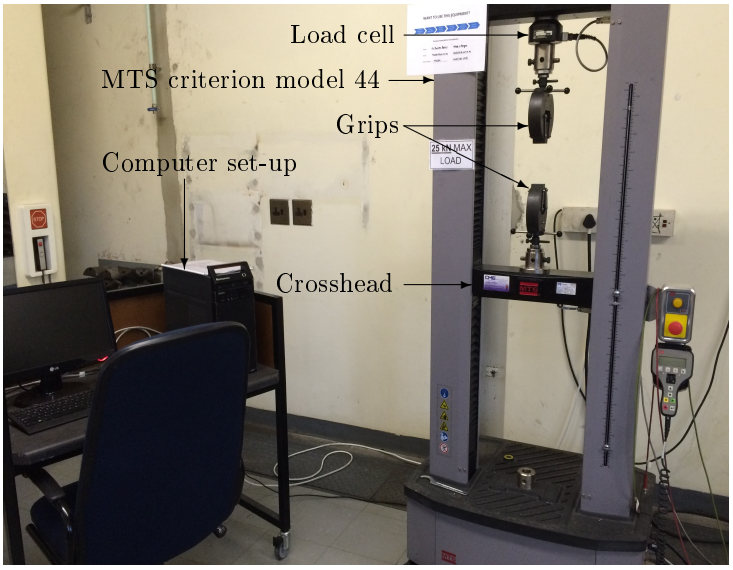

Figure C.1: Computer and MTS Criterion Model 44 set-up at the Mechanical and Mechatronic Engineering Department at Stellenbosch University

C.2.1 Methodology

The general procedure to perform the tensile tests on the MTS machine are as follow:

1. Set-up the software in TestWorks according to the test template provided by Stellenbosch University as given by Van Rooyen (2015).

2. Clamp each end of the sample in grips and set the load and the crosshead to zero.

3. Increase the crosshead extension until the sample breaks or the desired maximum load is achieved.

4. Record the change in force and the crosshead extension during testing using the software provided. The data can be used to obtain the force-extension curve of the sample.

A MFA 25 extensometer was used to measure the extension the steel cords and bead wire since metals tend to slip in the grips. The gauge length of the MFA 25 extensometer was 0.025 m. The gauge length is defined as the distance between the two points where the measurement of strain occurs.

C.2.2 Calculating material properties

The force-extension curve obtained from the MTS tensile tests was used to calculate the stress-strain curve of the material. The equations used to calculate these curve are given in this section.

There are two types of stress-strain curves, namely, engineering and true stress-strain curves. Engineering stress can be calculated from the applied force using,

$$\sigma_e = \frac{F}{A_0} \tag{C.1}$$

where σ_e is the engineering stress (Pa), F is the load applied (N), and A_0 is the original cross-sectional area of the specimen (m^2).

Engineering strain can be calculated from the extension using,

$$\epsilon_e = \frac{l - l_0}{l_0} \tag{C.2}$$

where ϵ_e is the engineering strain (mm/mm), l is the gauge length when loaded (m), and l_0 is the original gauge length of the specimen (m). In the low strain portion of the stress-strain curve, linear-elastic materials tend to obey Hooke's law to a reasonable approximation. Hooke's law implies that the stress is proportional to strain with a constant of proportionality known as the modulus of elasticity or Young's modulus, E (Roylance, 2001):

$$E = \frac{\sigma_e}{\epsilon_e} \tag{C.3}$$

The Young's modulus is a measure of a material's stiffness. The higher the Young's modulus, the stiffer the material. However, as the strain increases the material behaviour will start to deviate from this linear proportionality. Beyond this point the specimen dimensions experience substantial change from their original values. This behaviour can be accommodated by measuring the cross-sectional area of the specimen simultaneously. This material behaviour can be represented by true stress-strain curves.

The true strain, ϵ_t, of a material can be described as the sum of the incremental elongations divided by its current length:

$$\epsilon_t = \int_{l_0}^{l} \frac{dl}{l} = \ln \frac{l}{l_0} \tag{C.4}$$

The resulting true stress, σ_t, can be then calculate as:

$$\sigma_t = \sigma_e \frac{l}{l_0} \tag{C.5}$$

C.2.3 Tensile tests: Belts, body ply and bead

The sample preparation and tensile test results of the bead wire and the cords used in the belts and body ply are discussed in the section. This discussion includes the influence of the cord arrangement on the cord behaviour.

C.2.3.1 Sample preparation

The steel cords and bead wire were separated from rubber by burning pieces cut from the donated tyre segment in an open flame set-up. All the access rubber was cut from these pieces and it was burnt until the steel cord could drawn from the rubber to keep the temperature of the set-up as low as possible. It was assumed that this method can be used to separate the structural components from the rubber and used it for tensile testing, since this set-up will not reach the critical temperatures associated with a significant effect on the material properties of steel.

This assumption was based on the following statements: tyres can decompose in a open flame set-up at temperatures as low as 210 °C (Stambaugh and Banks, 1998), while the critical temperatures typically associated with a significant effect on the material properties of steel range from 900 °C to 1200 °C (SteelConstruction.info, 2012). Since the temperature of the open flame set-up was assumed to be much lower than that of the critical temperatures required to change that material properties of steel, the cords and bead wire were selected from the burnt sections and cleaned for tensile testing.

C.2.3.2 Results

Tensile tests were performed on the structural components to establish an estimate of the allowable load before the components would break without using an extensometer. The reason for these tests were to establish the linear region of the components, since only the linear region of the components were required to calculate its Young's modulus and extensometers are very sensitive instruments and should preferably not be exposed to the breaking of a component during tensile testing. Based on these results, three set of uniaxial tensile tests were performed on the structural components within its linear region. The test set-up is shown in Figure C.2.

From the results obtained, it was concluded that the cords with similar constructions yielded similar results. Thus, only the results of the bead wire and cords used in belts 1 and 5 and the body ply are included in this section, since each of these component represented a different construction, as discussed in Section 3.3.2. The stress-strain curves for the cords in each of the respective components are shown in Figures C.3 to C.6. These figures includes the average of the data sets. The test speed and data acquisition rate for each component are given in Table C.1.

C.2.3.3 Discussion and conclusion

The tendency of the stress-strain curves obtained form the tensile test data are compared to the expected cord behaviour described in literature to evaluate the tendency of the results obtained, since the cord arrangement influences the overall cord behaviour. The expected tendency of different cord arrangements are shown in Figure C.7.

The cord arrangements of the selected structural components, as defined in Section 3.3.2, include a 3x6 arrangement for the cords used in belts 1 and 2, a 1x27

arrangement for the cords used in belts 3 and 4 and the body ply, and a 1x12 arrangement for the cords used in belt 5.

According to the expected tendencies shown in Figure C.7 it can be seen that for a multi-strand arrangement, such as the 7x7 arrangement, a slightly non-linear curve is expected, which is similar to that obtained for the cords used in belts 1 and 2. For single strand arrangements, such as the 1x7 and 1x19 a more linear curve than that of a multi-strand arrangement is expected. A similar tendency was obtained for the cords used in belts 3, 4, 5 and the body ply.

The stress-strain curve of the bead wires were completely linear. This behaviour was expected since the individual steel wires used for the tensile tests and were known to have linear-elastic material behaviour.

Based on the results obtained, it was concluded that the tendency obtained from the results of the tensile tests were consistent with the expected cord behaviour given in literature. Thus, the tensile tests results were considered sufficient to determine the Young's modulus of the structural components.

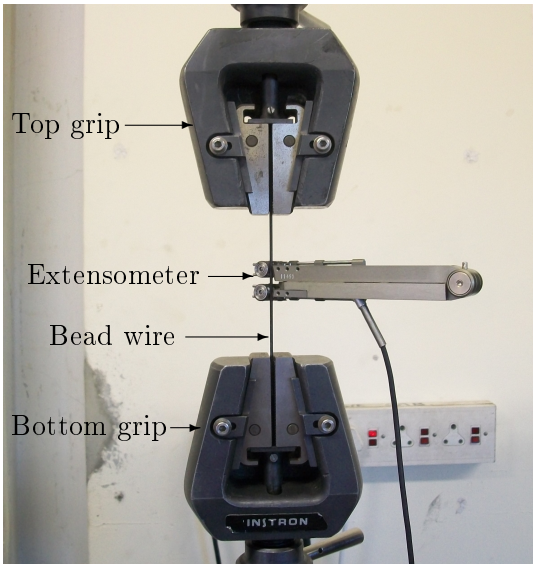

Figure C.2: MTS set-up of a bead wire and MFA 25 extensometer

Table C.1: Test speed and data acquisition rate of the bead wire and the cords

	Test speed (mm/min)	Data acquisition rate (Hz)
Belt 1, 5 and body ply	1	20
Bead wire	4	20

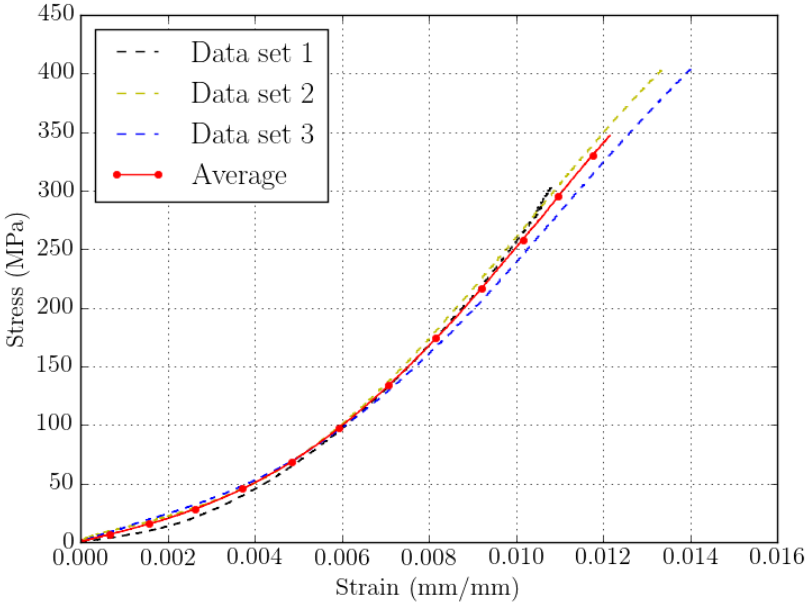

Figure C.3: The cords used in belt 1: stress-strain curve of the data obtained from the tensile tests and the average of the data sets

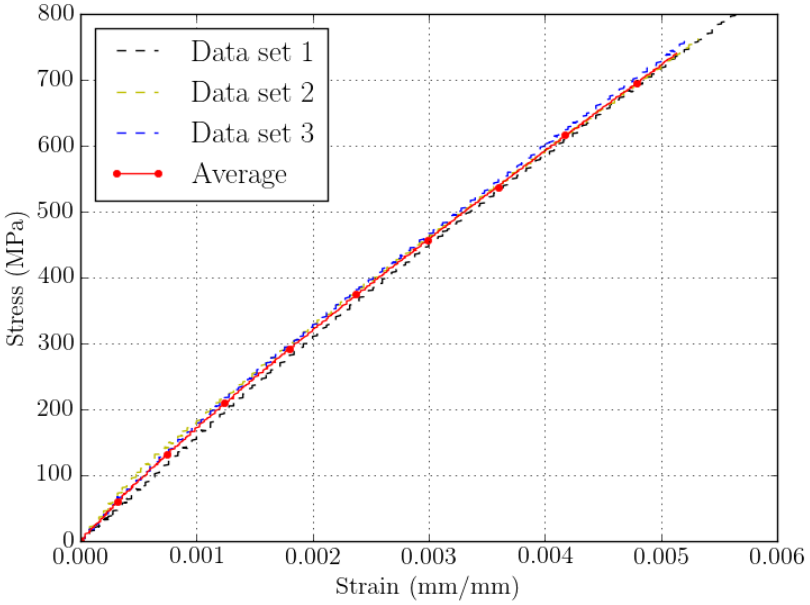

Figure C.4: The cords used in belt 5: stress-strain curve of the data obtained from the tensile tests and the average of the data sets

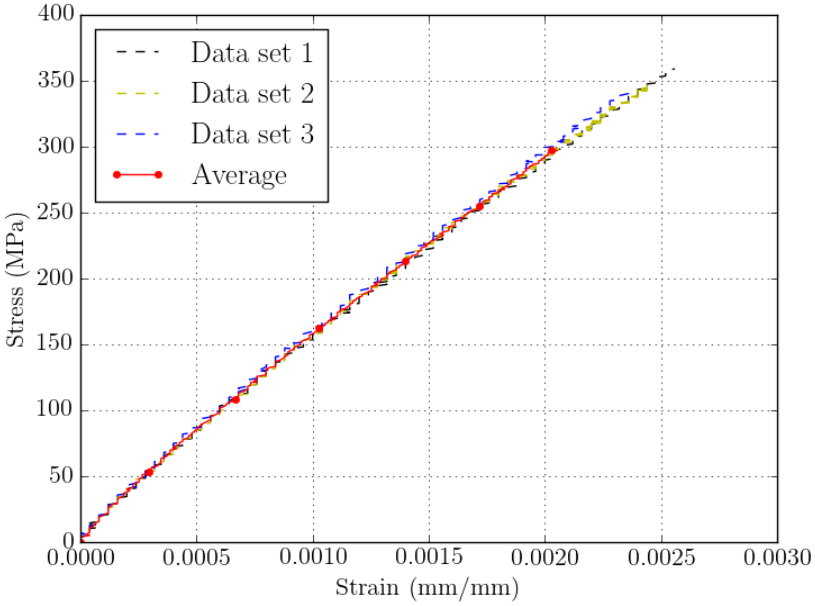

Figure C.5: The cords used in body ply: stress-strain curve of the data obtained from the tensile tests and the average of the data sets

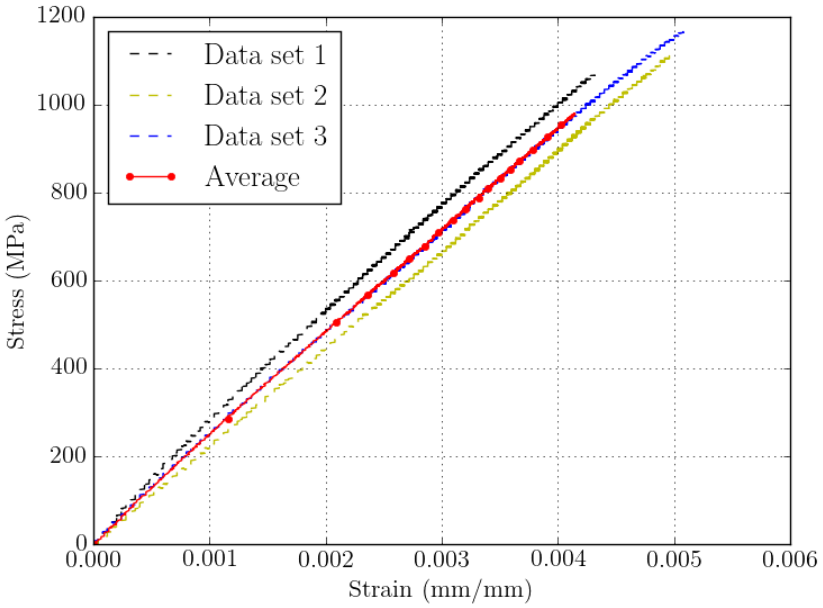

Figure C.6: Bead wire: stress-strain curve of the data obtained from the tensile tests and the average of the data sets

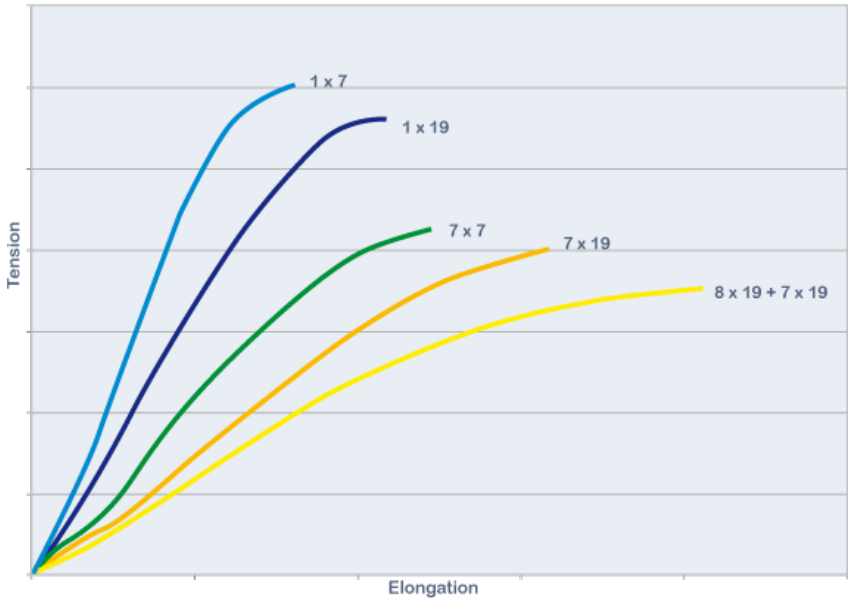

Figure C.7: Tendency of the different cord arrangements (Carl Stahl Technocables, 2016)

C.2.4 Tensile tests: Tread, sidewall and inner liner rubber

The tread, sidewall and inner liner rubber compounds were selected for tensile tests. The results were used to determine the stress-strain behaviour of the selected rubber compounds. The sample preparation and the results of the tensile tests are given in this section.

C.2.4.1 Sample preparation

Samples of tread, sidewall and inner liner rubber compounds were cut from the provided tyre segment. The samples were cut into a dumbbell shaped specimens using waterjet cutting. The dumbbell shape and dimensions are given in Figure C.8. The thickness of the tread, sidewall and inner liner were 0.010 m, 0.008 m and 0.007 m, respectively. The samples are shown in Figure C.9.

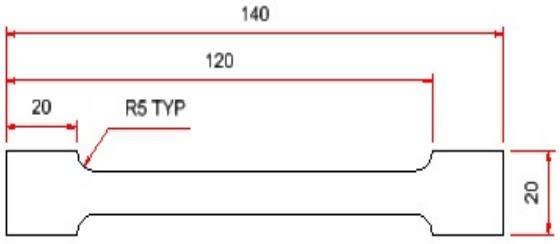

Figure C.8: Dumbbell dimensions

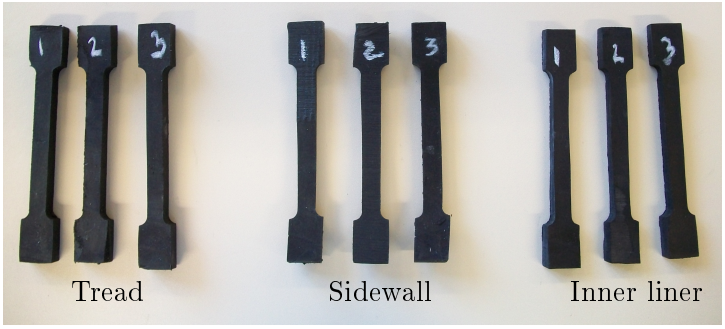

Figure C.9: Dumbbell shaped samples of the tread, sidewall and inner liner rubber compounds used for tensile testing

C.2.4.2 Results

Three sets of tensile tests were completed for each of the rubber compounds. The stress-strain curves of the data sets and the average of the sets of the inner liner, sidewall and tread rubber compounds are shown in Figures C.10, C.11 and C.12, respectively. The test speed and data acquisition rate for each of the samples were 25 mm/min and 25 Hz, respectively.

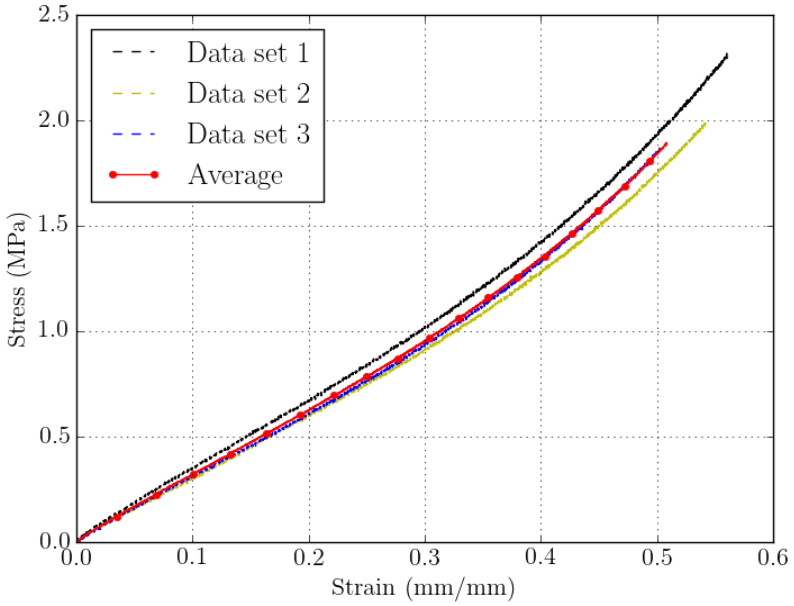

Figure C.10: Inner liner rubber: stress-strain curve of the tensile tests data sets and the average of the data sets

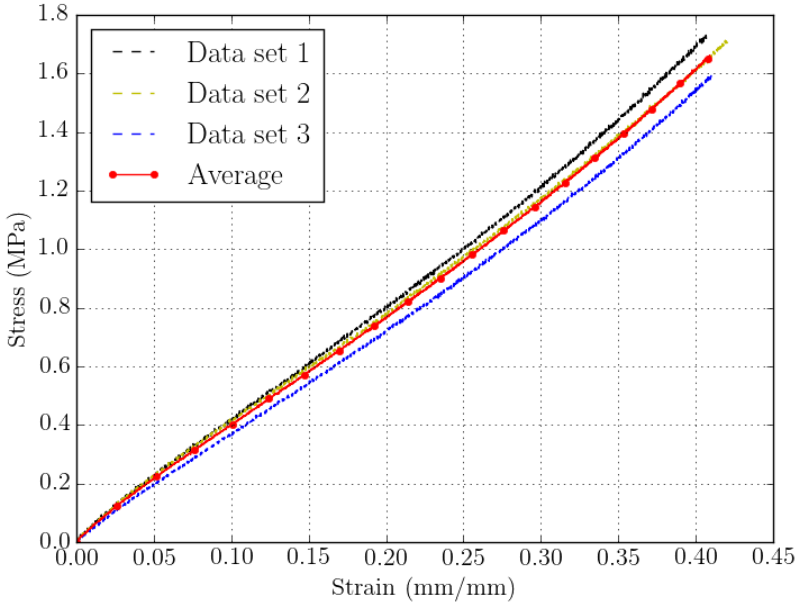

Figure C.11: Sidewall rubber: stress-strain curve of the tensile tests data sets and the average of the data sets

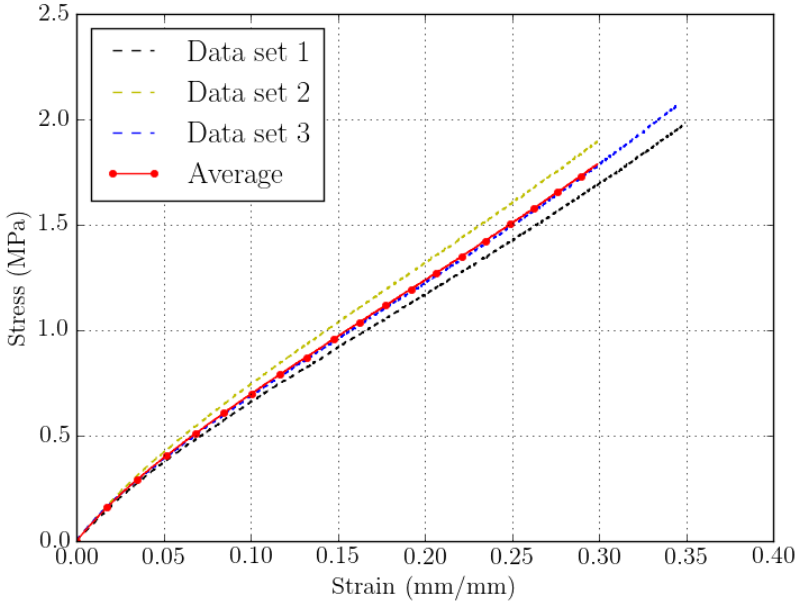

Figure C.12: Tread rubber: stress-strain curve of the tensile tests data sets and the average of the data sets

C.2.4.3 Discussion and conclusion

From the results obtained, it can be seen that the trend of each data set is consistent with the rubber compound under investigation. The average of the data sets for the stress-strain curve of the linear, sidewall and tread rubber in tension are shown in Figure C.13. From this comparison it can be seen that the liner is the most elastic rubber compound, then the sidewall, and then the tread. This trend was expected since the rubber hardness is typically indicative of its strength and the tread compound had the highest hardness value, then the sidewall and then the inner liner, as seen in Appendix D. Thus, it was concluded that the results obtained were considered sufficient to describe the material behaviour of the selected rubber compounds in tension.

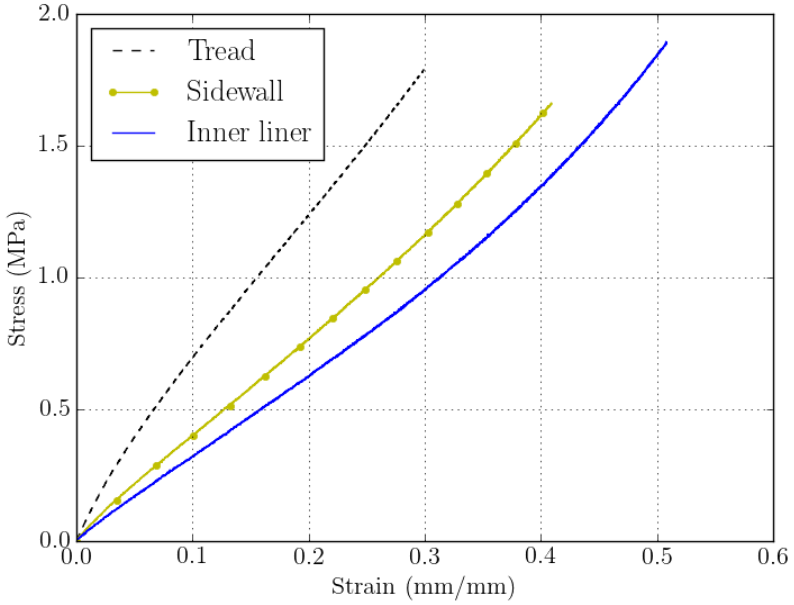

Figure C.13: Stress-strain curves of the average of the data sets for the inner liner, sidewall and tread rubber in tension

C.3 Uniaxial compression tests

This section describes the sample preparation, the methodology and the results obtained from the uniaxial compression tests. These tests were performed on the sidewall and tread rubber compounds. The standard test method for rubber properties in compression as given by ASTM D575-91 (2012) was used as a guideline to cut, prepare and perform the compression tests on the rubber compounds.

C.3.1 Sample preparation

Samples of the tread and sidewall rubber were cut from the tyre segment using a 0.032 m diameter hole saw. Since the rubber tends to grab the hole saw, the resulting average sample diameter was 0.0292 m. The samples were evened with a grinder and A36 Aluminium Oxide sanding disks. The resulting sample thickness was 0.0113 m and 0.0107 m for the sidewall and tread rubber, respectively. The samples are shown in Figure C.14.

Tread rubber Sidewall rubber

Figure C.14: Tread and sidewall rubber samples used for the compression tests

C.3.2 Methodology

The compression test set-up is shown in Figure C.15. The procedure for performing compression tests on rubber compounds using the MTS machine are as follow:

1. Set-up the software in TestWorks according to the compression test template provided by Stellenbosch University as given by Van Rooyen (2015).

2. Place the sample between the platens. Place a sheet of sandpaper between the rubber surfaces and the testing machine platens. The sandpaper resists lateral slippage of the rubber contact surface and should be slightly larger than the specimen (ASTM D575-91, 2012).

3. Set the load to zero. Move the crosshead until the load slightly increases and set it to zero.

4. Move the crosshead until the desired deflection is reached. When the specified deflection is reached, release the force at the same rate and the repeat the loading cycle a second time, and then a third.

5. Record the force required to obtain the specified deflection. Report the median values taken from three samples.

Table C.2 lists the specifications used for the compression test template, in which the platen separation refers to the minimum distance the top and bottom platen must be set to accommodate the sample thickness with no pre-load. P600C Aquaflex waterproof sandpaper was used for the compression test set-up.

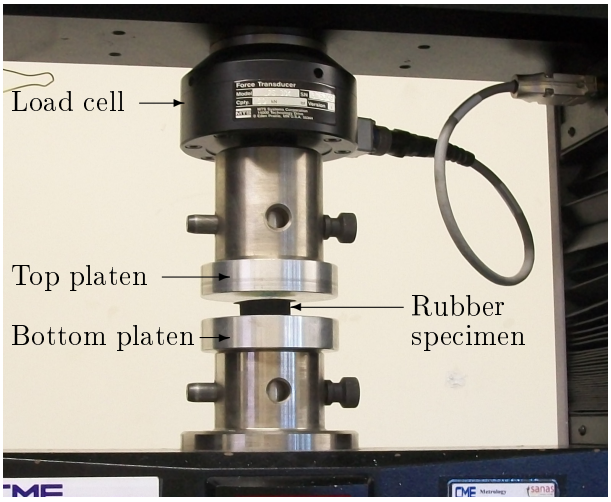

Figure C.15: MTS rubber compression test set-up

Table C.2: Compression test specifications

Test speed (mm/min)	10
Data acquisition rate (Hz)	25
Platen separation (mm)	12
Pre-load (N)	50
Pre-load speed (mm/min)	10
Strain-end point (mm/mm)	0.67

C.3.3 Calculating material properties

The force-deflection curves of the selected rubber samples were obtained from the MTS compression tests. These curves were used to calculate the stress-strain curves of each rubber compound using the equations given in Section C.2.2. In practice the engineering stress and strain are used to calculate the compressive strength of the samples although its original cross-sectional area increases as a function of the applied load due to spread in the lateral direction.

On compression, the specimen will shorten and tend to spread in the lateral direction. The sandpaper resists lateral slippage of the rubber at the contact surfaces and as a result a frictional force will arise to oppose the lateral spread. The work done to oppose this force increases the energy consumed during the process. This can cause substantial shearing strains that can alter the stress response to straining. However, the lateral friction force of rubber is not well characterised since it varies from the centre of the sample to the outer region (Axel, 2015). Consequently the experimental compression data cannot be corrected with a significant certainty and therefore it was neglected in the calculation of the compression stress-strain curves of the samples.

C.3.4 Results

The median of the three samples were used to represent the measured data of each rubber compound (ASTM D575-91, 2012). The stress-strain curves of the sidewall and tread rubber compounds are shown in Figures C.16 and C.17, respectively.

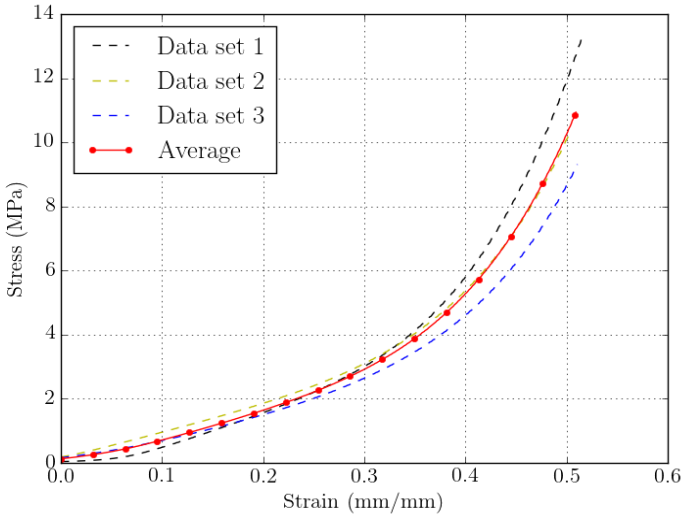

Figure C.16: Sidewall rubber: stress-strain curve of the compression tests data sets and the average of the data sets

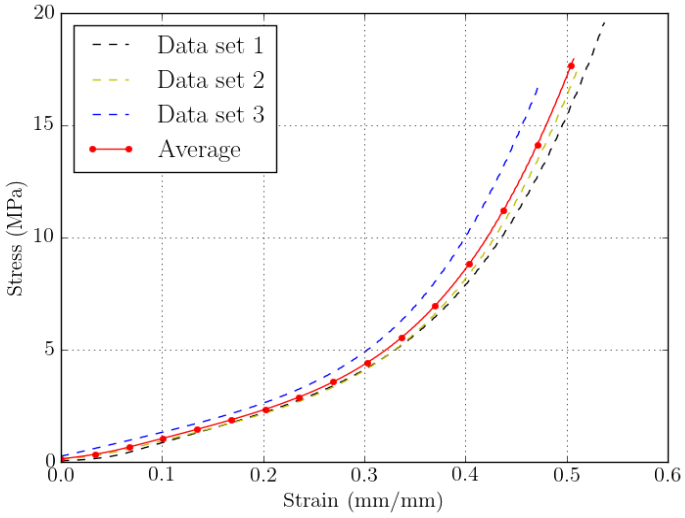

Figure C.17: Tread rubber: stress-strain curve of the compression tests data sets and the average of the data sets

C.3.5 Discussion and conclusion

From the results obtained, it can be seen that the trend of each data set is consistent with the rubber compound under investigation. The stress-strain curve of the sidewall and tread rubber in compression is shown in Figure C.18. From this comparison it can be seen that the sidewall rubber is less stiff than the tread rubber. This trend was expected since the rubber hardness is typically indicative of its strength and the tread compound had the highest hardness value of the two compounds, as stated in Appendix D.

As mentioned, a lateral frictional force exists between the tests specimen and the sandpaper to resist lateral slippage of the sample during testing. Since the force was neglected in the calculation compression stress-strain results, the purpose of these results was to evaluate the response of the material model fit using both tensile and compression data, compared to the material fits obtained using only tensile test data. Thus, it was concluded that the uniaxial compression test results of the selected rubber compounds were considered sufficient to describe its material behaviour in compression for the purpose of this evaluation.

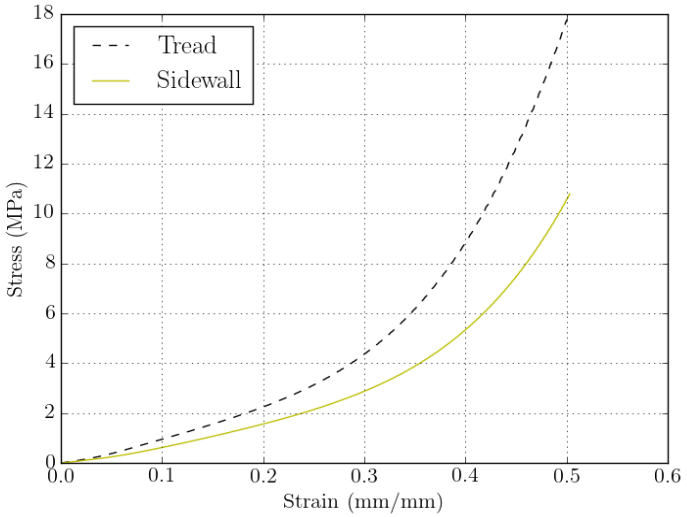

Figure C.18: Stress-strain curve of the average of the data sets for the sidewall and tread rubber in compression

Appendix D

Hardness tests

Durometers are typically used to measure the hardness of rubber. A standard method for determining the durometer hardness of rubber as given by ASTM D2240-05 (2010) was used as a guideline to determine the durometer hardness of the rubber compounds identified from the donated tyre segment. Samples were cut from the provided tyre segment and prepared for the hardness tests according to the requirements stated ASTM D2240-05 (2010). A standard method for the preparation of rubber surfaces from products as given by ASTM D3183-10 (2010) was used as a guideline to prepare the sample surfaces. These samples are shown in Figure D.1. The regions of rubber compounds identified from visual inspection were marked on these samples to indicate the regions of the hardness tests completed for each compound.

The hardness of samples A and B were measured using both Shore A and D scale durometers. Although the hardness of rubber used in tyre manufacturing are typically measured with a Shore A scale durometer, this appendix includes the hardness measurements of both scales to compare the trend of the results when using different scales.

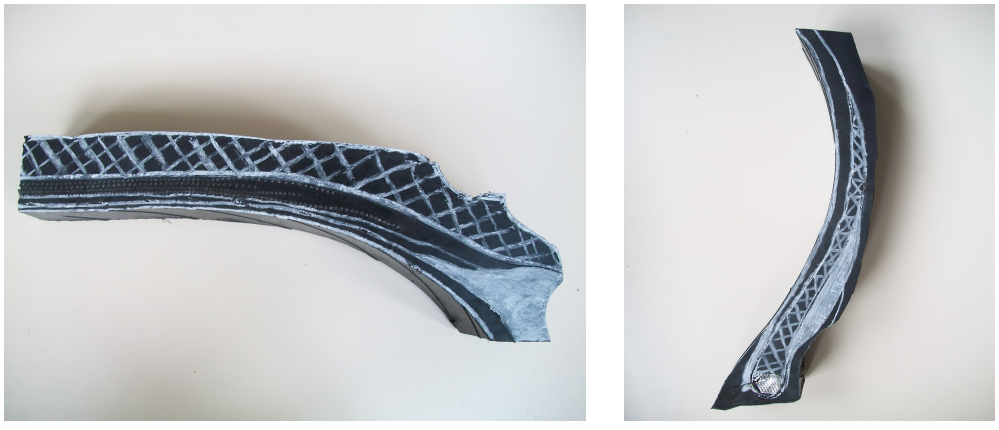

(a) (b)

Figure D.1: Regions of the rubber compounds identified from visual inspection of the tyre: (a) Tread cut-out (Sample A) and (b) sidewall cut-out (Sample B)

D.1 Equipment specifications and calibration

A digital Shore D scale durometer, reference number: 16HDM002-D100HD-06, was used to measure the Shore D scale hardness of the samples. The digital durometer is shown in Figure D.2. A PTC 306L-model, ASTM Type A classic-style durometer and 320-model durometer test stand by PTC Instruments were used to measure the Shore A scale hardness of the samples. The classical-style durometer and test stand are shown in Figure D.3.

The digital Shore D scale durometer was sent for official calibration on July 2013. The Type A classic-style durometer was sent for official calibration by the Cape Metrology field in July 2007, ID number: 24158. The calibration of both devices have been maintained by the Polymer Science Department at Stellenbosch University ever since.

D.2 Sample preparation

The sample surfaces were evened and buffed with a grinder and P40 Aluminium Oxide flap disks and P100 Aluminium Oxide sanding disks. This was done to ensure that the sample surfaces were flat and parallel over an area of at least 6.0 mm from the indentor point (sensing tip) (ASTM D2240-05, 2010). This specification was required to permit the presser foot to have even contact over the specimen area.

D.3 Methodology

The methodology used to measure the Shore D and A scale durometer hardness of the rubber samples are described in this section. The tests were completed at 23 °C and 101 625 Pa at the Polymer Science Department at Stellenbosch University.

Figure D.2: A digital Shore D scale durometer, reference number: 16HDM002-D100HD-06 (adapted from Eporm (2015))

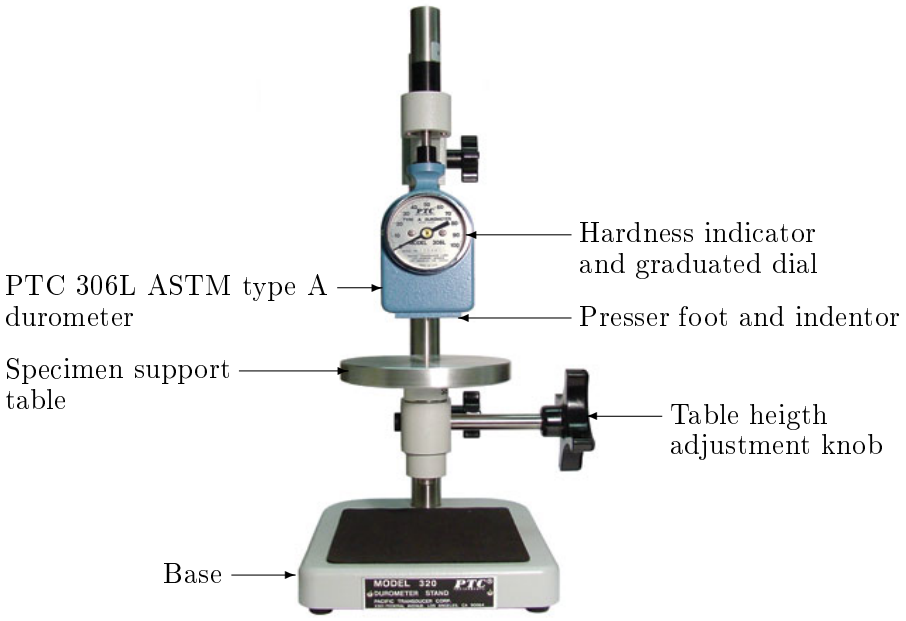

Figure D.3: A PTC 306L model, ASTM Type A classic-style durometer and 320-model durometer test stand by PTC Instruments (adapted from Stone Tucker Instruments (2015))

The samples were placed on a flat wooden slab to ensure stability during the measurements (ASTM D2240-05, 2010). The Shore D scale digital durometer was held in a vertical position and sufficient pressure was applied to assure firm contact between the presser foot and the specimen. The sensing tip was placed at the point of interest and was pressed against the sample surface in a smooth downward action to avoid shock to the sample. After the stand was in contact with the specimen, the indicated reading was recorded within 15 s and displayed on the LCD screen. At least five determinations of the hardness of each rubber compound where made at least 0.006 m apart (ASTM D2240-05, 2010).

A similar method was used to determine the Shore A scale hardness of the samples, however, in this case a classic-style durometer was used and the samples were placed on the specimen support table. The sample was pressed against the presser foot and indentor by means of the table height adjustment knob. The sample was pressed against the presser foot and indentor for at least 10 s to record the measured hardness indicated on the graduated dial. Again, at least five determinations of the hardness of each rubber compound were made at least 0.006 m apart.

D.4 Results

The Shore D and A scale durometer hardness of the rubber compounds are given in Tables D.1 and D.2. The rubber compounds were labelled according the terminology given in Section 3.2.

Table D.1: Shore D scale durometer hardness

Rim strip	Inner liner	Liner filler	Soft Apex	Rubber cushion	Sidewall	Shoulder cushion	Base	Tread
30.5	17.5	21.0	17.0	17.5	20.5	19.0	24.5	30.0
31.0	18.0	20.0	19.5	18.5	20.0	17.5	23.5	28.0
29.0	17.5	20.5	17.5	19.0	19.0	18.5	23.0	28.0
28.0	20.0	21.0	19.0	21.0	19.5	20.0	24.5	27.5
27.5	18.5	21.0	17.0	21.0	18.0	18.0	24.0	27.5
28.0	18.0	20.5	19.5	20.5	19.5	20.0		32.0
29.5	18.0	22.0	19.0		19.0			25.0
27.0	18.5	22.0	19.0		19.0			29.0
31.0		20.0	20.0		20.0			27.5
28.0		21.5	19.5		18.0			28.0
		22.0	20.0		18.5			30.0
		20.5	18.0		20.0			
		22.0	18.5		20.0			
		22.5			21.0			
					21.0			
					21.0			
29.0	18.3	21.2	18.7	19.6	19.6	18.8	23.9	28.4

Table D.2: Shore A scale durometer hardness

Rim strip	Inner liner	Liner filler	Soft Apex	Rubber cushion	Sidewall	Shoulder cushion	Base	Tread
70	50	61	61	52	62	59	64	73
72	57	61	58	59	65	54	64	77
78	51	64	57	64	60	51	65	69
77	52	65	58	61	58	63	65	74
71	57	64	58	61	57	57	64	74
	56	62	57		60		63	67
	56	62	58		59			71
		57			60			72
		64			59			72
		59			61			70
		64			61			74
73.6	54.1	62.1	58.1	59.4	60.2	56.8	64.2	72.1

D.5 Discussion and conclusion

The hardness of the rubber compounds were determined from the arithmetic mean of the results given in Tables D.1 and D.2. From the results obtained, it can be seen that the trend in the Shore D and A scale durometer hardness measurements are consistent. However, durometer readings below 20 or above 90 are not considered reliable (ASTM D2240-05, 2010), and therefore the Shore D scale durometer were only used to compare the trend of the results of both scales.

According to Clark (1981) the typical Shore A scale durometer hardness of steel belted radial passenger tyres are: 62 for the tread, 60 for the base, 55 for the sidewall, 75 for the apex and 50 for the inner liner. The typical Shore A hardness values of steel belted radial truck tyres are: 65 for the tread, 60 for the base, 60 for the sidewall and 89 for the apex (Clark, 1981).

Thus, it was concluded that the trend of the measured Shore D and A scale durometer hardness measurements are consistent and the measured hardness of the rubber compounds are consistent with the expected hardness given in literature. The measured hardness of the rubber compounds was used to distinguish between the different rubber compounds and its influence on the material properties of each compound. These properties included an indication of the amount of carbon black introduced in the rubber compound, its strength and its expected hysteresis coefficient.

Appendix E

Rubber density

The density of the rubber compounds were established from volume and mass measurements of sidewall and tread samples cut from the donated tyre segment. The equipment, calibration, sample preparation, methodology and results are discussed in this appendix.

E.1 Equipment specifications and calibration

A KERN EMB600-2 0.01g/100g precision balance scale was used to measure the mass of each rubber sample. The scale was calibrated using a set of calibrated masses. The calibrated masses, its recorded mass, and the percentage difference are given in Table E.1. From the results obtained, it was concluded that the percentage difference in mass were considered negligible and the instrument was used to measure the masses of the samples.

Table E.1: Calibrated masses, its recorded mass, and percentage difference

Calibrated mass (kg)	Measured mass (kg)	% Difference (%)
0.0500	0.0498	0.40
0.0102	0.0100	0.02
0.0050	0.0050	0.00
0.0199	0.0199	0.00

E.2 Sample preparation

The samples prepared for the compression tests, as shown in Figure C.14, were used to determine the density of the rubber compounds.

E.3 Methodology

The diameter and thickness of the sidewall and tread rubber compounds were measured with a vernier. The samples were placed on the scale and its measured mass was recorded. The set-up is shown in Figure E.1.

(a) (b)

Figure E.1: (a) Calibrated mass and scale; (b) Rubber sample and scale

E.4 Results

The measured diameter, thickness, mass and its calculated volume and density are given in Table E.2. The volume of the compounds were calculated using,

$$V = \frac{\pi}{4} D^2 t \tag{E.1}$$

where V in the volume of the sample (m^3), D is the diameter of the sample (m), and t is the sample thickness (m).

Table E.2: Sample dimensions, volume, mass and density

	Diameter (m)	Thickness (m)	Volume ($10^{-6} m^3$)	Mass (kg)	Density (kg/m^3)
Sidewall sample 1	0.0293	0.0113	7.4639	0.0083	1112.0
Sidewall sample 2	0.0030	0.0120	8.4823	0.0088	1037.5
Sidewall sample 3	0.0030	0.0122	8.6237	0.0085	985.7
Tread sample 1	0.0029	0.0116	7.6620	0.0077	1005.0
Tread sample 2	0.0295	0.0110	7.5180	0.0078	1037.5
Tread sample 3	0.0290	0.0105	6.9350	0.0074	1067.1

E.5 Discussion and conclusion

The average density of the sidewall and tread rubber were 1 045.1 kg/m^3 and 1 036.5 kg/m^3, respectively. The average density of both compounds was 1 040.8 kg/m^3. The density of natural rubber, styrene-butadiene rubber, polybutadiene rubber which are typically used for the rubber compounds in the tread and sidewall of a tyre, range from 1 130 to 1 140 kg/m^3 (Gent, 2012). Thus, a density of 1 040.8 kg/m^3 was considered sufficient to define the density of the rubber compounds in the tyre.

Appendix F

Hysteresis coefficient

This chapter includes the sample preparation, the methodology and the results obtained from the dynamic mechanical analysis (DMA) performed on the inner liner, sidewall and tread rubber compounds. The tests were done at the Council for Scientific and Industrial Research (CSIR) in Pretoria [1]. The purpose of these tests was to determine the hysteresis coefficient of the selected rubber compounds.

F.1 Sample preparation

Samples were cut from the inner liner, sidewall and tread rubber of the donated tyre segment. The samples were prepared according to the dimensions specified by the CSIR for DMA for each of the selected rubber compounds. The resulting sample length, width and thickness were 0.04, 0.013, and 0.004 m, respectively. Three samples were prepared from each of the selected rubber compounds.

F.2 Methodology

Each sample was tested at a different frequencies. These test frequencies included 0.86, 1.72, 2.58 Hz. These frequencies were calculated from Equation 2.16, using a rolling velocity of 15, 30 and 45 km/h and tyre radius of 0.771 m. The DMA tests were done at each frequency while ramping up the temperature from 23 °C to 100 °C.

F.3 Results

The DMA test results included the storage modulus, E', the loss modulus E'' and the tangent of phase difference, tan (δ). The hysteresis coefficient of the rubber compounds were calculated from Equations 2.11 and 2.12. The resulting hysteresis coefficient of the inner liner, sidewall and tread rubber compounds as a function of temperature are shown in Figures F.1, F.2 and F.3, respectively.

[1] Gertrude Makgatho, Polymer Characterisation Technician, CSIR, 1 Meiring Naude Rd, Brummeria, Pretoria, 0001, South Africa. E-mial: GMakgatho@csir.co.za

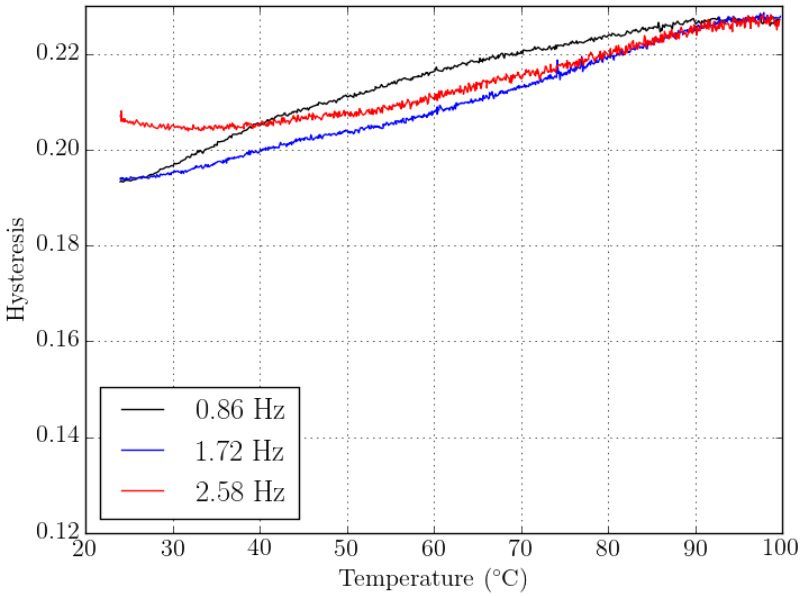

Figure F.1: Inner liner rubber: hysteresis coefficient as a function of temperature at 0.86, 1.72, 2.58 Hz

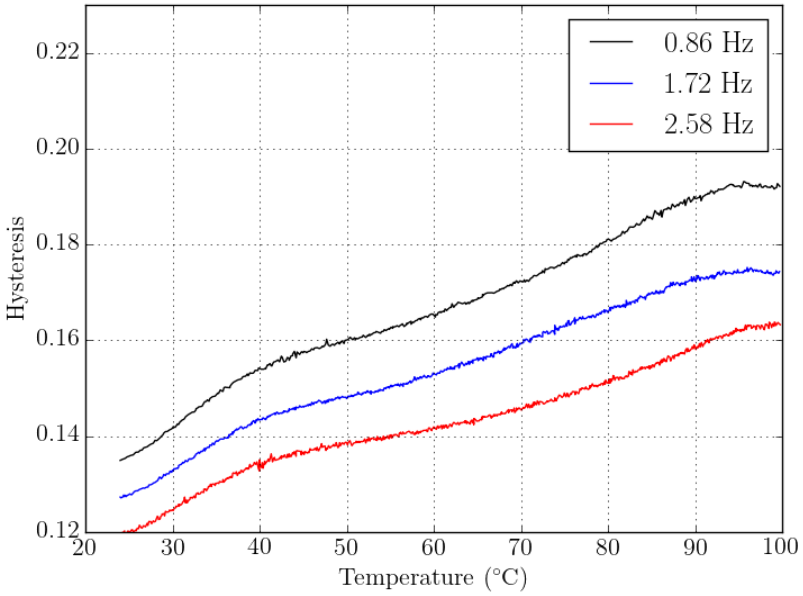

Figure F.2: Sidewall rubber: hysteresis coefficient as a function of temperature at 0.86, 1.72, 2.58 Hz

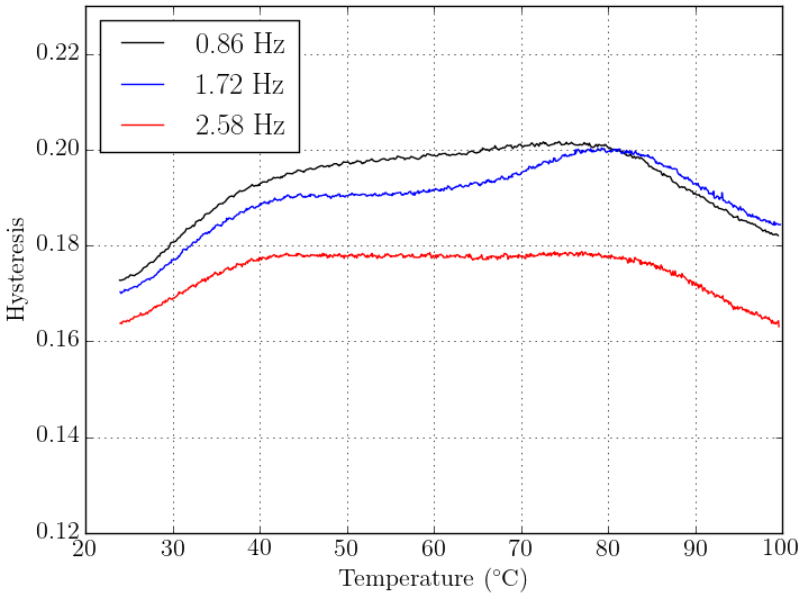

Figure F.3: Tread rubber: hysteresis coefficient of the tread as a function of temperature at 0.86, 1.72, 2.58 Hz

From the results obtained, it can be seen that the hysteresis coefficient varies with of both frequency and temperature. The average for each frequency over the temperature rage for each rubber compound is given in Table F.1. The resulting average for the listed frequencies for each of the rubber compounds are also given in Table 3.5.

Table F.1: Average hysteresis coefficient for each of the rubber samples at each frequency

Frequency	Hysteresis coefficient		
(Hz)	Inner liner	Sidewall	Tread
0.86	0.2155	0.1683	0.1937
1.72	0.2104	0.1555	0.1906
2.58	0.2137	0.1434	0.1749
Average	0.2132	0.1557	0.1864

F.4 Discussion and conclusion

The corresponding tan (δ) of the average hysteresis coefficient of the inner liner, sidewall and tread, are 0.2183, 0.1577, 0.1898, respectively. The typical tan (δ) values for steel belted radial passenger tyres are: 0.2 for the tread and base, 0.25 for the sidewall 0.25, and 0.4 for the inner liner (Clark, 1981). The typical tan (δ) values

for steel belted radial truck tyres, are: 0.2 for the tread, 0.17 for the base and the sidewall (Clark, 1981). Thus, the results obtained are within the same ranges as the typical values found in literature.

Although these results were consistent with that of literature, it was used to evaluate the assumptions made about the influence of carbon black on the expected hysteresis coefficient of the rubber compounds. In Section 2.2 it was stated that carbon black added to the rubber compound has a significant influence on the strength and hysteresis of the compounds. Carbon black increases the modulus, the hardness and the hysteresis coefficient of a rubber compounds (Clark, 1981). However, from the hardness results obtained in Appendix D, the tread had the highest hardness, then the sidewall and then the inner liner rubber compound. Thus, it would be expected that the tread would have the highest hysteresis coefficient and not the inner liner, as seen in Table F.1.

The reason for this result is due to the rubber polymer used for inner liner and tread rubber. Natural rubber, styrene-butadiene rubber, and butyl rubber are typically used for the tread and sidewall, while butyl rubber or halogenated butyl rubber are used for the inner liner (McGarry, 2007). The internal viscosity of butyl rubber is especially high (Gent, 2012) and therefore a high hysteresis coefficient is expected regardless of its low hardness reading.

The hysteresis coefficient of the tread and sidewall rubber is expected, since the tread and sidewall are typically made from the same rubber polymers and the tread had a higher hardness than the sidewall. Furthermore, a higher hysteresis coefficient for the tread is desirable, since an increase in hysteresis can lead to an increase in friction between the tyre and road contact area (Cho *et al.*, 2013). A low hysteresis coefficient for the sidewall is desirable, since the most of the tyre deformation occurs in the sidewall, which can easily lead to excessive heat generation if a compound with a high hysteresis coefficient is used.

From the results obtained it was concluded that the hysteresis coefficients calculated from the DMA results were consistent with literature and the expected rubber behaviour. It should be noted that the coefficient varies with of both frequency and temperature. In order to simplify the evaluation of the heat generation in the tyre the average coefficient of the selected rubber compounds given in Table F.1 were used instead. By using this approach the heat generation in the tyre could be evaluated purely as a function of its operating conditions and therefore excluding the influence of a varying hysteresis coefficient.

Appendix G

Contact stress

The contact normal stress distribution of the tyre model at each of the inflation and load conditions given in Table 5.1 are shown in Figures G.1 and G.2.

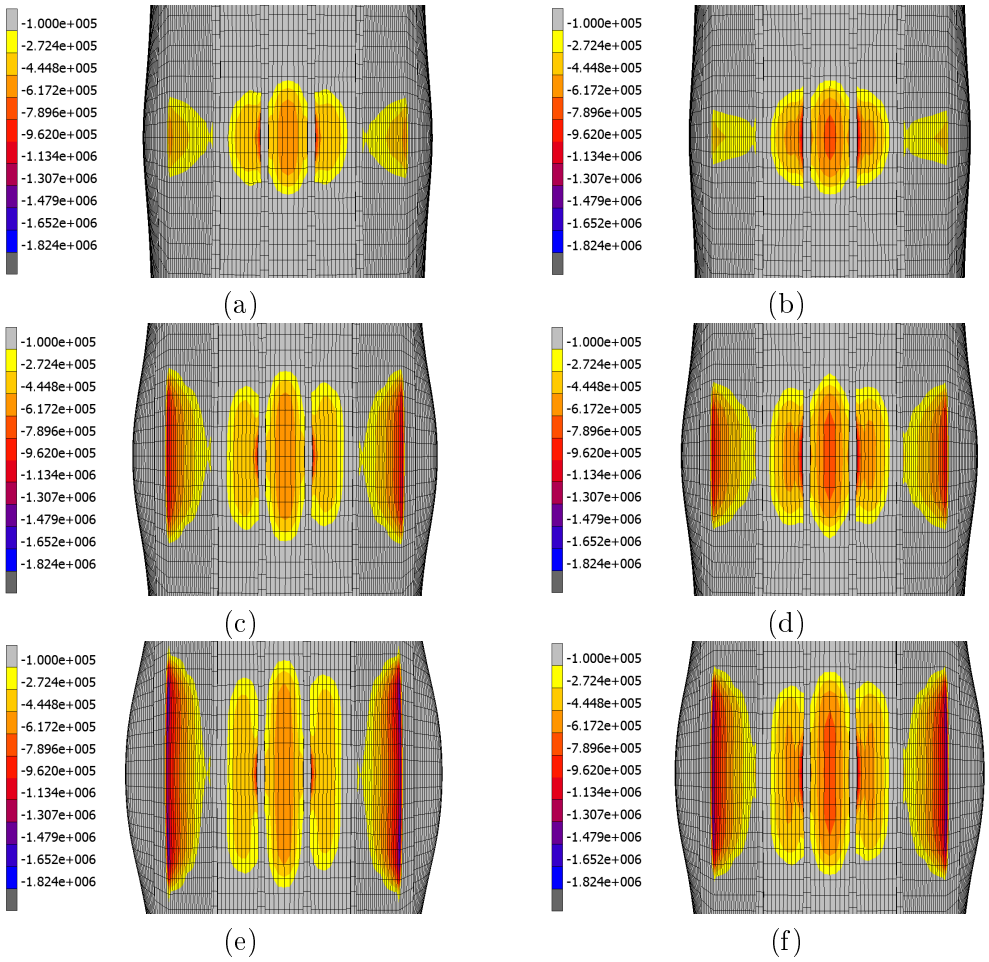

Figure G.1: Contact normal stress distribution of the tyre model inflated to 200 kPa and loaded to: (a) 22 588 N, (c) 48 656 N and (e) 74 703 N; Contact normal stress distribution of the tyre model inflated to 268 kPa and loaded to: (b) 22 588 N, (d) 48 656 N and (f) 74 703 N

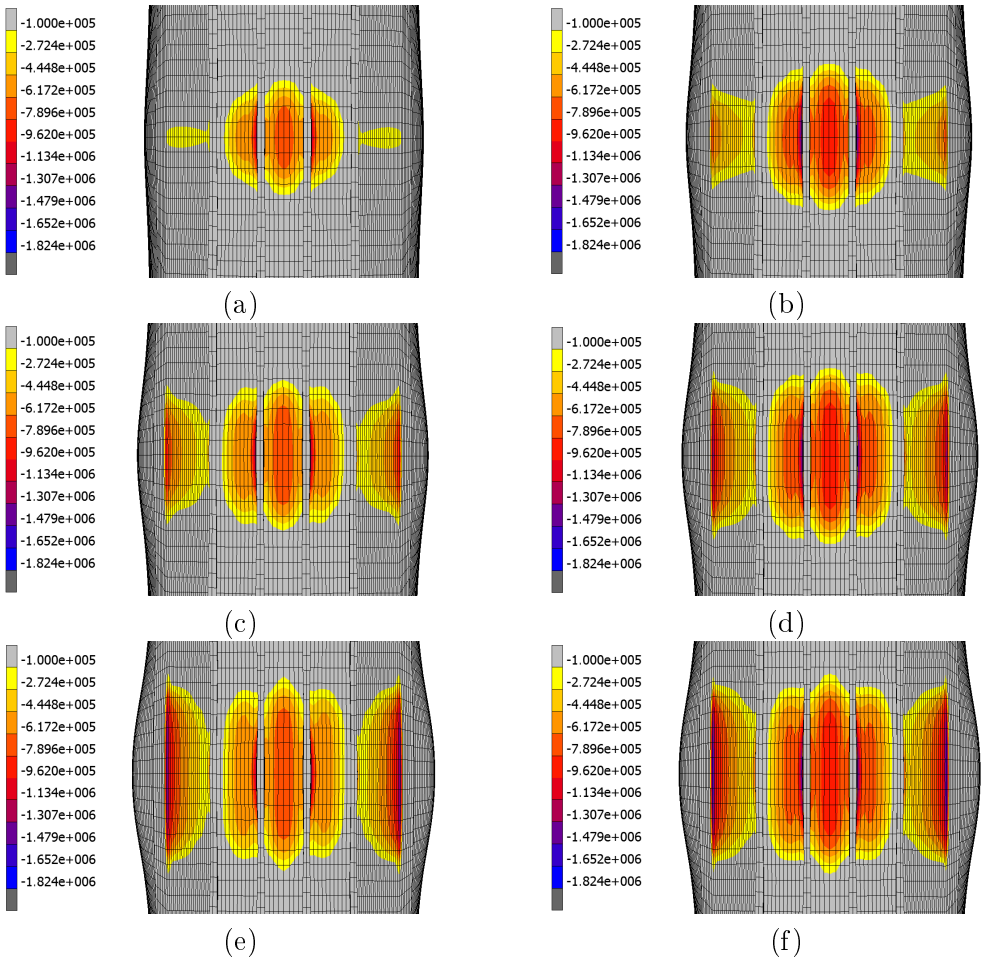

Figure G.2: Contact normal stress distribution of the tyre model inflated to 336 kPa and loaded to: (a) 22 588 N, (c) 48 656 N and (e) 74 703 N; Contact normal stress distribution of the tyre model inflated to 450 kPa and loaded to: (b) 48 656 N, (d) 74 703 N and (f) 90 742 N

Appendix H

Temperature distribution

The temperature distribution in the 2-D axisymmetric tyre model for each combination of the operating conditions given in Table 5.1 are shown in Figures H.1 to H.3.

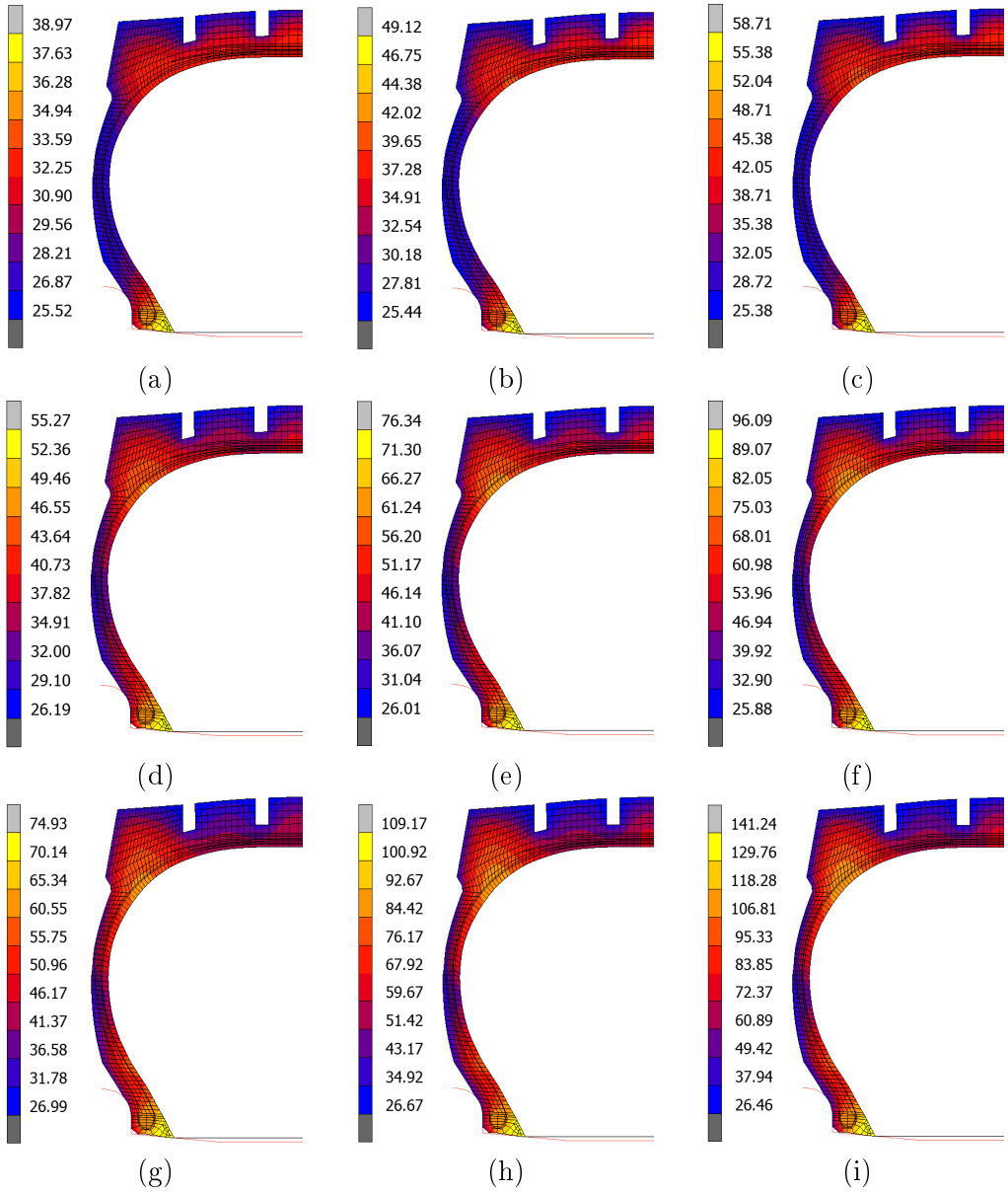

Figure H.1: Temperature distribution of the tyre model inflated to 200 kPa and loaded to: 22 588 N at (a) 15, (b) 30 and (c) 45 km/h; Temperature distribution of the tyre model inflated to 200 kPa and loaded to: 48 656 N at (d) 15, (e) 30 and (f) 45 km/h; Temperature distribution of the tyre model inflated to 200 kPa and loaded to: 74 703 N at (g) 15, (h) 30 and (i) 45 km/h

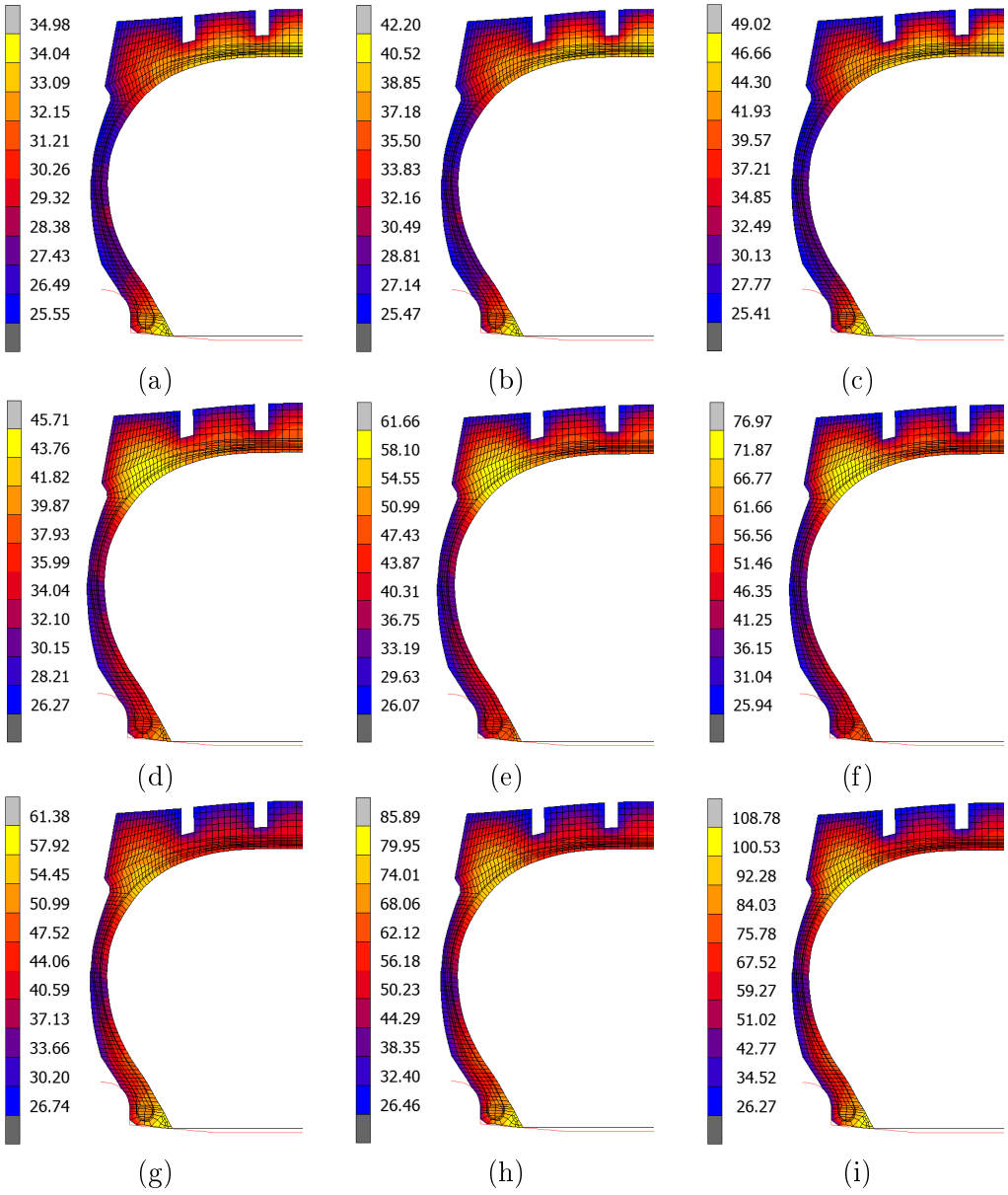

Figure H.2: Temperature distribution of the tyre model inflated to 268 kPa and loaded to: 22 588 N at (a) 15, (b) 30 and (c) 45 km/h; Temperature distribution of the tyre model inflated to 268 kPa and loaded to: 48 656 N at (d) 15, (e) 30 and (f) 45 km/h; Temperature distribution of the tyre model inflated to 268 kPa and loaded to: 74 703 N at (g) 15, (h) 30 and (i) 45 km/h

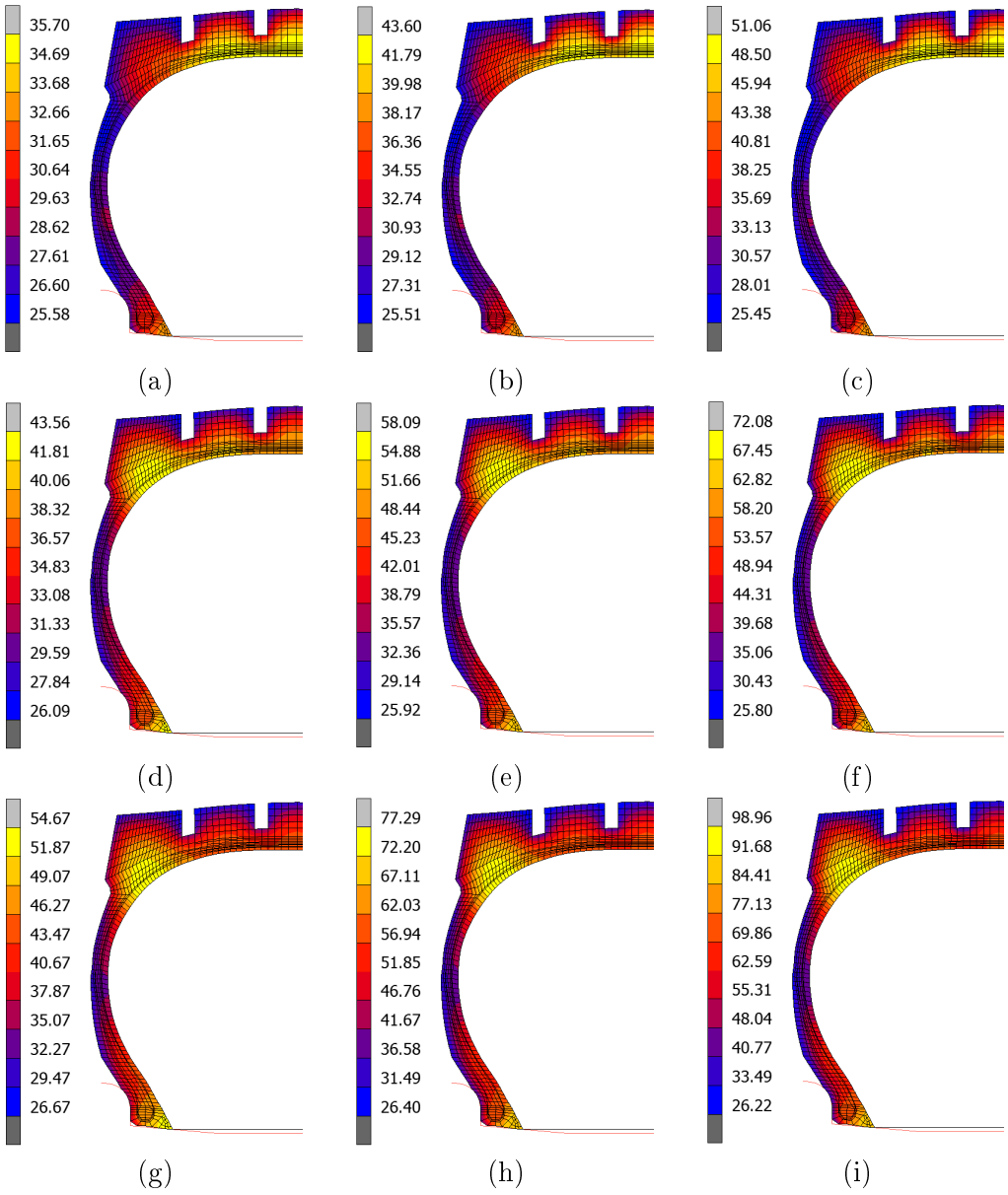

Figure H.3: Temperature distribution of the tyre model inflated to 336 kPa and loaded to: 22 588 N at (a) 15, (b) 30 and (c) 45 km/h; Temperature distribution of the tyre model inflated to 336 kPa and loaded to: 48 656 N at (d) 15, (e) 30 and (f) 45 km/h; Temperature distribution of the tyre model inflated to 336 kPa and loaded to: 74 703 N at (g) 15, (h) 30 and (i) 45 km/h

List of References

Anzor (2016). *Stainless steel wire rope/cable types* [Online]. Available at: http://www.anzor.com.au/content/stainless-steel-wire-ropecable-types. [2016, August 9].

Assaad, M., Kimble, B., Huang, Y.-M., Burgan, R., Fralick, G.C., Wrbanek, J.D. and Gonzalez, J.M. (2008). Thin film heat flux sensor for measuring film coefficient of rubber components of a rolling tire. *Tire Science and Technology*, vol. 36 (4), pp. 275–289.

ASTM D2240-05 (2010). *Standard test method for rubber property: Durometer hardness.* West Conshohocken: ASTM International.

ASTM D3183-10 (2010). *Standard practice for pubber: Preparation of pieces for test purposes from products.* West Conshohocken: ASTM International.

ASTM D412-06a (2013). *Standard test methods for vulcanized rubber and thermoplastic elastomers: Tension.* West Conshohocken: ASTM International.

ASTM D4975-04 (2011). *Standard test methods for single-filament tire bead wire made from steel.* West Conshohocken: ASTM International.

ASTM D575-91 (2012). *Standard test methods for rubber properties in compression.* West Conshohocken: ASTM International.

ASTM E8/E8M-11 (2011). *Standard test methods for tension testing of metallic materials.* West Conshohocken: ASTM International.

Axel (2015). *Testing brief: Compression or biaxial extension?* [Online]. Available at: http://www.axelproducts.com/downloads/CompressionOrBiax.pdf. [2015, September 21].

Bell (2015*a*). *Articulated dump truck* [Online]. Available at: http://www.bellequipment.com/apps/bell/bellza.nsf/0/9D38A25934CE88CB42257B4B0034E3B6/$file/technical_data.pdf. [2015, October 5].

Bell (2015*b*). *Michelin tyres for Bell machines* [Online]. Available at: http://www.bellequipment.com/apps/bell/bellza.nsf/0/1E19E93B23DEE8D942257CAC0028A1BB/$file/Michelin-Bell-Tyre(Broch14100813)web.pdf. [2015, September 24].

Bell (2016). *Articulated dump truck* [Online]. Available at: http://www.bellequipment.com/resource/0/69E8854910F88EF842257EBD002BF72C/$file/B45D-dimensions.jpg. [2016, August 1].

Bell, S.L. (ed.) (2010). *Standard wire, rope and cable, or iron or steel.* Washington, D.C.: U.S. Dept. of Homeland Security, U.S. Customs and Border Protection.

Benoît, R., Lafrance, L., Malo, D. and Baron, J. (2009). *Heavy vehicles tire blowout and explosion.* Tech. Rep., Montréal: Association Sectorielle Transport Enterposage.

Bridon (2016). *Steel rope technical information* [Online]. Available at: http://www.bridon.com/china/x/downloads/steel_technical.pdf. [2016, February 3].

Canadian Wheel (2012). *Offroad wheels and rims* (catalogue). Edmonton: Canadian Wheel.

Carl Stahl Technocables (2016). *Strands and wire ropes* [Online]. Available at: http://www.carlstahl-technocables.com/wire-rope-science/strands-and-wire-ropes.html. [2016, January 14].

Cartwright, A. (2016). *Technical illustration cutaway: Realistic technical illustration of a tyre* [Online]. Available at: http://www.planetillustration.co.uk/illustration-05-tehnical-technicalillustration-cutaway-tyre-realistic.html. [2016, April 22].

Chi, S. and Caldas, C.H. (2009). Development of an automated safety assessment framework for construction activities. In: *Proceedings of 26th International Symposium on Automation and Robotics in Construction (ISARC), IAARC, Austin, TX, pp. 38-46.* Brisbane: Queensland University of Technology.

Cho, J., Lee, H., Jeong, W. and Kim, K. (2013). Numerical estimation of rolling resistance and temperature distribution of 3-D periodic patterned tire. *International Journal of Solids and Structures*, vol. 50, pp. 86–96.

Clark, S.K. (ed.) (1981). *Mechanics of pneumatic tires.* Washington, D.C.: U.S. Dept. of Transportation, National Highway Traffic Safety Administration.

Eporm (2015). *Shore D durometer scale digital hardness tester* [Online]. Available at: http://www.eprom.com/AM-16HDM002-D100HD/. [2015, October 22].

Gent, A.N. (ed.) (2012). *Engineering with rubber: How to design rubber components.* 3rd edn. Cincinnati: Hanser Publications.

Gent, A.N. and Walter, J.D. (2006). *The pneumatic tire.* Washington, D.C.: U.S. Dept. of Transportation, National Highway Traffic Safety Administration.

Ghoreishy, M.H.R. (2006). Steady state rolling of a radial tyre: Comparison with experimental results. *Proc. IMechE*, vol. 220 (Part D: J. Automobile Engineering), pp. 713 – 721.

Ghoreishy, M.H.R. (2008). A state of the art review of the fininte element modelling of rolling tyres. *Iranian Polymer Journal*, vol. 17 (8), pp. 571–597.

Ghoreishy, M.H.R., Malekzadeh, M. and Rahimi, H. (2007). A parametric study on the steady state rolling behaviour of a steel-belted radial tyre. *Iranian Polymer Jourmal*, vol. 16 (8), pp. 539 – 548.

Ghosh, S. (2011). *Invesigation on role of fillers on viscoelastic properties of tire tread compounds.* Ph.D. thesis, Vadodara: Maharaja Sayajirao University of Baroda.

Hankook (2015). *Types of tyres* [Online]. Available at: http://www.hankooktire.com/global/tires-services/tire-guide/types-of-tires/tires-by-structure.html. [2016, April 22].

Korunović, N., Trajanović, M. and Stojković, M. (2007). FEA of tyres subjected to static loading. *Serbian Society for Computational Mechanics*, vol. 1 (1), pp. 87 – 98.

Kováč, I. and Krmela, J. (2012). FE analysis of automobile tire. *Advanced Research in Scientific Areas*, vol. 7, pp. 1809–1812.

Lam Hong (2014). *Steel wire rope* [Online]. Available at: http://www.lamhongs.com.sg/steelwire-ropes.html. [2016, August 9].

Lin, Y.-J. and Hwang, S.-J. (2004). Temperature prediction of rolling tire by computer simulation. *Mathematics and Computers in Simulation*, vol. 67, pp. 235–249.

Maritz, J.C. (2015). *Numerical modelling and experimental measurement of the temperature distribution in a rolling tire.* Master's thesis, Stellenbosch: Stellenbosch University.

McGarry, P. (2007). *Haul truck tires and open pit mining applications.* Master's thesis, Kingston: Queen's University.

Michelin (2016). *The differences between bias and radial technologies* [Online]. Available at: http://www.michelinag.com/Innovating/Radial-vs.-Bias-technology. [2016, May 15].

Miller, K. (2002). *Testing elastomers for hyperelastic material models in finite element analysis* [Online]. Available at: http://easc.ansys.com/staticassets/ANSYS/staticassets/resourcelibrary/confpaper/2002-Int-ANSYS-Conf-147.PDF. [2015, September 25].

MSC (2010). *Experimental elastomer analyses: MAR103.* Santa Ana: MSC Software Co.

MSC (2013). *Basic nonlinear analysis using Marc and Mentat: MAR101.* Newport Beach: MSC Software Co.

MSC (2014*a*). *Marc® 2014, User guide.* Newport Beach: MSC Software Co.

MSC (2014*b*). *Marc® 2014, Volume A: Theory and user information.* Newport Beach: MSC Software Co.

Nyaaba, W., Frimpong, S. and Gbadam, E. (2015). Thermo-mechanical stress loading and deformation of OTR dump truck tires in surface mining operations. *International Journal of Advanced and Innovative Research*, vol. 4 (9), pp. 2278–7844.

Polymer Properties Database (2015). *Rubber elasticity* [Online]. Available at: http://polymerdatabase.com/polymer%20physics/RubberElasticity.html. [2016, May 5].

Roylance, D. (2001). Stress-strain curves. Class notes. Cambridge: Massachusetts Institute of Technology [Online]. Available at: http://ocw.mit.edu/courses/materials-science-and-engineering/3-11-mechanics-of-materials-fall-1999/modules/MIT3_11F99_ss.pdf. [2015, August 19].

Smith, R.E., Tang, T., Johnson, D., Ledbury, E. and Goddette, T. (2012). Simulation of thermal signature of tires and tracks. In: *Proceedings of the 2012 Ground Vehicle Systems Engineering and Technology Symposium (GVSETS), Warren.*

Stambaugh, H. and Banks, P. (1998). *Scrap and shredded tire fires.* Tech. Rep., Emmitsburg: U. S. Fire Administration, National Fire Data Center.

SteelConstruction.info (2012). *Steel material properties* [Online]. Available at: http://www.steelconstruction.info/Steel_material_properties. [2016, August 16].

Stone Tucker Instruments (2015). *PTC classic-style durometer* [Online]. Available at: http://www.stone-tucker.com/en/hardness-testers/ptc-classic-style-durometer. [2015, October 22].

TA Instruments (2014). *RSA-G2 Solids analyzer.* New Castle: TA Instruments. Available at: http://www.tainstruments.com/wp-content/uploads/RSA-G2.pdf. [2016, July 28].

Tang, T., Johnson, D., Smith, R.E. and Felicelli, S.D. (2014). Numerical evaluation of the temperature field of steady-state rolling tires. *Applied Mathematical Modelling*, vol. 28, pp. 1622–1637.

Topy (2008). *Rim instruction manual: Multi-piece rims for industrial and construction vehicles, Version 1.0.* Ayase: Topy Industies, Ltd.

Van Blommestein, W.B. (2016). *Experimentally determined material parameters for temperature prediction of an automobile tire using finite element analysis.* Master's thesis, Stellenbosch: Stellenbosch University.

Van Rooyen, M. (2015). *MTS criterion model 44: Giuide for skripsie students.* Tech. Rep., Stellenbosch: Stellenbosch University.